UTS UNIVERSITY OF TECHNOLOGY SYDNEY

Novel nanomaterials for efficient photocatalytic ammonia synthesis

by Qiang Hao

Thesis submitted in fulfilment of the requirements for the degree of

Doctor of Philosophy

under the supervision of Prof. Bruce Ni and Dr. Yiwen Liu

University of Technology Sydney
Faculty of Engineering and Information Technology

Aug 2021

Certification of original authorship

I, Qiang Hao declare that this thesis, is submitted in fulfilment of the requirements for the award of Doctor of Philosophy, in the School of Civil and Environmental Engineering, Faculty of Engineering and Information Technology at the University of Technology Sydney.

This thesis is wholly my own work unless otherwise referenced or acknowledged. In addition, I certify that all information sources and literature used are indicated in the thesis.

This document has not been submitted for qualifications at any other academic institution.

This research is supported by the Australian Government Research Training Program.

Signature: Production Note:
Signature removed prior to publication.

Date: 15/08/2021

Acknowledgements

Firstly, I would like to express my deepest acknowledgment to my principle supervisor: Prof. Bruce Ni. He helped me to get such a great opportunity to study at Centre for Technology in Water and Wastewater, University of Technology Sydney. He is an enthusiastic, gentle and nice person. More importantly, he always provides me excellent guidance, continual encouragement, in-time help and generous support. If I did not get his help, my research could not get published. I also acknowledge my co-supervisor Dr. Yiwen Liu's help. He is always happy to help me every time I need. Besides, he gave me a lot of suggestions about my future development.

Secondly, I want to thank our group members, including Miss. Xiaoqing Liu, Miss Lan Wu, Mr. Zhijie Chen and Dr. Wei Wei. They gave me a lot of support not only in my research, but also in daily life. I would also like to say thank you to the students at our school including Dr. Lei Zheng, Dr. Jiantao Li, Dr. Dongle Cheng, Dr. Jiawei Ren, Dr. Minwei Yao, Miss. Huan Liu, Mr. Zehao Zhang, Mr. Linhao Li, Mr. Fulin Qu, Mr. Feng Shan, Mr. Haoding Xu, Mr. Feng Gao etc. They brought me a lot of happiness and warmness.

Thirdly, I appreciate the kind support of my research collaborators for their contribution to the density functional calculations. Dr. Chuangwei Liu (Technical University of Denmark) contributed to the calculation of Chapter 4. A/Prof. Ying Wang (Changchun Institute of Applied Chemistry, Chinese Academy of Science), contributed to the calculation of Chapter 6 and Dr. Liang Mao (China University of Mining and

Technology) contributed to the calculation of Chapter 7. Besides, I would like to acknowledge my research collaborators including Dr. Guohua Jia (Curtin university), A/Prof. Xiaojuan Bai (Beijing University of Civil Engineering and Architecture), Dr. Helen Xu (University of Technology Sydney), Prof. Igor Aharonovich (University of Technology Sydney), Dr. Yang Liu (Henan Normal University), Dr. Hamidreza Arandiyan (The University of Sydney), Prof. Qiang Kong (Shandong Normal University), Prof. Zhi-gang Chen (University of Southern Queensland), Dr. Monika Figiela (Poznan University of Technology), Miss. Sijia Sun (China University of Geosciences Beijing), A.Prof. Qingfeng Guo (China University of Geosciences Beijing), Dr. Xiaoguang Duan (The University of Adelaide), Prof. Shaobin Wang (The University of Adelaide) etc.

Then I want to thank the lab technical support officers at UTS, including Dr. Mohammed Johir, Dr. Herbert Yuan, Dr. Katie Mcbean, Dr. Mark Lockrey, Dr. Linda Xiao and Dr. Ron Shimmon. I also acknowledge the lab technical support officers at Sydney Analytical including Dr. Michelle Wood, Dr. Joonsup Lee, Dr. Sarah Kwlloway and Dr. Ahmed. Ahmed. They helped me to characterize my samples and analyzed the data.

Finally, I would like to thank my parents and my sister. They always provide encouragement to overcome the difficulties in my research and life.

Table of contents

Table list

Figure list

pseudocubic-C_3N_4 view from the [001] axis.

Figure. 2.7 Triazine-(a) and tri-s-triazine-based connection patterns (b) of potential g-C_3N_4 allotropes.

Figure 2.8 (a) The crystal structure of metal Bi from standard orientation, (b) Scheme of the defective Bi nanoplates for the N_2 fixation reaction, (c) The free-energy charts for the N2 fixation response on Bi(110) and Bi(110) features through a response pathway, and (d) Limiting potentials for nitrogen reduction on different metals vs. the binding energy of N_2H*; (e) Volcano plot for the HER on representative transition metals; (f) activation energy of the rate-determining step. (b-f) Reproduced with permission (Wang, Shi, et al. 2019). Copyright 2019, Wiley-VCH.

Figure 2.9 (a) The crystal structure of δ-Bi_2O_3 from standard orientation. (b) EPR spectra of δ-Bi_2O_3 and 3% AgCl/δ-Bi_2O_3. (c) The crystal structure of BiO from standard orientation. The calculated charge density at the VB of BiO (010) surfaces by (d) top view and (e) side view. (f) A probable route for the nitrogen molecule activation and the hydrogenation on the surface of the bismuth oxide catalyst. (b) Reproduced with permission (Gao, Shang, et al. 2019a). Copyright 2019, Elsevier. (d-f) Reproduced with permission (Sun et al. 2017). Copyright 2017, Royal Society of Chemistry.

Figure 2.10 (a) The crystal structure of BiOBr from standard orientation; (b) schematic illustration of the probable photocatalytic nitrogen fixation over defect-rich Bi_3O_4Br. (b) Reproduced with permission (Di et al. 2019). Copyright 2019, Wiley-VCH.

5 to 80 degrees. (b) The FTIR spectra of BiOBr and BiOBr-TCNQ between 2300 to 500 cm^{-1}. The narrow XPS spectra of O1*s* (c) and Bi 4*f* (d). The EPR spectra of BiOBr (e) and BiOBr-TCNQ samples (f). Inserted image in Figure 2f: The proposed possible structure of BiOBi-TCNQ sample.

Figure 5.3 The zoom-in part of FTIR spectra of prepared samples.

Figure 5.4 (a) The ammonia concentration changes over time. (b) The NH_3 yield by prepared samples. (c) The NMR spectra of $^{15}NH_4Cl$ standard solution and the final photoreduction production of $15N_2$ by BiOBi-TCNQ-2. (d) The NH_3 yield of BiOBi-TCNQ-2 in cycle uses.

Figure 5.5 The UV-vis spectra of the solution to detect hydrazine with color reagent.

Figure 5.6 (a) The UV-vis DRS spectra of BiOBr, TCNQ and BiOBr-TCNQ samples. (b) The photoluminescence spectra, (c) photocurrent response and (d) electrochemical impedance spectroscopy of BiOBr and BiOBr-TCNQ-2. (e) The mechanisms of the separation and transfer of photogenerated electron-hole pairs for the remarkable photocatalytic N_2 fixation performance.

Figure 6.1 HRTEM image of g-C_3N_4 nanosheets (a), CN-Ru-1 (b) and the zoom-in part of the lattice (c), high-angle annular dark-field image (d), energy dispersive spectroscopy for Ru element mapping (e), and SEM image of CN-Ru-1 (f).

Figure 6.2 The XRD patterns of bulk CN, 2D-CN and CN-Ru samples.

Figure 6.3 Narrow C 1*s* XPS spectra of 2D-CN (a) and CN-Ru-1 (b). Narrow N 1*s* XPS spectra of 2D-CN (c) and CN-Ru-1 (d).

Figure 6.4 (a) Photocatalytic activity of bulk CN, 2D-CN and CN-Ru samples, and (b) cycle stability of CN-Ru-1. (c) The NMR spectra of $^{15}NH_4Cl$ standard solution and the final photoreduction production of $Na^{15}NO3$ by CN-Ru-1. The proportions of productions and NO_3^- after photocatalytic reaction by (d) bulk CN and (e) CN-Ru-1. The selectivity of photocatalytic reduction of NO_3^- by (f) bulk CN and (g) CN-Ru-1.

Figure 6.5 UV-vis DRS of bulk CN, 2D-CN and CN-Ru samples (a). Density of states of g-C_3N_4 and CN-Ru (b). Photocurrent response (c), EIS (d) and PL spectra (e, f) of bulk CN, 2D-CN and CN-Ru samples.

Figure 6.6 Adsorption structures and calculated adsorption energies of NO_3^- adsorbed on g-C_3N_4 (a) and CN-Ru (b). Optimized spin density (c) and charge differences (d) of CN-Ru.

Figure 6.7 Calculated free energy differences between the formation of H_2 and N_2 on g-C_3N_4 (a) and CN-Ru (b). Calculated free energy changes of NO_3^- reduction to NH_3 on g-C_3N_4 and CN-Ru (c).

Figure 6.8 The elements that can be reduced by green tea theoretically.

Figure 7.1 (a) The XRD patterns of prepared bismuth/bismuth oxide samples. (b) The crystal structure of Bi_2O_3 and metallic bismuth. (c) The narrow XPS spectra of Bi of BiO-120 and BiO-160. (d) The narrow XPS spectra of O of BiO-120 and BiO-160.

Figure 7.2 The SEM images of BiO-120 (a) and BiO-160 (b). The TEM images of BiO-120 (c, d) and BiO-160 (e). The HADDF TEM image of BiO-160 (f) and EDS

mapping of C (g), O (h) and Bi (i) of BiO-160.

Figure 7.3 (a) The ammonia concentration in the photocatalytic reaction system with time went by. (b) The ammonia yield of prepared samples. (c) The cycle stability of BiO-160 used for 4-time nitrate reduction. (d) The NMR spectra of $^{15}NH_4^+$ standard solution and the final photoreduction production of $^{15}NO_3^-$ by BiO-160. The proportions of productions and NO_3^- after photocatalytic reaction by (e) BiO-120 and (f) BiO-160. The selectivity of photocatalytic reduction of NO_3^- by (g) BiO-120 and (h) BiO-160.

Figure 7.4 (a) The DFT calculated band structure of Bi_2O_3. (b) The UV-vis DRS spectra of prepared bismuth/bismuth oxide samples. (c) The photocurrent response of prepared samples with the light on and off. (d) The EIS Nyquist plots of prepared-sample electrodes in the dark.

Figure 7.5 The band structure and possible separation pathways of photogenerated charge carriers for enhanced photocatalytic activity.

List of abbreviations

Symbol	Description
$BaSO_4$	Barium sulfate
BET	Brunauer-Emmett-Teller
Bi	Bismuth
$Bi(NO_3)_3 \cdot 5H_2O$	Bismuth nitrate pentahydrate
BiOBr	Bismuth bromide oxide
Bi_2MoO_6	Bismuth molybdate
$BiVO_4$	Bismuth vanadate
C	Carbon
CB	Conduction band
CN	Carbon nitride
CO_2	Carbon dioxide
Cu	Copper
DFT	Density functional theory
D-CN	Defective g-C_3N_4
DRS	Diffuse reflectance spectra
DMF	*N*,*N*-dimethylformamide
DMSO	Dimethyl sulfoxide
EIS	Electrochemical impedance spectroscopy
ESR	Electron spin resonance
EDS	Energy dispersive spectroscopy
EDTA	Ethylenediaminetetraacetic acid
Fe	Iron
FT-IR	Fourier transform infrared

g-C_3N_4	Graphitic carbon nitride
H_2	Hydrogen
HER	Hydrogen evolution reaction
H_2O	Water
HAADF-STEM	High-angle annular dark-field scanning transmission electron microscopy
HI	Hydriodic acid
HCl	Hydrochloric acid
H_2SO_4	Sulfuric acid
HNO_3	Nitric acid
IC	Ion chromatography
ITO	Indium-tin oxide
K	Potassium
K_2SO_4	Potassium sulphate
KBr	Potassium bromide
La	Lanthanum
Li	Lithium
LiOH	Lithium hydroxide
Mo	Molybdenum
Mg	Manganese
N	Nitrogen
N_2	Nitrogen gas
NH_3	Ammonia
NO_2^-	Nitrite
NO_3^-	Nitrate

NH_4^+	Ammonium
N_2O	Nitrous oxide
NO	Nitric oxide
NO_2	Nitrogen dioxide
N_2O_5	Dinitrogen pentoxide
N_2H_4	Hydrazine
NH_4Cl	Ammonium chloride
NaClO	Sodium hypochlorite
NaOH	Sodium hydroxide
Ni	Nickle
NRR	Nitrogen reduction reaction
NMR	Nuclear Magnetic Resonance
$NaNO_3$	Sodium nitrate
Na_2SO_4	Sodium sulfate
Pt	Platinum
Pd	Palladium
PL	Photoluminescence
Ru	Ruthenium
$RuCl_3$	Ruthenium trichloride
rGO	reduced graphene oxide
RHE	Reversible hydrogen electrode
SCE	Saturated calomel electrode
Sn	Selenium
SPR	Surface plasmon resonance
SEM	Scanning electron microscope

TCNQ	Tetracyanoquinodimethane
TEM	Transmission electron microscope
TiO_2	Titanium dioxide
THF	Tetrahydrofuran
V	Vanadium
VB	Valence band
XRD	X-ray diffraction
XPS	X-ray photoelectron spectroscopy
XRF	X-ray fluorescence
ZnO	Zinc oxide
ZIF	Zeolitic imidazolate framework

List of publications

Note: The candidate prefers to use his preferred name "Derek" in publications as the given name start with "q" is difficult to pronounce for English speakers.

A. First-author Peer-Reviewed Journal Articles

1) **Q. Hao**, Y. Liu, T. Chen, Q. Guo, W. Wei, B. J. Ni. Bi_2O_3@Carbon Nanocomposites for Solar-Driven Photocatalytic Degradation of Chlorophenols. ACS Applied Nano Materials. 2019, 2 (4), 2308-2316. (JCR: Q2)

2) R. Wang, **Q. Hao**, J. Feng, G.C. Wang, H. Ding, D. Chen, B. Ni. Enhanced separation of photogenerated charge carriers and catalytic properties of ZnO-MnO_2 composites by microwave and photothermal effect. Journal of Alloys and Compounds. 2019, 786, 418-427. (Equal contribution) (JCR: Q1)

3) **Q. Hao**, C. Liu, G. Jia, Y. Wang, H. Arandiyan, W. Wei, B.J. Ni. Catalytic reduction of nitrogen to produce ammonia by bismuth-based catalysts: state of the art and future prospects. Materials Horizons. 2020, 7 (4), 1014-1029. (JCR: Q1, ESI highly cited paper)

4) **Q. Hao**, G. Jia, W. Wei, A. Vinu, Y. Wang, H. Arandiyan, B.J. Ni. Graphitic carbon nitride with different dimensionalities for energy and environmental applications. Nano Research. 2020. 13, 18-37. (JCR: Q1, ESI highly cited paper)

5) **Q. Hao**, C. Xie, Y. Huang, D. Chen, Y. Liu, W. Wei, B.J. Ni. Accelerated separation of photogenerated charge carriers and enhanced photocatalytic performance of g-C_3N_4 by Bi_2S_3 nanoparticles. Chinese Journal of Catalysis. 2020. 41 (2), 249-258. (JCR: Q1,

ESI highly cited paper, Front cover)

6) **D. Hao**, C. Liu, X. Xu, M. Kianinia, I. Aharonovich, X. Bai, X. Liu, Z. Chen, W. Wei, G. Jia, B.J. Ni. Surface defect-abundant one-dimensional graphitic carbon nitride nanorods boost photocatalytic nitrogen fixation. New Journal of Chemistry. 2020, 44, 20651-20658. (JCR: Q2)

7) **D. Hao**, Z. Chen, M. Figiela, I. Stepniak, W. Wei, B.J. Ni. Emerging alternative for artificial ammonia synthesis through catalytic nitrate reduction. Journal of Materials Science & Technology. 2021, 77, 163-168. (JCR: Q1)

8) **D. Hao**, Y. Liu, S. Gao, H. Arandiyan, X. Bai, Q. Kong, W. Wei, P.K. Shen, B.J. Ni. Emerging artificial nitrogen cycle processes through novel electrochemical and photochemical synthesis. Materials Today. 2021, 46, 212-233. (JCR: Q1, Inner cover)

9) **D. Hao**, Q. Huang, W. Wei, X. Bai, B.J. Ni. A reusable, separation-free and biodegradable calcium alginate/g-C_3N_4 microsphere for sustainable photocatalytic wastewater treatment. Journal of Cleaner Production. 2021, 128033. (JCR: Q1)

10) **D. Hao**, J. Ren, H. Arandiyan, M. Garbrecht, X. Bai, H. K. Shon, W. Wei, Y. Wang, B. J. Ni. A green synthesis of Ru modified g-C_3N_4 nanosheets for enhanced photocatalytic ammonia synthesis. Energy Materials Advances. 2021, 2021, 9761263.

11) **D. Hao**, T. Ma, B. Jia, Y. Wei, X. Bai, W. Wei. B. J. Ni. Small molecule π-conjugated electron acceptor for highly enhanced photocatalytic nitrogen reduction of BiOBr. Journal of Materials Science ＆ Technology. (Accepted) (JCR: Q1)

B: First-author Articles Under Consideration

12) **D. Hao**, Y. Wei, L. M, X. Bai, W. Wei. B. J. Ni. Boosted selective catalytic nitrate reduction to ammonia on carbon/bismuth/bismuth oxide photocatalysts. Journal of Cleaner Production. (Major revision) (JCR: Q1)

C: Co-author Peer-Reviewed Journal Articles

13) M. Ma, Y. Liu, Y. Wei, **D. Hao**, W. Wei. B.J. Ni. A facile oxygen vacancy and bandgap control of $Bi(OH)SO_4H_2O$ for achieving enhanced photocatalytic remediation. Journal of Environmental Management, 2021, 294, 113046. (JCR: Q1)

14) X. Bai, B. Sun, X. Wang, T. Zhang, **Q. Hao**, B.J. Ni, R. Zong, Z. Zhang, X. Zhang, H. Li. CrystEngComm. 2020. 22 (16), 2709-2717. (JCR: Q2)

15) W. Wei, L. Wu, X. Liu, Z. Chen, **Q. Hao**, D. Wang, Y. Liu, L. Peng, B.J. Ni. How does synthetic musks affect methane production from the anaerobic digestion of waste activated sludge? Science of The Total Environment. 2020, 713, 136594. (JCR: Q1)

16) A. Wang, W. Wang, J. Chen, R. Mao, Y. Pang, Y. Li, W. Chen, D. Chen, **D. Hao**, B.J. Ni, M. Saunders, G. Jia. Dominant Polar Surfaces of Colloidal II–VI Wurtzite Semiconductor Nanocrystals Enabled by Cation Exchange. Journal of Physical Chemistry Letters. 2020, 11 (13), 4990-4997. (JCR: Q1)

17) W. Wei, **Q. Hao**, Z.J. Chen, T. Bao, B.J. Ni. Polystyrene nanoplastics reshape the anaerobic granular sludge for recovering methane from wastewater. Water Research, 2020, 182, 116041. (JCR: Q1)

18) Z. Chen, I. Ibrahim, **D. Hao**, X. Liu, L. Wu, W. Wei, D. Su, B.J. Ni. Controllable design of nanoworm-like nickel sulfides for efficient electrochemical water splitting in alkaline media. Materials Today Energy, 2020, 18, 100573. (JCR: Q1)

19) X. Bai, X. Wang, X. Lu, Y. Liang, J. Li, L. Wu, H. Li, **Q. Hao**, B.J. Ni, C Wang. Surface defective g-C_3N_4-xCl_x with unique spongy structure by polarization effect for enhanced photocatalytic removal of organic pollutants. Journal of Hazardous Materials, 2020, 398, 122897. (JCR: Q1)

20) X. Liu, B. Xu, X. Duan, **D. Hao**, W. Wei, S. Wang, B.J. Ni. Facile preparation of hydrophilic In_2O_3 nanospheres and rods with improved performances for photocatalytic degradation of PFOA. Environmental Science: Nano. 2021, 8, 1010−1018. (JCR: Q1)

Abstract

Ammonia is a key industrial raw material for fertilizers, chemicals and energy. The annual artificial ammonia synthesis via the Haber-Bosch process causes about 2% of global energy consumption and can lead to 1.6% CO_2 emission. Therefore, it is urgent to develop low-cost and environmentally friendly approaches for artificial ammonia synthesis under ambient conditions. In this thesis, we summarized the current research status. Besides, a new concept of "artificial nitrogen cycle process based on photochemical and electrochemical reactions" was proposed. Through nanostructure control, metal modification, small π-conjugated molecule modification, plasma modification, several kinds of novel nanomaterials were developed and achieved highly efficient artificial ammonia synthesis under ambient conditions.

A facile approach was used to prepare defective g-C_3N_4 nanorods with a narrower bandgap and a sub-gap, which can significantly enhance the light utilization ratio. More importantly, the defects of g-C_3N_4 nanorods can also enhance light absorption and boost the cleavage of N_2 molecules, which is the rate-determining step of nitrogen fixation. Compared with bulk g-C_3N_4, the photocatalytic N_2 reduction rate of defective g-C_3N_4 nanorods as the catalysts was increased by 3.66 times.

We also report a novel bismuth bromide oxide (BiOBr)-Tetracyanoquinodimethane (TCNQ) photocatalyst prepared via a facile self-assembly method. Due to the well-match band structure of TCNQ and BiOBr, the separation and transfer of photogenerated electron-hole pairs were significantly boosted. The highest ammonia yield of the optimized sample reached 2.617 mg/h/g_{cat}, which was 5.6-fold as that of

pristine BiOBr and higher than the reported BiOBr-based photocatalysts.

Nitrate is a crucial environmental pollutant and its risk on the ecosystem keeps increasing. In this thesis, we reported a green and facile synthesis of novel metallic ruthenium particle modified graphitic carbon nitride photocatalysts. Compare with bulk graphitic carbon nitride, the optimal sample had 2.93-fold photocatalytic nitrate reduction to ammonia activity.

We also report a facile synthesis of carbon/bismuth/bismuth oxide photocatalyst via a one-pot hydrothermal reaction without using reducing reagent. Compared with bismuth oxide (α-Bi_2O_3), the photocatalytic ammonia yield of the optimum sample increased 3.65 times. In addition, the ammonia selectivity increased from 65.21% to 95.00%. The highly enhanced photocatalytic performance was attributed to the surface plasmon resonance of metallic bismuth. Meanwhile, the formation of carbon enables to boost the transfer of electrons significantly. The results and research findings of these works will contribute to the green artificial ammonia synthesis under ambient conditions.

Keywords: graphitic carbon nitride; bismuth; tetracyanoquinodimethane; bismuth bromide oxide; nitrogen reduction, nitrate reduction, photocatalysis; ammonia synthesis

Chapter 1 Introduction

1.1 Research background

Ammonia is a critical basic industrial material that has been massively used in the production of fertilizers, refrigerants and other chemicals. Every year, 750,000 tons of ammonia is produced and 88% of which are used as fertilizers (Giddey, Badwal & Kulkarni 2013; Lassaletta et al. 2014; Polikhronidi et al. 2009). Besides the application in fertilizers, ammonia is also a building block in refrigerants, pharmaceutical industries, cleaning products and other chemicals. In addition, the standard enthalpy change of combustion of ammonia is -316.8 kJ/mol, which is indeed higher than that of H_2 (-286 kJ/mol) (Council 2004; Kobayashi et al. 2019). More importantly, the complete combustion of NH_3 can only produce N_2 and H_2O, thus it is a highly potential clean fuel with high calorific value (Maffei et al. 2005; Siddiqui & Dincer 2017). With the rapid increase of the global population, the gap between naturally formed NH_3 to human demand amount is increasing. In 1909, the Haber-Bosch process was invented, which was the first time that people could obtain NH_3 on a large industrial scale. To accomplish this process, extreme conditions are required, counting high temperature (400–500 °C) and high pressing factor (15–25 MPa). What makes matters worse, the hydrogen source comes from the water gas shift reaction, which not only consumes a lot of fuel but also produces a lot of CO_2 (Leigh 2004b). Thus, researchers are keeping developing less minimal expense and more eco-accommodating methodologies for the artificial nitrogen fixation under surrounding conditions. Very recently, photocatalytic nitrogen fixation has attracted increasing attention (Wang, Qiu, et al. 2020; Yan et al. 2019). Photocatalysis is the speed increase of photoreactions carried by the photoinduced electron-hole pairs and their secondary redox reactions (Alshammari & Jiang 2016). It has wide applications in energy and environmental areas (Fu et al. 2019;

Saravanan et al. 2015).

Compared with the Haber-Bosch process, photocatalytic nitrogen reduction use water (H_2O) as the hydrogen source, which can significantly reduce energy consumption and CO_2 emission. In addition, these reactions usually occur under ambient conditions, without the requirement of high pressure and high temperature (Guo et al. 2019). Besides nitrogen gas, some other nitrogen-based chemicals like nitrogen oxides, nitrite and nitrate can also be used for ammonia synthesis, which can not only generate useful ammonia, but also eliminate the environmental pollutants(Choi et al. 2019). However, due to the low ammonia yield rate, the research on the topic is still limited in lab scale. It is urgent to develop novel materials to enhance the artificial ammonia synthesis efficiency.

Graphitic carbon nitride is a kind of metal-free semiconductor, which has a ton of benefits including high stability, nontoxicity, easy and minimal expense synthesis, proper bandgap in the visible spectral range and wide accessibility of resources. It is a high-potential candidate for the photochemical synthesis of ammonia. However, g-C_3N_4 has an absorbance edge at 460 nm and it cannot absorb solar photons with the wavelength beyond this value, therefore, the light utilization of this material is not high (Bai et al. 2018; Gao, Cao, et al. 2019; Gao et al. 2018). Meanwhile, the rapid recombination of photoinduced electron-hole pairs in bulk g-C_3N_4 obstructs its catalytic performance. g-C_3N_4 is usually prepared by the calcination of nitrogen-rich precursors, and it always shows a bulk structure because of the Van der Waals forces between its layers (Bai et al. 2014). By adjusting the microstructure and compounding with other materials, the catalytic activity of carbon nitride can be greatly improved, which is

helpful for its wide application.

Bismuth is the 83rd element in the periodic table. Compared with most of other heavy metals, bismuth has the advantage of non-toxicity (Dong et al. 2014). In recent years, bismuth-based semiconductor photocatalysts including bismuth oxides, bismuth oxyhalides, and bismuth-based polyoxometalates have attracted increasing interests because of the distinct crystal structure as well as the unique electronic structure (Hsieh et al. 2012; Kong et al. 2016; Liu, Jiang, et al. 2018; Sheng et al. 2020). Meanwhile, metallic bismuth has surface plasmon resonance like noble metals, which makes bismuth a good co-catalyst for photocatalytic reactions (Dong et al. 2014; Hao, Wang, et al. 2017). Based on the structure characteristics, bismuth-based materials have huge potential in achieving highly-efficient artificial ammonia synthesis under ambient condition. Nevertheless, the current photocatalytic activity of bismuth-based materials is still a long way far from large-scale application, and strategies should be developed to enhance the photocatalytic ammonia synthesis efficiency of bismuth-based semiconductors.

With the energy and environmental crisis being increasingly serious, it is highly urgent to develop novel nanomaterials to minimize the carbon dioxide emission caused by the Haber-Bosch process. Photocatalytic technology might be one of the best candidates to achieve this target. Therefore, the development of high-performance photocatalysts is in emergency. In this thesis, we report some novel g-C_3N_4 and bismuth-based nanomaterials with remarkable photocatalytic performance on ammonia synthesis. Via

controlling the structure and components of materials, the photocatalytic activity improved a lot. A series of characterizations were used to study the mechanisms systematically. The results and findings of these work can contribute to the research on nanotechnology and ammonia synthesis under ambient condition.

1.2 Objectives and scopes

Currently, because of the repaid recombination of electron-hole pairs, the competitively low solar energy usage and the stability issue of photocatalysts, the research gap on artificial ammonia synthesis between laboratory-scale research to mass production is still huge. The scopes of the research are to develop several novel semiconductor photocatalysts to narrow the research gap. The exact objectives are listed below:

- Develop a facile approach to synthesize one-dimensional g-C_3N_4 nanorods to regulate the separation and transfer of electron-hole pairs to achieve highly efficient photochemical nitrogen fixation.

- Use small molecule π-conjugated electron acceptor to modify BiOBr to achieve highly efficient photochemical nitrogen fixation.

- Invent a green and facile approach to synthesize metallic elements modified g-C_3N_4 nanosheets to improve the photocatalytic nitrate reduction to ammonia efficiency and selectivity.

- Establish a facile preparation of metallic bismuth modified photocatalyst and use the surface plasmon resonance

1.3 Research significance

The scopes and objectives were set to narrow the research gap between laboratory-scale research and mass application on photocatalytic ammonia synthesis. Based on abundant literature reviewed, we clarified the relationship between the crystal structure bismuth-based materials and high potential on artificial nitrogen fixation. The differences between using nitrogen and nitrate as nitrogen source for ammonia synthesis were systematically analyzed. A new concept "artificial nitrogen cycle processes through novel electrochemical and photochemical synthesis" was proposed. Through nanostructure control, metal modification, small π-conjugated molecule modification, plasma modification, several kinds of novel nanomaterials were developed and achieved highly efficient artificial ammonia synthesis under ambient condition. The results of these research are of great significance and will contribute to the research on nanotechnology, chemistry, materials science and environmental engineering.

1.4 Structure of the thesis

Chapter 1. Introduction includes research background, objectives and research significance.

Chapter 2. Literature review about materials and methods to achieve highly efficient artificial ammonia synthesis.

Chapter 3. Materials preparation and characterizations.

Chapter 4. Surface defect-abundant one-dimensional graphitic carbon nitride nanorods

boost photocatalytic nitrogen fixation.

Chapter 5. Small molecule π-conjugated electron acceptor for highly enhanced photocatalytic nitrogen reduction of BiOBr.

Chapter 6. A green synthesis of Ru modified g-C_3N_4 nanosheets for enhanced photocatalytic ammonia synthesis from nitrate.

Chapter 7. Boosted selective catalytic nitrate reduction to ammonia on carbon/bismuth/bismuth oxide photocatalysts.

Chapter 8. Summarization of the main results of the works and suggestions for future development.

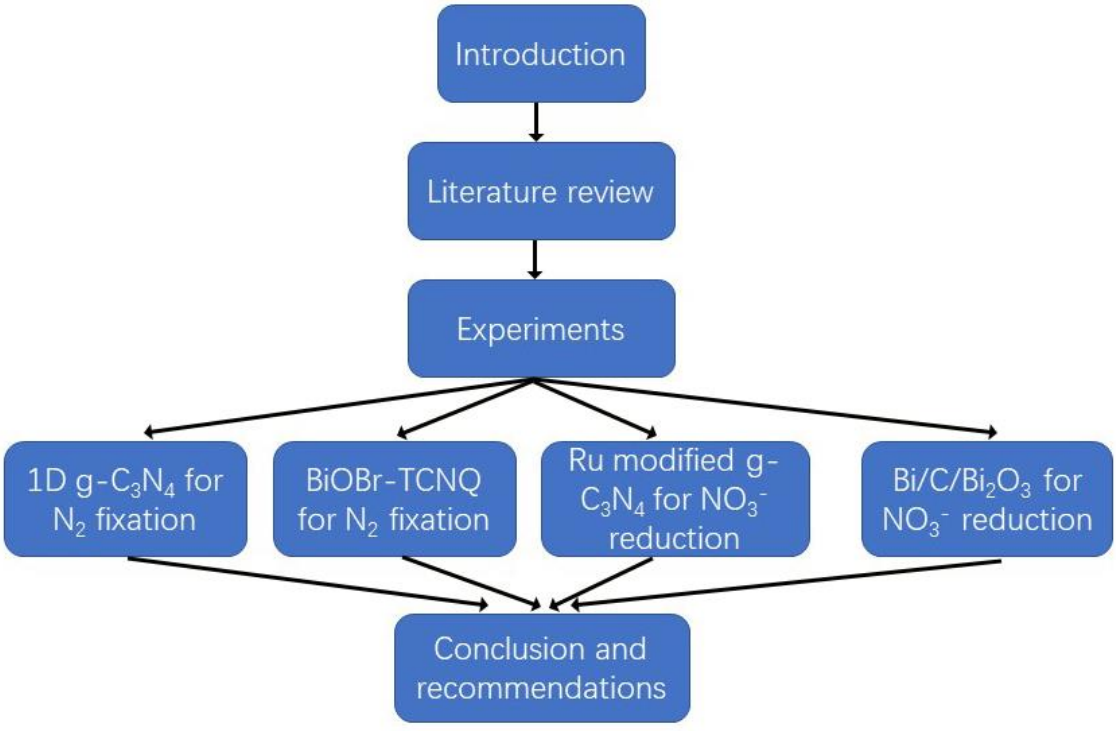

Diagram 1. The detailed structure of the thesis.

Chapter 2. Literature review

Related publications:

Graphitic carbon nitride with different dimensionalities for energy and environmental applications. Nano Research. 2020. 13, 18-37.

Catalytic reduction of nitrogen to produce ammonia by bismuth-based catalysts: state of the art and future prospects. Materials Horizons. 2020, 7 (4), 1014-1029.

Emerging alternative for artificial ammonia synthesis through catalytic nitrate reduction. Journal of Materials Science & Technology. 2021, 77, 163-168.

Emerging artificial nitrogen cycle processes through novel electrochemical and photochemical synthesis. Materials Today. 2021, 46, 212-233.

2.1 Introduction

Nitrogen is very important for the growth of plants. Proper application of nitrogen fertilizers can promote the growth of crops, increasing the protein content and yield amounts of grains. With the explosive growth of population, human demand for food has reached an unprecedented amount. Naturally formed NH_3 is not enough to support the world's agricultural industry. Since the invention of the Haber-Bosch process, a large amount of NH_3 has been produced, 90% of which is used to produce fertilizers, thereby providing sustainable food production for over 7 billion people (Erisman et al. 2008). Meanwhile, ammonia also has wide application as a fuel or hydrogen carrier (Wang et al. 2013). The decomposition of ammonia is a low-cost and facile process. So

using NH_3 as a H_2 transporter is able to solve the hydrogen stockpiling problem to a certain extent (Zhao et al. 2019). However, the Haber-Bosch process requires high pressure (15–25 MPa) and high temperature (400–500 °C) (Kandemir et al. 2013; Leigh 2004b). Every year, the production of NH_3 by Haber-Bosch process can consume 2% global energy and cause 1.6% CO_2 emission (Guo et al. 2019). To solve the energy and environmental crisis caused by ammonia industry, it is urgent to develop cost effective methods for NH_3 synthesis under surrounding conditions.

Since the abuse of fertilizers, the groundwater is facing challenge. The chemical forms of nitrogen in fertilizers are mainly in NO_3^-, NO_2^-, NH_3, NH_4^+, and urea.(Scherer et al. 2000) The crops can only utilize a small amount of nitrogen of the artificial fertilizers. As a result, a considerable amount of nitrogen elements flow into both surface water and groundwater, causing serious environmental problems. The nitrogen of polluted groundwater is usually nitrate. If we can use the nitrate polluted water as nitrogen source for artificial ammonia synthesis, it would be more sustainable and environmentally friendly.

2.2 Photocatalytic synthesis of ammonia

2.2.1 Photochemical nitrogen fixation

Considering the mentioned energy and environmental problems, photocatalytic technology may be one of the best approaches to overcome the crisis caused by ammonia industry. In 1972, Japanese scientist Fujishima found that TiO_2 had the electrochemical photolysis, which opened the avenue of photocatalysis (Fujishima &

Honda 1972). Photocatalysis is the speed increase of photoreactions carried by the photogenerated electron-hole pairs and the secondary reactions (Alshammari, Jiang & Cordova 2016). Thus it has wide applications for various redox reactions, including water splitting, CO_2 reduction, nitrogen fixation etc. (Han et al. 2018; Liu, Wang, et al. 2019; Zhou, Shi, et al. 2018).

Comprehension of N_2-fixation pathways and mechanisms is very important for research on this topic. Currently, there are three kinds of mechanisms for the N_2 reduction process, including the dissociative, associative and enzymatic mechanism.(Guo et al. 2019; Li, Li, et al. 2016) In the dissociative process, N≡N is initially cleaved, and after that, NH_3 will be gradually formed via hydrogenation (**Figure 2.1a**). It is what happens of the Haber–Bosch process. While in the associative mechanism, the 2 nitrogen centres in N_2 are kept bound to each other before the broken of the final N–N bond. There are 2 pathways in the associative mechanism called the distal pathway and the alternating pathway. In the distal pathway, hydrogenation may react in preference to the nitrogen further from the catalyst. As a result, one equivalent of NH_3 will be released, and a metal nitride will remain until hydrogenation yields the last equivalent of NH_3 (**Figure 2.1b**). In the alternative pathway, each of the 2 nitrogen centres undergoes single hydrogenation in sequence till one nitrogen is converted to ammonia and the N–N bond is broken (**Figure 2.1c**). For nitrogenases and some kinds of catalysts, the N_2 molecules are adsorbed by the two edges rather than one side on the surface of nitrogenases/catalysts (**Figure 2.1d**). And the hydrogenation will occur to both the N atoms at the same time. When the last N–N is broken, NH_3 molecules will be released.

$$N_2\,(g) + 3H_2 \leftrightarrow 2NH_3\,(g) \qquad (1)$$

$$N_2\,(g) + 6H^+ + 6e^- \leftrightarrow 2NH_3\,(g) \quad (2)$$

$$N_2\,(g) + 8H^+ + 6e^- \leftrightarrow 2NH_4^+\,(aq.) \quad (3)$$

$$N_2\,(g) + 8H_2O\,(l) + 6e^- \leftrightarrow 2NH_3{\cdot}H_2O\,(aq.) + 6OH^-\,(aq.) \quad (4)$$

The catalytic N_2 fixation usually involves several steps. As shown in equation (1), the NH_3 synthesis reaction is an exothermic reaction whose enthalpy change is 93 kJ/mol. Equation (2) shows that the reaction of nitrogen and hydrogen to produce gaseous NH_3 has a certain degree of spontaneity, with a potential of +0.0577 V. In acidic conditions, such as pH = 0, NH_3 gas becomes dissolved NH_4^+ ions. The whole reaction is shown in equation (3), which has a positive potential difference between +0.274 V. When the generated NH_3 is $NH_3{\cdot}H_2O$, the reaction potential is +0.092 V (Equation 4). According to equation 1-3, it can be conducted that it is easier to synthesize NH_3 in acidic conditions because the NH_3 synthesis reaction has a higher thermodynamic potential in acidic conditions. Nevertheless, the N_2 reduction reaction is a 6-electron process with blended steps, and any step with a high energy barrier will make the reaction obstructed.

$$N_2\,(g) + 5H^+ + 4e^- \leftrightarrow N_2H_5^+\,(aq.) \quad (5)$$

$$N_2\,(g) + 4H_2O\,(l) + 4e^- = N_2H_4\,(aq.) + 4OH\,(aq.) \quad (6)$$

$$N_2\,(g) + 2H^+ + 2e^- \leftrightarrow N_2H_2\,(g) \quad (7)$$

$$N_2\,(g) + H^+ + e^- \leftrightarrow N_2H\,(g) \quad (8)$$

$$N_2\,(g) + e^- \leftrightarrow N_2^-\,(aq.) \quad (9)$$

Besides the 6-electron process, there are several subprocesses of the N_2 reduction

reaction. The 4-electron process of N_2 reduction can be divided to two conditions, including the high-pH condition (pH > 6.07) and low-pH condition (pH < 6.07). When pH < 6.07, the product is $N_2H_5^+$, and the total potential of the reaction is −0.214 V, which also means that the energy barrier of the whole reaction is 0.214 V (Equation 5). When pH > 6.07, the reaction product is N_2H_4, the potential is −0.332 V, and the total reaction energy barrier is 0.332 V (Equation 6). In terms of the thermodynamic changes of the initial state and the final state, it is a process that cannot react spontaneously. The product of the 2-electron process in N_2 reduction is N_2H_4, and the potential is −1.10 V (Equation 7). The product of the single-electron process in N_2 reduction is N_2H, with a potential of −3.2 V (Equation 8). The first electron transfer and proton coupling process of nitrogen reduction have the largest thermodynamic energy barrier of 3.2 V. The energy barrier for directly receiving an electron of nitrogen molecules is higher, and it is 4.16 V (Equation 9). In alkaline conditions (pH = 14), the energy barrier is slightly lower, with a value of 3.37 V.

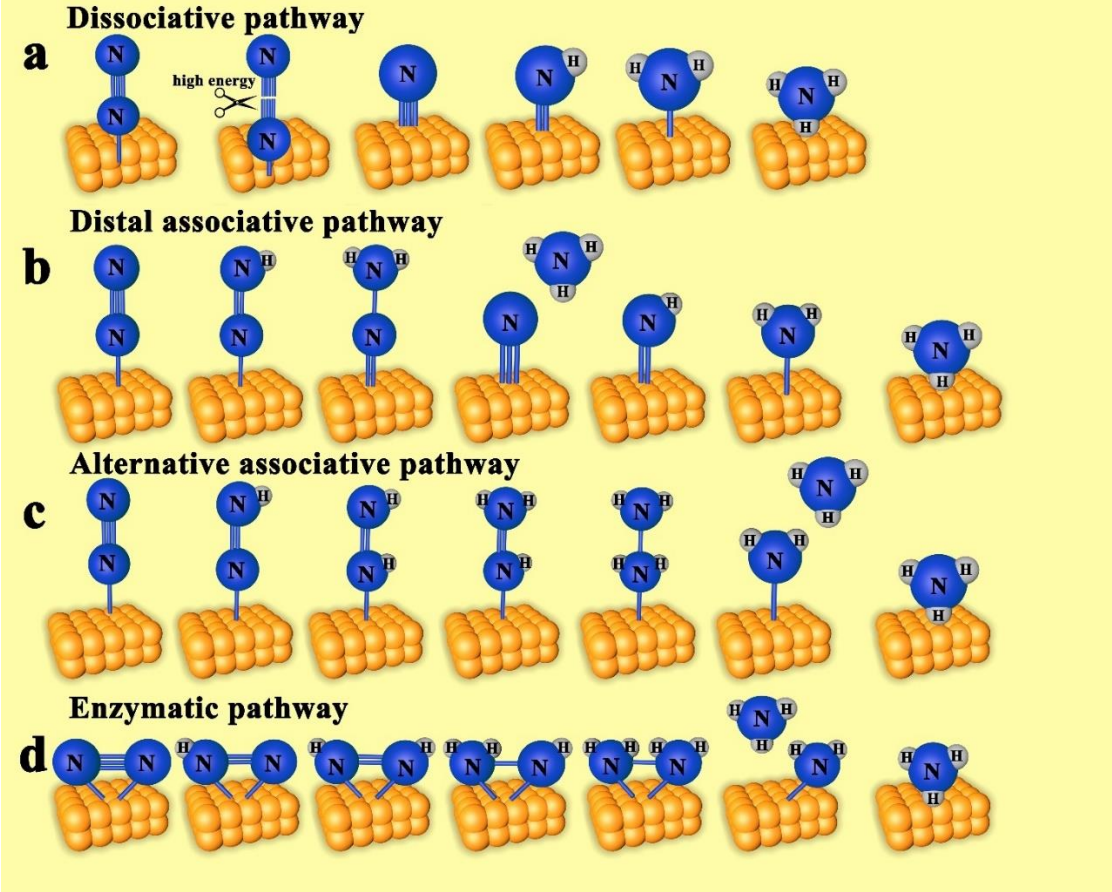

Figure 2.1 The pathways of nitrogen fixation to ammonia (a) dissociative pathway, (b) distal associative pathway, (c) alternative associative pathway, and (d) enzymatic pathway.

Titanium oxide is a superstar of photocatalysts, and it has been firstly reported to be a kind of N_2-fixation photocatalyst (Comer & Medford 2018; Hao et al. 2020; Zhao et al. 2014). While due to the poor solubility of N_2 in aqueous solution, the strong and stable N≡N, and the competing hydrogen evolution reaction (HER), the NH_3 yield rate is obstructed in laboratory-scale.

Recently, many novel materials and approaches have been developed to overcome the mentioned difficulties to improve the NH_3 yield rate. For example, pure bismuth bromide oxide (BiOBr) nearly has no photocatalytic N_2 fixation activity. While Li et al. designed a novel (001) facets exposed and oxygen vacancies enriched BiOBr nanosheet, which can reach the photocatalytic NH_3 yield rate of 104.2 μmol/h (Li et al. 2015). It is

attributed to that the oxygen vacancies can help to activate and cleave the N_2 molecules. Creating oxygen vacancies on the exterior of other semiconductors can also effectively boost the N_2 fixation performance, as electrons can be accumulated at the vacancy sites, leading to the activation and extension of N≡N. For instance, Zhang et al. prepared a kind of Fe-doped BiOCl nanosheet with remarkable photocatalytic N_2 fixation performance, which is attributed to the oxygen vacancies and the doped Fe element (**Figure 2.2**) (Zhang, Li, et al. 2019). Some iron-based semiconductors, alloys and g-C_3N_4-based photocatalysts also showed significant potential application prospects.(Lashgari & Zeinalkhani 2017; Liu, Wang, et al. 2019; Mou et al. 2019; Tennakone, Thaminimulla & Bandara 1992) However, there is a magnitude difference between photocatalytic and electrochemical N_2 reduction to NH_3 rates.

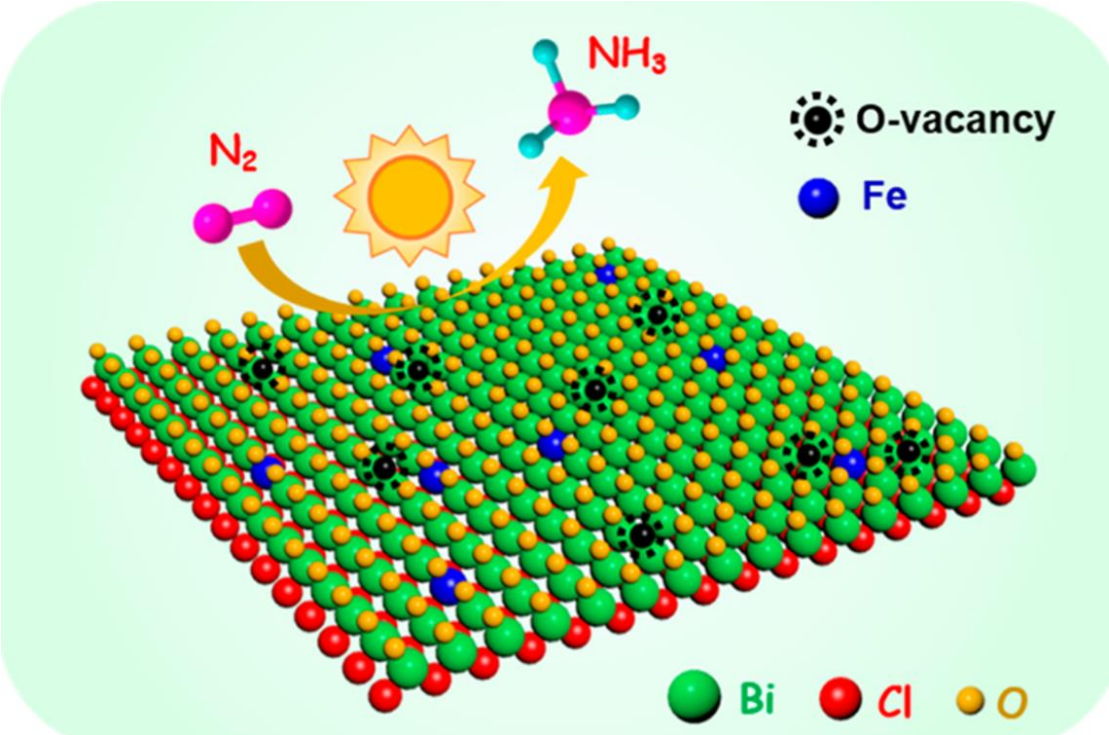

Figure 2.2 Scheme for the photochemical N_2 fixation on the surface of Fe-doped BiOCl nanosheet. Reproduced with permission. (Zhang, Li, et al. 2019) Copyright 2019, American Chemical Society.

2.2.2 Limits of artificial N_2 fixation

The catalytic reaction system for synthesizing ammonia usually consists of the catalysts and water, and there are a few key factors that limit the yield of ammonia. Firstly, the low solubility of N_2 in aqueous solution (20 mg/L, 20 °C, 100 kPa) greatly limits the contact area and time between the catalysts and the N_2 in the water, thereby limiting the rate of N_2 fixation (**Figure 2.3a**). Secondly, it is very difficult for N_2 molecules to be strongly adsorbed and activated on the surface of catalysts, as it has stable chemical properties (**Figure 2.3b**). Thirdly, the competitive HER can rip electrons, reducing the selectivity of N_2 fixation. Oshikiri et al. reported an Au nanoparticle modified $SrTiO_3$ photoelectrode for N_2 fixation under visible light irradiation (Oshikiri, Ueno & Misawa 2014). In this system, the following two reactions proceed:

$N_2 + 6H^+ + 6e^- \rightarrow 2HN_3$ (1) U° (N_2/NH_3): -0.092 V vs RHE

$2H^+ + 2e^- \rightarrow 2H_2$ (2) U° (H^+/H_2): 0 V vs RHE

As the standard redox potential of N_2 reduction is more negative than that of HER, the competitive HER is a significant barrier for N_2 reduction (**Figure 2.3c**). While Bi-based catalysts have many advantages (i.e., unique structure to capture and activate N_2, low adsorption energy of H_2, etc.) in solving these limiting factors, the Bi-based catalysts may form a unique and effective platform in N_2-reduction area.

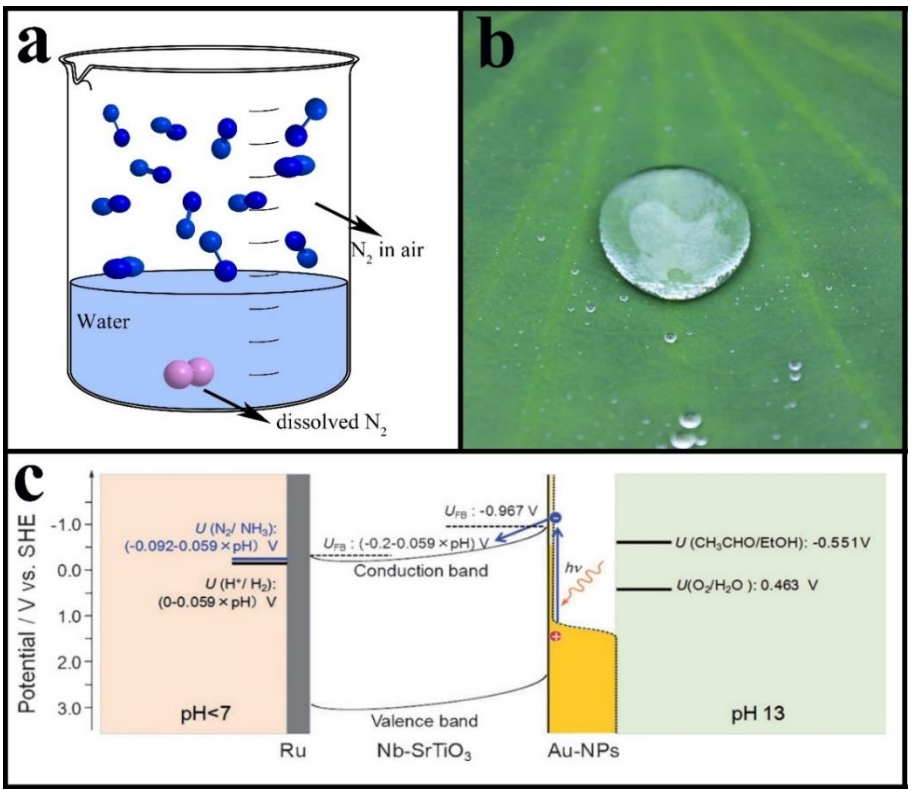

Figure 2.3 (a) Schematic of dissolved N_2 in water; (b) diagram of N_2 on the clean surface of catalysts which is being analogous to water on the surface of hydrophobic lotus leaf; (c) energy diagram of the plasmon-induced photocatalytic nitrogen reduction system using $SrTiO_3$ substrate with Au particles. (c) Reproduced with permission (Oshikiri, Ueno & Misawa 2014). Copyright 2014, Wiley-VCH.

2.2.3 Nitrate reduction

NO_3^- and NO_2^- are naturally occurring ions that are part of the nitrogen cycle. As mentioned, about 90% of NH_3 is used in fertilizers. While the crops can only utilize a small amount of nitrogen of the artificial fertilizers. As a result, a large amount of NO_3^- flow into both surface water and groundwater, which causes a lot of environmental problems. Compared with N_2 fixation, nitrate reduction is regarded as a more promising approach, which may replace the Haber-Bosch process. Currently, the direct N_2 reduction is obstructed in laboratory scale as the low NH_3 yield rate (0.1 to 100 ug/h/mg_{cat}) (Guo et al. 2019). The key reasons that hinder the catalytic NH_3 yield efficiency include the poor solubility of N_2 in water, the hard cleavage of N≡N, and the competing HER. The solubility of nitrites or nitrates is nearly 40000-fold as that of N_2

gas, which can ensure the N source continuously delivered to the surface of the catalysts. The dissociation of N=O (204 kJ/mol) is much easier than that of N≡N (941 kJ/mol), indicating that the catalytic reduction of NO_3^- or NO_2^- is much easier (Wang, Zhou, et al. 2020; Wang, Yu, et al. 2019). What is more, if N_2 gas is replaced by NO_3^- or NO_2^-, the residual NO_3^- and NO_2^- contaminations in water systems can be efficiently eliminated and converted to energy sources at the same time.

The nitrate reduction pathway mainly contains three productions, including nitrogen oxides, N_2 and NH_3. The formation of N_2 is a 5-electron process, and the generation of NH_3 is an 8-electron process (Equation 10 and 11).(Hirakawa et al. 2017) During the NO_3^- reduction pathway (**Figure. 2.4**), the adsorbed NO_3^- was first reduced to NO_2^- by getting one electron (Equation 12). With further electron acceptation, the NO_2^- will become NO_2^{2-} and react with H_2O to generate NO (Equation 13 and 14). Meanwhile, NO_2^- can also be converted to HONO, which can further react to generate N_2O_4 and N_2O. Then what will happen is regarded as the selectivity-determining step. The NO may react with H_2O to form HN_2O_2 or HNO, which are considered as the intermedia of the formation of N_2O, N_2 and NH_3, respectively. At the same time, NO can take part in other reactions to generate N_2 and N_2O.(Garcia-Segura et al. 2018) The used materials, pH value, voltage all have a significant influence on the reaction selectivity.

$$2\ NO_3^- + 12\ H^+ + 10\ e^- \rightarrow N_2 + 6\ H_2\ E^0 = 1.17\ V\ vs\ SHE \quad (10)$$

$$NO_3^- + 9\ H^+ + 8\ e^- \rightarrow NH_3 + 3\ H_2\ E^0 = -0.12\ V\ vs\ SHE \quad (11)$$

$$NO_3^- + 2\ H^+ + 2\ e^- \rightarrow NO_2^- + H_2O\ E^0 = 0.01\ V\ vs\ SHE \quad (12)$$

$$NO_{2\ (ad)}^- + e^- \rightarrow NO_{2\ (ad)}^{2-}\ E^0 = -0.47\ V\ vs\ SHE \quad (13)$$

$$NO_{2\ (ad)}^{2-} + H_2O \rightarrow NO_{(ad)} + 2\ OH^- \quad (14)$$

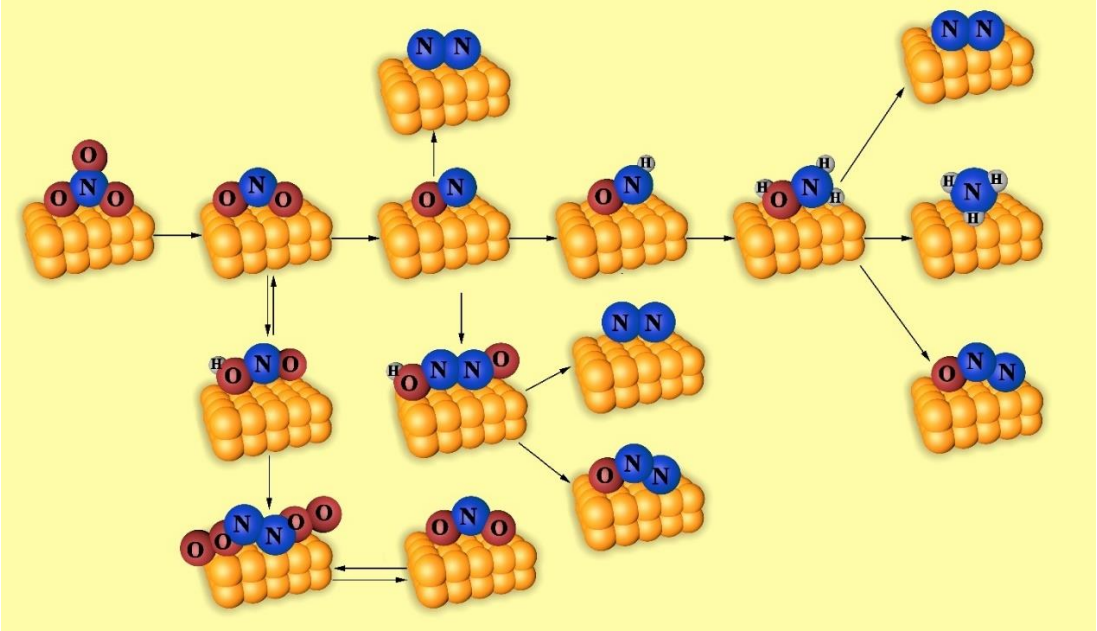

Figure 2.4 The main pathways and products of the reduction of NO_3^-.

If the waste NO_3^- can be converted to valuable chemicals and utilized, it will be more sustainable and more eco-friendly for the environment. Under light irradiation, the photogenerated electrons can take part in the NO_3^- reaction. With some organic electron donors added, the photocatalytic induced holes can react with the scavengers to form $CO_2^{\bullet-}$. For instance, Tong et al. fabricated a PdSn/NiO/$NaTaO_3$: La photocatalyst, which exhibited 100% NO_3^- conversion with an NH_3 selectivity of 72% (**Figure 2.5a**) (Tong et al. 2018). The excellent results are referred to the high adsorption energy of NO_2^- on NiO and the highly efficient charge separation. Herein, formic acid was employed as a hole scavenger to increase the utilization rate of photogenerated charge carriers. At the same time, some achievements have been realized in the development of materials. For example, Choi et al. prepared a new metal-organic framework named MOF NU-1000, which exhibited 89% selectivity for the photocatalytic nitrate reduction to ammonia (**Figure 2.6**) (Choi et al. 2019).

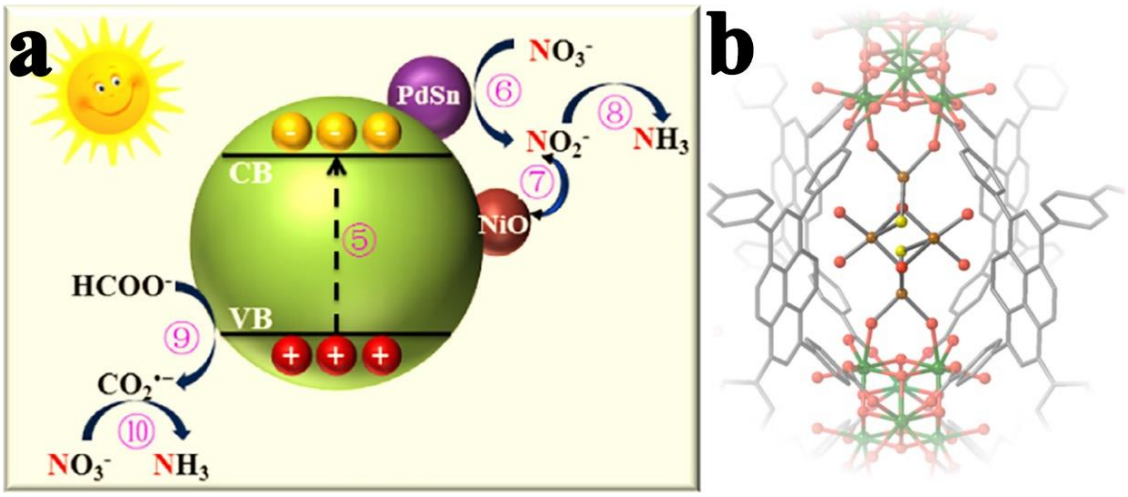

Figure 2.5 (a) The scheme of photoinduced NO_3^- reduction on PdSn/NiO/$NaTaO_3$: La. Reproduced with permission (Tong et al. 2018). Copyright 2018, Elsevier. (b) The structure of MOF-supported iron thiolate cluster (Zr, green; O, red; C, gray; S, yellow; Fe, orange). Reproduced with permission (Choi et al. 2019). Copyright 2019, American Chemical Society.

2.3 g-C_3N_4 photocatalysts

The study of CN can be dated back to 1834 when Berzelius firstly prepared a linear CN material and called it as "melon" (Liebig 1834; Zhou, Zhang, et al. 2018). Since then, the investigation of CN has begun. In 1922, Franklin discovered a type of g-C_3N_4 by the thermal calcination of mercuric thiocyanate (Franklin 1922). In 1989, it was predicted that if C would supplant Si in the construction of β-Si_3N_4, a super hard β-C_3N_4 material could be gotten (Liu & Cohen 1989). In 1996, Teter and Hemley affirmed five types of CN with different phases including α-C_3N_4, β-C_3N_4, c-C_3N_4, p-C_3N_4 and g-C_3N_4 (Figure 2.6) (Teter & Hemley 1996). According to the crystal structure, the CNs are all super hard materials except for g-C_3N_4 (Zhang, Wang & Wang 2013). Thus, it is much easier to adjust the morphology and structures of g-C_3N_4. As a result, the study of g-C_3N_4 became a hot topic, and many kinds of g-C_3N_4 with various structures and functionalities have been reported.

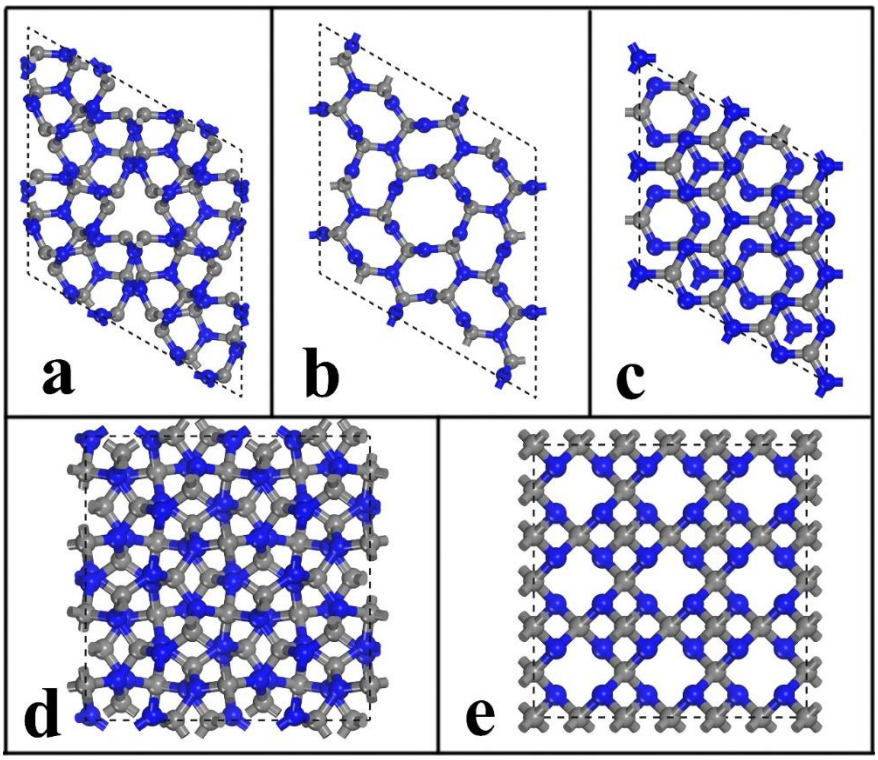

Figure 2.6 Structure of (a) α-C_3N_4, (b) β-C_3N_4, (c) g-C_3N_4, (d) cubic-C_3N_4 and (e) pseudocubic-C_3N_4 view from the [001] axis.

In g-C_3N_4, C and N atoms are sp^2 hybridised. They are both associated by the σ bonds, leading to the generation of a hexagonal structure. The hexatomic ring is named triazine ring. In g-C_3N_4, each triazine ring is connected by the N atom at the end, generating an infinitely expanded planar grid structure. In these two allotropes (**Figure 2.7**), the electronic structure and thermodynamic stability are different because of the different-sized nitrogen holes in the structure. It is reported that the g-C_3N_4 with the tri-s-triazine ring is more thermodynamically stable than that with triazine structure (Kroke et al. 2002).

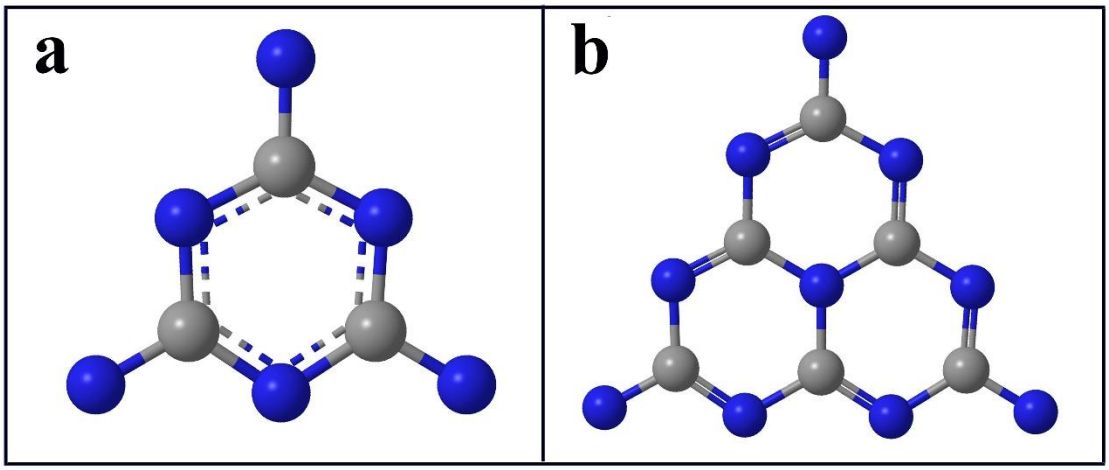

Figure. 2.7 Triazine-(a) and tri-s-triazine-based connection patterns (b) of potential g-C_3N_4 allotropes.

In these two types of g-C_3N_4, both C and N atoms belong to sp^2 hybridisation, which can form highly conjugated π bonds with the lone electron pairs on Pz orbitals. As a result, a highly delocalized conjugated system is composed. The absorption edge of g-C_3N_4 is about 460 nm and its bandgap is about 2.7 eV, with the CB at -1.13 eV and the VB at +1.74 eV (Lu, Wang, et al. 2018).

Since the low-coordinated N atoms contribute to both the CB and VB, the significant π bonds formed have low delocalisation, which is one of the main reasons for the relatively high electron-hole recombination rate of bulk g-C_3N_4. Generally, thermal calcination of precursors is the most commonly used techniques to prepare g-C_3N_4. However, the obtained g-C_3N_4 is usually bulk and non-porous in nature with a strong Van der Waals forces between CN layers. As a result, the bulk g-C_3N_4 exhibits poor specific surface area with irregular stacking of thick layers, which significantly restricts its application in catalysis due to the limited contact area with reactants. Besides, the

calcined g-C_3N_4 has a low polymerisation degree, low crystallinity and abundant surface defects, which deteriorate its performances and impede its widespread applications in various fields covering sensing, adsorption and separation and catalysis. The dimension of g-C_3N_4 is another important factor that can be controlled by altering the synthesis parameters. The control of dimensions plays an important role in the catalytic activity of these nanostructures towards highly efficient photocatalytic ammonia synthesis, as the effects on the specific surface area, pore structure, light absorption properties, transfer path, and separating speed of electron-hole pairs of the g-C_3N_4. Research on this topic needs further investigation.

2.4 Bi-based photocatalysts

As active materials for photocatalytic ammonia synthesis, Bi-based materials including metallic bismuth, bismuth oxide, bismuth oxyhalide, and bismuth molybdate have been extensively studied particularly due to their advantages of being non-carcinogenic and non-toxic as well as their excellent catalytic properties in many fields (Li, Tang, et al. 2019; Sun et al. 2017; Xue et al. 2018). Compared with common photocatalysts (TiO_2, g-C_3N_4 etc.) and electrocatalysts (porous C-N, Pt/C etc.), Bi-based showed significantly higher performance, which is caused by its strong chemical interaction with N_2 molecules (Sun et al. 2017).

2.4.1 Metallic Bi

The atomic number of Bi in the periodic table of elements is 83 (Meija et al. 2016). Unlike its ortho-elements, the 82nd of lead and 84th elements of polonium which are

toxic, Bi is a non-poisonous substantial metallic component. The crystal structure of Bi **Figure 2.8a** shows that it belongs to the trigonal crystal system (a = b = 4.53 Å, c = 11.81 Å) and R3m (166) space group (Cucka & Barrett 1962). Bulk metallic Bi is a semimetal with direct plasmonic effect (Dong et al. 2014). For the advances of long Fermi wavelength, rapid transporter motilities and SPR effect, it has drawn a ton of exploration interests, especially in the study of photocatalysis and electrocatalysis (Dong et al. 2015). Due to the quantum confinement phenomena and low energy overlap of Bi, it can be converted to semiconductor from semimetal when it becomes thin films (Hoffman et al. 1993; Yang et al. 1999). Very recently, researchers found that metallic Bi can be used in electrocatalytic N_2 reduction (Li, Tang, et al. 2019). The semiconducting Bi is less-reactive in HER reaction due to the high free energy barrier of adsorption between Bi and H_2 (Greeley et al. 2006). The solid connection between the *p* orbitals of Bi and N permits N_2 to be selectively adsorbed on its surface, which contributes to the dissociation of N≡N (Hao et al. 2019). Besides, Bi atoms in Bi-based catalysts are able to confine the density state around its Fermi level, and it implies that Bi atoms can provide more active centres for activating N_2 by donating *p*-electrons (Sun et al. 2017). At the same time, Bi is able to decrease the free-energy change in the potential-determining step (Hao et al. 2019). The above facts are all favourable for the N_2 reduction reaction. Furthermore, Hao et al. found that Bi and K^+ pairs can ulteriorly reduce the reactional free-energy change, adjust the proton diffusion process, stabilize intermediates of N_2 reduction and boost the N_2 fixation efficiency (Hao et al. 2019). It has been confirmed that two-dimensional Bi nanosheets with ample edge sites and

delocalized *p*-orbital electrons show excellent electrocatalytic performance of N_2 fixation (Li, Tang, et al. 2019). It has also been found that surface defects can influence the N_2 fixation performance of metallic Bi. Wang et al. prepared Bi nanoplates by the reduction of Bi_2O_3 (**Figure 2.8b**). As shown in the Gibbs-free-energy diagrams (**Figure 2.8c**), the ΔG_{N2H}* of defective Bi (110) is much smaller than that of prefect Bi (110). The HER performances of different catalysts listed in **Figure 2.8e** demonstrate the hydrogen-generation activity of Bi is poor, due to its low adsorption energy of H. The activation energy of N_2 of the ideal Bi (110) is 1.03 eV, while it can be reduced to 0.56 eV on the surface of defective Bi (110) (**Figure 2.8f**), indicating that N_2 can be more easily and dynamically fixated on defective Bi (110) (Wang, Shi, et al. 2019a).

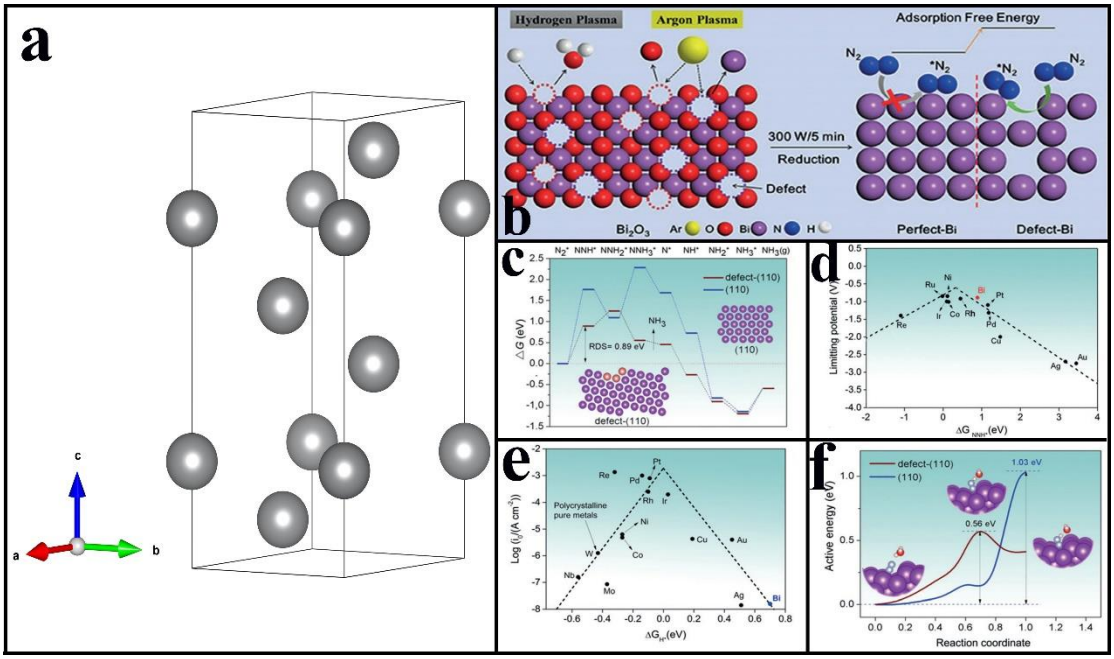

Figure 2.8 (a) The crystal structure of metal Bi from standard orientation, (b) Scheme of the defective Bi nanoplates for the N_2 fixation reaction, (c) The free-energy charts for the N_2 fixation response on Bi(110) and Bi(110) features through a response pathway, and (d) Limiting potentials for nitrogen reduction on different metals vs. the binding energy of N_2H*; (e) Volcano plot for the HER on representative transition metals; (f) activation energy of the rate-determining step. (b-f) Reproduced with permission (Wang, Shi, et al. 2019a). Copyright 2019, Wiley-VCH.

2.4.2 Bismuth Oxide

Previously, δ-Bi_2O_3 and BiO have been reported to be active for N_2 fixation under ambient condition.(Gao, Shang, et al. 2019a, 2019b; Sun et al. 2017). **Figure 2.9a** shows the defective fluorite-prototype of δ-Bi_2O_3, which belongs to the cubic crystal system (a = b = c = 5.53 Å) and Pn3m (224) space group. Different from CaF_2, here are just 6 oxygen atoms present in the stoichiometric compound to involve the 8 comparable anion destinations, leaving 25% of the oxygen lattice sites inherently empty (Music, Konstantinidis & Schneider 2009). Such natural oxygen-vacancy structure may lead to superior catalytic performance (**Figure 2.9b**). The valence band of δ-Bi_2O_3 is about 2.60 eV (vs. NHE) and its conduction band is about -0.25 eV (vs. NHE), which is not theoretically usable to nitrogen reduction. Due to the oxygen vacancies in δ-Bi_2O_3, N_2 can be chemically adsorbed in the vacancies and then activated by the photogenerated electrons, which makes the δ-Bi_2O_3 based photocatalysts have excellent performance in photocatalytic N_2 reduction (Gao, Shang, et al. 2019a, 2019b).

BiO is another bismuth oxide with superior performance in photocatalytic N_2 reduction. The crystal structure of BiO from standard orientation in **Figure 2.9c** shows that it has a trigonal crystal system (a = b = 3.88 Å, c = 9.71 Å) and R3m (160) space group. BiO shows a hexagonal passage arrangement forward the (010) facet, arranged by Bi and O groups. More importantly, the size of the "tunnel" in the BiO crystal structure is around 4.5 Å and it is much larger than the diameter of N_2 molecules. Consequently, N_2 can be caged in BiO and further activated. According to DFT calculation, the VB of BiO around Fermi levels are chiefly produced by *p*-electrons of Bi (**Figure 2.9d, e**). The

charge distribution on the surface of BiO (010) can be accumulated near the Bi atoms, which means that Bi atoms can provide electrons as active centres. This is the main reason why the BiO photocatalyst exhibits excellent N_2 reduction performance (1226 μmol/g/h, which is one thousand times larger than iron-doped TiO_2) (Sun et al. 2017). Due to the lone electron pair of Bi atom, N≡N can be extended by alternatively aligned Bi atoms via devoting electrons to the flat 6d orbitals of Bi and acquiring electrons from the lone pairs of Bi atoms to the unfilled orbitals. The obtained electrons from the adjacent low-valence Bi ions can significantly decrease the N≡N energy, which can lead to a one-step 3-electron photochemical N_2 fixation process (**Figure 2.9f**).

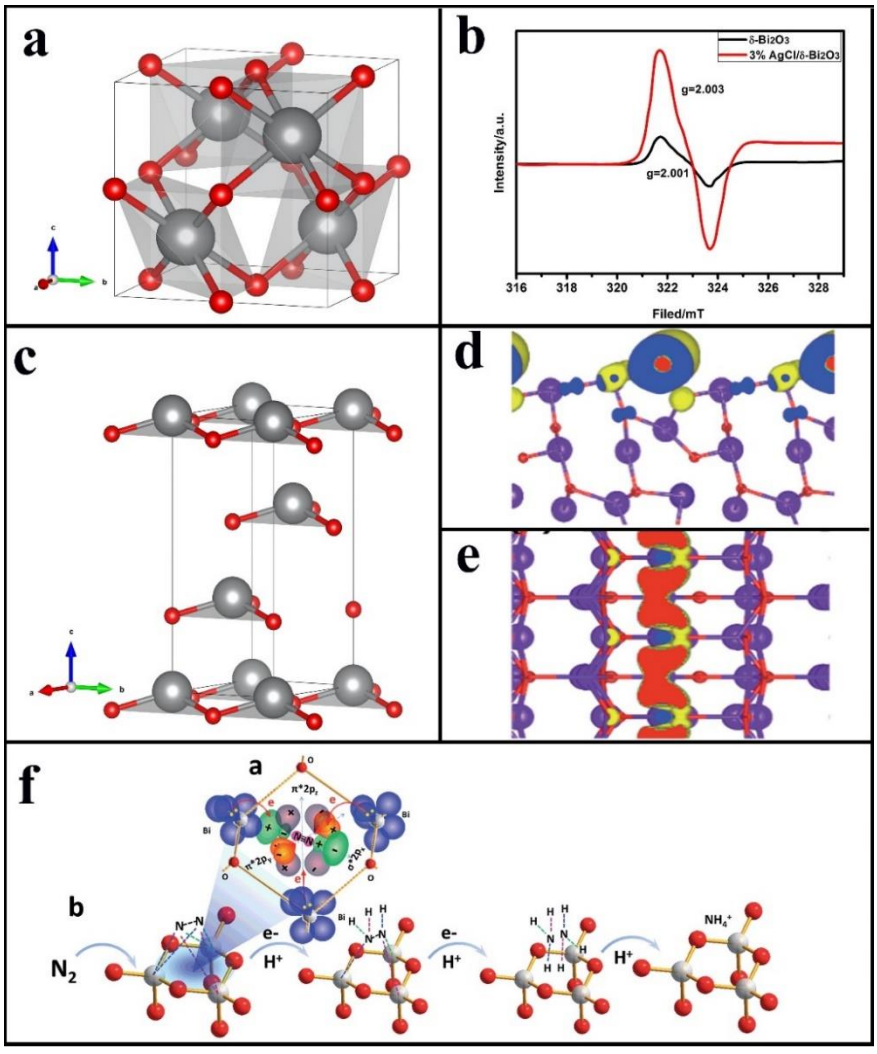

Figure 2.9 (a) The crystal structure of δ-Bi_2O_3 from standard orientation. (b) EPR spectra of δ-Bi_2O_3 and 3% AgCl/δ-Bi_2O_3. (c) The crystal structure of BiO from standard orientation. The calculated charge density at the VB of BiO (010) surfaces by (d) top view and (e) side view. (f) A probable route for the nitrogen molecule activation and the hydrogenation on the surface of the bismuth oxide catalyst. (b) Reproduced with permission (Gao, Shang, et al. 2019a). Copyright 2019, Elsevier. (d-f) Reproduced with permission (Sun et al. 2017). Copyright 2017, Royal Society of Chemistry.

2.4.3 Bismuth oxyhalides

Bismuth oxyhalides are typical ternary semiconductors belonging to the tetragonal crystal system and P4/nmm (129) space group. They generally have the formula of $[Bi_lO_mX_n]$, in which X = Cl, Br or I. The specific Bi oxyhalide structure can facilitate the formation of a layered structure comprising $[Bi_lO_m]$ and $[X_n]$ monolayers. In $[Bi_lO_m]$ layers, Bi and O are connected by covalent bonds, and van der Waals forces exist between $[Bi_lO_m]$ and $[X_n]$ (**Figure 2.10a**) (Li et al. 2017). In general, it is very difficult for N_2 molecules to be chemically adsorbed on the surface of bismuth oxyhalides because of their poor interaction between their surface and N_2 molecules (Li, Shang, et al. 2016). Recently, it has been confirmed that creating oxygen vacancies on the surface of bismuth oxyhalides is a highly efficient approach to improve the photocatalytic N_2 reduction performance (**Figure 2.10b**) (Bai et al. 2016; Di et al. 2019; Wang et al. 2017; Xue et al. 2018). For instance, BiOBr without oxygen vacancies nearly has no N_2 reduction performance, while 1 g of BiOBr with oxygen vacancies can generate 104.2 μmol ammonia in an hour under visible light irradiation (Li et al. 2015). It is attributed to the fact that oxygen vacancies can feed local electrons back to the π antibonding orbital of nitrogen molecules and adsorb them tightly (Li et al. 2015; Li, Shang, et al. 2016). Meanwhile, the firm interaction between the *p* orbitals of Bi and N can further

enhance the adsorption, which is crucial for the break of N≡N bonds and the activation of N_2 (Hao et al. 2019).

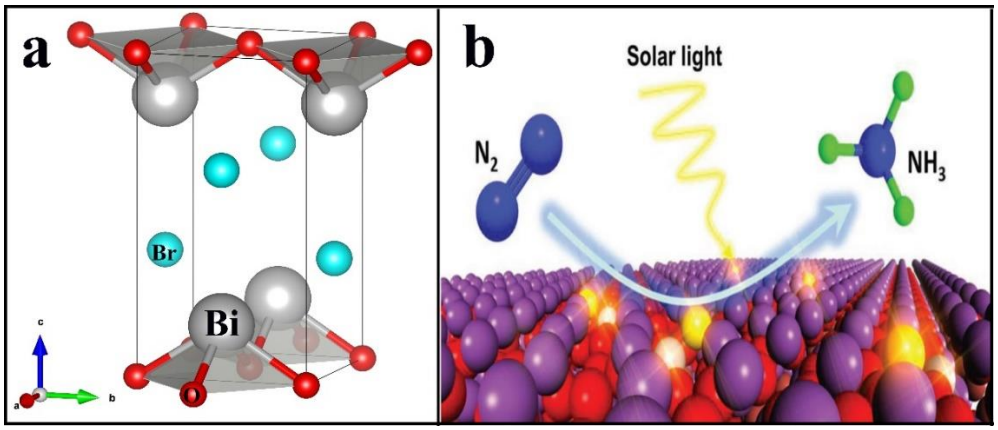

Figure 2.10 (a) The crystal structure of BiOBr from standard orientation; (b) schematic illustration of the probable photocatalytic nitrogen fixation over defect-rich Bi_3O_4Br. (b) Reproduced with permission (Di et al. 2019). Copyright 2019, Wiley-VCH.2.4.4 Bi-based polyoxometalates

The polyoxometalates comprise of at least three change metal oxyanions connected together by shared oxygen particles to shape closed 3D systems. Herein, the metal atoms might usually be Mo, W or V in their high oxidation states. Bi_2MoO_6 belongs to the monoclinic crystal system (a = 5.51 Å, b = 16.23 Å, c = 5.49 Å) and Pbca(61) space group, sandwiched by the $(Bi_2O_2)^{2+}$ between the perovskite-like MoO_6 octahedral layers (**Figure 2.11a**) (Dai et al. 2016). The CB bottom and VB top of Bi_2MoO_6 are at -0.19 and +2.29 eV, which is very close to $E(N_2/NH_3$ vs. NHE) (Li et al. 2014). Generally, it is challenging to carry out the N_2 fixation reaction on the surface of Bi_2MoO_6 as the CB is not sufficiently negative. Hao et al. stated that the coordinating unsaturated Mo atoms exposed at the edges of the Mo-O coordination polyhedron could become the active centre of the N_2 adsorption, activation and photocatalytic reduction. There are two main reasons for the excellent catalytic performance of the Bi_2MoO_6: (i)

the strong chemisorption between the N_2 and Mo active centres enables to eliminate the spatial deferral of electron transmission, and (ii) the space barriers of exciton donor centre and active centre can minimise the high overlap between the active centre and CB of Bi_2MoO_6 (Hao, Dong, et al. 2016).

Besides, bismuth vanadate is another catalyst that can be used for N_2 fixation under ambient environment. $BiVO_4$ belongs to the monoclinic crystal system (a = 5.19 Å, b = 5.09 Å, c= 11.70 Å) and I112/b (15) space group, which consists of BiO_8 and VO_4 groups. $BiVO_4$ is a layered material that is vertically separated in the *c* direction by rickety bonded oxygen planes (**Figure 2.11b**). The CB bottom and VB top of $BiVO_4$ are at +0.02 and +2.53 eV (vs. NHE), indicating that the productivity of photocatalytic generated electrons in the CB of $BiVO_4$ is too weak to reduce N_2 (Hong et al. 2011). The results show that the external electric field can reduce the energy barriers and make N_2 fixation reaction on the surface of bismuth vanadate catalysts possible (Lv et al. 2018b; Yao et al. 2018). DFT simulation indicates that the CB of $BiVO_4$ is chiefly constructed with the V 3*d* states, and the Bi 6*p* states contribute to the top (Cooper et al. 2014). Like bismuth oxyhalides and Bi_2MoO_6, N_2 molecules are challenging to be adsorbed on the prefect crystal surface of $BiVO_4$. With oxygen vacancies induced to the structure of $BiVO_4$, the V atoms with low coordination undergo spin-polarisation, which contributes to the activation and cleavage of N_2 molecules. Compared with clean $BiVO_4$, the N_2 adsorption energy on $BiVO_4$ with oxygen-vacancy reduced by 0.2 eV, indicating much stronger chemical adsorption. More importantly, the high spin-polarisation can stretch the N≡N from 1.117 to 1.143 Å, resulting in a facile split of N_2

molecules (Yao et al. 2018).

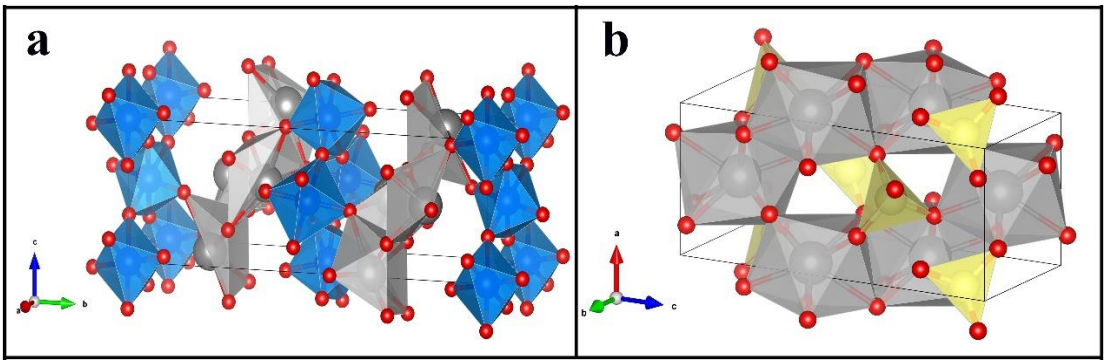

Figure 2.11 The crystal structure of a) Bi_2MoO_6 and b) $BiVO_4$.

Because of the firm interaction between the *p* orbitals of Bi and N, N_2 molecules can be firmly adsorbed on the outside surface of Bi-based photocatalysts, especially the one with oxygen vacancies. δ-Bi_2O_3 is a defective fluorite-prototype structure and its natural oxygen vacancies can aid the adsorption and activation of nitrogen. More importantly, the oxygen vacancies can lead to the accumulation of electrons on the surface of catalysts, which can feedback to N_2 and weaken the N≡N. The natural tunnel of BiO can also enhance the adsorption of N_2. Because HER requires a more negative potential than N_2 reduction, overcoming HER competitiveness is a big challenge. Notably, Bi is a less reactive metal that promotes the selectivity of N_2 activation without changing the binding energy of further intermediates. At the same time, the surface electron accessibility of HER can be prevented as it has poor hydrogen adsorption energy (Li, Tang, et al. 2019; Montoya et al. 2015). Based on the mentioned characteristics, Bi-based materials exhibit great potential in artificial ammonia synthesis under ambient condition. However, the shortages of slow transfer efficiency of electrons,

disappointing stability and positive CB position are the barriers for a new platform. Thus, effective strategies should be employed to minimise the influence of these weaknesses.

2.5 Conclusions and perspectives

The g-C_3N_4 and bismuth-based semiconductors are highly potential candidates for photocatalytic synthesis of ammonia. In recent years, g-C_3N_4-based materials have drawn huge attention for its accomplished properties, such as good stability, nontoxicity, facile and economical synthesis, wide resources and visible light absorption. For the 1D electronic confined effect, the recombination of electrons and holes can be minimized and it has broad prospects in the catalytic area. However, the synthetic approaches usually involve the template or re-crystallization, which need complex steps and are not environmentally friendly. It remains uncertain if 1D g-C_3N_4 can be produced more easily and if the problems of high energy consumption and pollution can be avoided in the production process of 1D g-C_3N_4. Bismuth-based materials have really interesting crystal properties for artificial ammonia synthesis. As global warming becomes more serious, it is imperative to use Bi-based catalysts for artificial ammonia synthesis to reduce CO_2 emission under ambient condition. Metallic bismuth, bismuth oxide, bismuth oxyhalides and Bi-based polyoxometalates all performed excellent artificial N_2-fixation activity. However, the ammonia yield is too low to meet the mass production needs. Some modification approaches such as surface oxygen-vacancy engineering, surface molecules grafting, regulation of internal electric field etc. have

great potential in solving the problems. These materials may make the mass application of photochemical synthesis of ammonia achieved, but here is still a long way to go.

Chapter 3 Chemicals and characterizations

3.1 Chemicals

In this thesis, all the chemicals were obtained from Sigma-Aldrich Australia, which are analytical reagent and used without any further purification. The chemicals includes hydriodic acid, potassium sulphate, ammonium chloride, sodium hypochlorite, sodium hydroxide, hydrochloric acid, sodium salicylate, sodium nitroferricyanide dihydrate, 4-(Dimethylamino) benzaldehyde, dicyandiamide, ethanol, methanol, bismuth nitrate pentahydrate, potassium bromide, ethylene glycol, tetrahydrofuran, sodium nitrate, ammonium chloride, tetracyanoquinodimethane, nitrogen gas, ruthenium trichloride, sodium nitrate, sodium sulfate, sulfuric acid, formic acid, dimethyl sulfoxide.

3.2 Characterizations

3.2.1 XRD

The XRD patterns of the samples were tested with a Bruker D8 Discover XRD with intense Cu *K*α radiation (40kV and 40mA, λ=1.5406 Å) at room temperature. The XRD research data were analyzed by the software Bruker Diffrac. Suite EVA V5.2 with the Crystallography open database.

3.2.2 SEM

The SEM images of the materials were carried out using a Zeiss Supra 55VP SEM, with an operating voltage of 5-15 kV. Before measurement, the samples were pasted on carbon tabs and coated with Au. The images of EDS for elemental mapping were obtained with the Oxford Ultim Max.

3.2.3 TME images

TEM image of samples was obtained from a FEI T20 Tecnai TEM or a double-corrected FEI Themis-Z 60-300 TEM equipped with ChemiSTEM EDS detector system for ultra-high count rates. The powder materials were loaded on ultrathin lacey carbon supported copper grid (TEM-LC200CUUL, 200 mesh).

3.2.4 XPS

The XPS were measure with the Thermo Fisher Scientific K-Alpha+ instrument. Samples were pasted on sample holder with carbon tape and then directly measured without treatment.

3.2.5 XRF

The XRF spectrometer (PANalytical energy-dispersive X-ray fluorescence) were used to examine the composition of obtained materials.

3.2.6 UV-vis DRS

The UV-vis diffuse reflectance spectra DRS of prepared samples were obtained from a Perkin Elmber Lambda 950 UV/VIS/NIR spectrometer, using high-purity $BaSO_4$ as the blank reference. During the measurement, about 200 mg of the sample was pressed in a self-made quartz sample holder to form a flat surface to be measured.

3.2.7 FT-IR

A FT-IR Spectroscopy (Nicolet 6700 FTIR) was used to characterize the functional moieties of prepared samples. The data were collected three times and the average results were finally used.

3.2.8 PL

PL spectra were obtained from a Shimadzu RF-6000 fluorescence spectrometer excited at 325 nm. The data interval was 0.2 nm, the scan speed was 600 nm/min, the EX bandwidth was 10.0 nm, the EM Bandwidth was 10.0 nm and the sensitivity was high.

3.2.9 PL life-time

For time-resolved PL measurement a 405-nm wavelength, 20-MHz pulsed laser was used as excitation source. The lifetimes were collected using single photon counting module (Excelitas SPCM-AQRH) and a time correlation counting module (Picoharp 300). Data was fitted with exponential function to drive the lifetime values.

3.2.10 Electrochemical characterizations

The photocurrent, EIS curves and Mott Schottky curve of the samples were obtained from an electrochemical working station (CHI-760E) in 0.1 M Na_2SO_4 solution. The counter electrode what we used was a Pt wire, and the reference electrode was an Ag/AgCl electrode. The working electrodes were prepared as follow: 7 mg of samples and 0.7 mL ethanol were mixed in 5 mL cuvettes; after that the cuvettes were sonicated for 4 h to disperse the samples in the solvent homogeneously; then the suspension was evenly coated on ITO glasses (5 × 2 cm) and dried in air for 12 h. When testing photocurrent, the light was provided by a 300 W Xenon lamp (HSX-F300, Beijing NBET Technology Co., Ltd) and no voltage was used. EIS was tested in the frequency from 0.01 to 1×10^5 Hz the initial voltage was 0.5 V and the amplitude was 0.005 V. The Mott-Schottky curves were obtained from the technology of impedance-potential, during which the voltage was from -1.5 to 1.5 V, and the frequency was 1000 Hz.

3.2.11 ESR

A Bruker EMX X-Band ESR spectrometer was used to test the ESR spectra of samples in room temperature. The solid samples were put into the ESR tubes and then directly measure.

3.2.12 Surface area

The specific surface area of samples were measured with Quantachrome instrument (Autosorb iQ2). By measuring the adsorption pressure and the amount of nitrogen adsorbed by the sample after the adsorption equilibrium of the nitrogen atmosphere, according to the BET theory, the adsorption curve in the adsorption isotherm of the sample is calculated at multiple points, and the specific surface area of the material is finally obtained.

3.2.13 Zeta potential

The zeta potential of samples were measured with Zetasizer (Nano ZS Malvern) instrument. In details, 5 mg of sample was put in 1 mL of water and put in the ultrasonic bath for 2 h. Then the suspension was directly measure. The data was collected three times and the average results were finally used.

Chapter 4 Surface defect-abundant one-dimensional graphitic carbon nitride nanorods boost photocatalytic nitrogen fixation

Related publication:

Surface defect-abundant one-dimensional graphitic carbon nitride nanorods boost photocatalytic nitrogen fixation. New Journal of Chemistry. 2020, 44, 20651-20658.

4.1 Introduction

Before 1910, it was difficult to produce ammonia on an industrial scale, and the problem was overcome since the successful development of the Haber–Bosch process (Erisman et al. 2008; Kissel 2014; Leigh 2004a). Nowadays, nitrogen fertilizers all over the world are mainly produced by the Haber–Bosch process. However, it needs iron-based catalysts, N_2, water gas (the source of hydrogen), high pressure (15–25 MPa) and high temperature (400–500 °C), which accounts 2 percent of the global energy utilization and causes 1.6% of the global CO_2 emission every year (Guo et al. 2019). Besides the application in fertilizers, ammonia is also a building block in refrigerants, pharmaceutical industries, cleaning products and other chemicals. In addition, the standard enthalpy change of combustion of ammonia is -316.8 kJ/mol, which is indeed higher than that of H_2 (-286 kJ/mol) (Council 2004; Kobayashi et al. 2019). More importantly, the complete combustion of NH_3 can only produce N_2 and H_2O, thus it is a highly potential clean fuel with high calorific value (Maffei et al. 2005; Siddiqui & Dincer 2017). Due to the high market demand and consumption of NH_3, it is critical to develop facile, clean and cost-effective ammonia synthesis methods (Liu, Li, Wu, et al.

2019; Liu, Li, et al. 2018; Meng et al. 2019).

In recent years, photocatalytic N_2 fixation provides a novel platform for artificial NH_3 synthesis under surrounding conditions (Li et al. 2015; Li 2018; Liu, Li, Zu, et al. 2019). Compared with the Haber–Bosch process, photocatalytic ammonia synthesis does not require high temperature or high pressure. It employs solar electrons to activate and cleavage the N≡N. More importantly, the hydrogen in the photocatalytic N_2-fixation process is from water, rather than water gas, which can significantly decrease the consumption of energy and the emission of carbon dioxide (Li, Shang, et al. 2016). However, the poor solubility of N_2 in water and its stable chemical structure make it challenging to achieve highly efficient photocatalytic N_2 fixation for mass production(Guo et al. 2019).

As an excellent photocatalyst, g-C_3N_4 has attracted huge interests recently (Hao et al. 2018a; Hao, Hao, et al. 2017; Wen et al. 2017). The g-C_3N_4 is a metal-free organic photocatalyst, which has a lot of advantages such as wide source, facile synthesis, low cost, good stability and visible-light response (Cao et al. 2015; Hao et al. 2018b; Hao, Niu, et al. 2016). However, g-C_3N_4 has an absorbance edge at 460 nm and it cannot absorb solar photons with the wavelength beyond this value, therefore, the light utilization of this material is not high (Bai et al. 2018; Gao, Cao, et al. 2019; Gao et al. 2018). Meanwhile, the rapid recombination of photogenerated electron-hole pairs in bulk g-C_3N_4 obstructs its catalytic performance. The g-C_3N_4 is usually prepared by the thermal calcination of its precursors, and it always shows a bulk arrangement due to the

Van der Waals forces of its layers (Bai et al. 2014). Fabrication of semiconductor materials on nanoscale with precise control in terms of size and shape provides an efficient way to regulate the transfer and separation of electron-hole pairs (Huynh, Dittmer & Alivisatos 2002; Jia et al. 2014; Peng et al. 2000). As a benchmark semiconductor material, 1D g-C_3N_4 with electron and hole pairs being confined in the width direction can efficiently transport electrons along the length direction, leading to excellent photocatalytic performance (Li et al. 2011). However, the synthesis of 1D g-C_3N_4 usually relies on complicated template approaches or complex methods which involve the peeling of bulk g-C_3N_4 to produce small components and re-assemble these components into 1D structure (Zhou, Shi, et al. 2018). Consequently, it is pressing to foster easy and harmless approaches for the arrangement of 1D g-C_3N_4.

Surface defect engineering of materials can lead to lattice distortions and excess-electron distribution, which can significantly change the properties of materials (Bai et al. 2016; Lv et al. 2018a; Wang, Shi, et al. 2019b; Xue et al. 2018). It has been recognized as one of the most powerful approaches to raise the photocatalytic nitrogen fixation activity, because electrons can be accumulated at the defects sites, which can act as the active sites for the adsorption and cleavage of nitrogen (Li et al. 2017; Xue, Chen, Yan, Zhao, et al. 2019). When the electrons are donated to N_2 molecules, the length of N≡N is increased, making it easier to break the N≡N bond.(Li et al. 2015) However, to the best of our knowledge, such facile 1D D-CN with boosted photocatalytic N_2 fixation has not been reported.

In this work, we reported an effortless synthesis of 1D defective g-C_3N_4 nanorods. The defects of the catalysts enable to activate and cleave the N_2 molecules, boosting the solar energy utilization and charge separation. Compared with the bulk g-C_3N_4, the photochemical N_2 reduction rate of defective g-C_3N_4 nanorods was increased by 3.66 times. The results of this work might provide in-depth understanding into the development of novel defective photocatalysts for N_2 fixation.

4.2 Experimental section

4.2.1 Chemicals and synthesis of materials

HI, K_2SO_4, NH_4Cl, NaClO, NaOH, HCl sodium salicylate, sodium nitroferricyanide dihydrate, 4-(Dimethylamino)benzaldehyde, dicyandiamide, ethanol and methanol are bought from Sigma-Aldrich Australia. All chemicals are analytical reagent and used without any further purification. The bulk g-C_3N_4 was prepared by the thermal decomposition of dicyandiamide. In details, 2 g of dicyandiamide was put in a 50-mL alumina crucible and covered with a lid. Then the crucible was located in a muffle furnace and heated at 550 °C for 4 h under air atmosphere. The D-CN was synthesized by modifying dicyandiamide with HI. Firstly, 2 g of dicyandiamide was put in a 250-mL beaker. After that, 25 mL of water, 25 mL of ethanol and various amount of HI (1, 1.5 and 2 mL) were added in 3 beakers. After that, the mixtures were strongly stirred for 4 h at 80 °C to make sure dicyandiamide and HI were mixed uniformly, and the majority of liquid were evaporated at the same time. Then the beakers were handed over a drying oven and heated at 120 °C for 2 h to make sure only solids were remained in the beakers. The solids were then ground in an agate mortar and the rest steps were

the same as the preparation of bulk g-C_3N_4. The obtained samples were named as D-CN-1, D-CN-1.5 and D-CN-2.

4.2.2 Characterizations

The XRD patterns of the samples were tested with a Bruker D8 Discover XRD with intense Cu *K*α radiation (40kV and 40mA, λ=1.5406 Å) at room temperature. The morphology observation on the materials were carried out using a Zeiss Supra 55VP SEM, with an operating voltage of 5 kV. TEM image of D-CN-1.5 was obtained from a FEI T20 Tecnai TEM. The XPS (Thermo Fisher Scientific K-Alpha+) and XRF spectrometer (PANalytical energy-dispersive X-ray fluorescence) were used to examine the composition of obtained materials. The UV-vis diffuse reflectance spectra DRS of prepared samples were obtained from a Perkin Elmber Lambda 950 UV/VIS/NIR spectrometer, using high-purity $BaSO_4$ as the blank reference. A FT-IR Spectroscopy (Nicolet 6700 FTIR) was used to characterize the functional moieties of prepared samples. PL spectra were obtained from a Shimadzu RF-6000 fluorescence spectrometer excited at 325 nm. For time-resolved PL measurement a 405-nm wavelength, 20-MHz pulsed laser was used as excitation source. The lifetimes were collected using single photon counting module (Excelitas SPCM-AQRH) and a time correlation counting module (Picoharp 300). Data was fitted with exponential function to drive the lifetime values. The photocurrent, EIS curves of the samples were obtained from an electrochemical working station (CHI-760E) in 0.1 M Na_2SO_4 solution. The counter electrode was a Pt wire, and the reference electrode was an Ag/AgCl electrode. The working electrodes were prepared as follow: 7 mg of samples and 0.7 mL ethanol

were mixed in 5 mL cuvettes; after that the cuvettes were sonicated for 4 h to disperse the samples in the solvent homogeneously; then the suspension was evenly coated on ITO glasses (5 × 2 cm) and dried in air for 12 h. When testing photocurrent, the light was provided by a 300 W Xenon lamp (HSX-F300, Beijing NBET Technology Co., Ltd) and its intensity was 600 mW/cm^2, and no voltage was used. EIS was tested in the frequency from 0.01 to 1 × 10^5 Hz the initial voltage was 0.5 V and the amplitude was 0.005 V. The Mott-Schottky curves were obtained from the technology of impedance-potential, during which the voltage was from -1.5 to 1.5 V, and the frequency was 1000 Hz. A Bruker EMX X-Band ESR spectrometer was used to test the ESR spectra of samples.

4.2.3 Photocatalytic nitrogen fixation performance

The photocatalytic nitrogen fixation performance was carried out with a self-made quartz reactor under simulated sunlight irradiation. During the reaction process, the light intensity was 600 mW/cm^2 and it was measured by a radiometer. Firstly, 200 mg of samples was weighted and put into the reactor. Then 95 mL of 0.1 M K_2SO_4 solution and 5 mL of methanol was added. The reactor was then closed and N_2 was bubbled in to remove air for 2 h with magnetic stirring. After that, the gas-out tube was closed and N_2 was kept bubbling in and the light was on. The photocatalytic reaction lasted 8 h and 2 mL of liquid was sampled every 2 h. The concentration of ammonium was measured by UV-VIS spectrometer by indophenol blue method at 667 nm. Firstly, the liquid was centrifugated and 1 mL of solution was sampled. Then 0.25 mL of NaOH solution (which contains 0.05 g/L NaOH and 0.1 mL/L NaClO) and 0.25 mL of sodium

salicylate (which contains 1 g/L sodium salicylate, 2 mg/L sodium nitroferricyanide dihydrate and 25 mg/L NaOH) was added. The absorbance of the solution was measured in 2 h. The calibration curve was obtained by measuring various NH_4Cl solution ($y = 1.80737x - 0.08037$, $R^2 = 0.9998$). The UV-VIS spectrometer method was also used to detect hydrazine, where the color reagent consisted with 0.5 g of 4-(Dimethylamino)benzaldehyde, 2.5 mL of HCl and 25 mL of ethanol. 2 mL color reagent and 2 mL of sample solution were mixed and the absorbance at 458 nm was recorded. The calibration curve was obtained by measuring various N_2H_4 solution ($y = 1.206x + 0.0174$, $R^2 = 0.9995$).

4.2.4 DFT calculation

In this research task, the calculations about those designs and energies depended on the standard DFT by utilizing Vienna ab initio Simulation Package (5.4.4 VASP) (Kresse & Joubert 1999). The electron trade connection work was treated through the generalized gradient approximation (GGA) with the reconsidered Perdew-Burke-Ernzerhof (RPBE) (Perdew, Burke & Ernzerhof 1996). The 450 eV energy cutoff was adopted and Brillouin zone was sampled with a 3×3×1 k-points using the Monkhorst-Pack scheme grid for geometry optimization and self-consistent calculations. A vacuum space exceeds 15 Å was employed to avoid the interaction between two periodic units. The atomic position was fully relaxed until the maximum force on each atom was less than -0.02 eV/A and 10^{-5} eV. And thermal and zero-point energy (ZPE) corrections were calculated over Γ points (Azofra et al. 2016). The van der Waals interaction has been considered using the DFT-D_3 scheme (Zhao et al. 2014).

4.3 Results and discussion

4.3.1 Component and structure

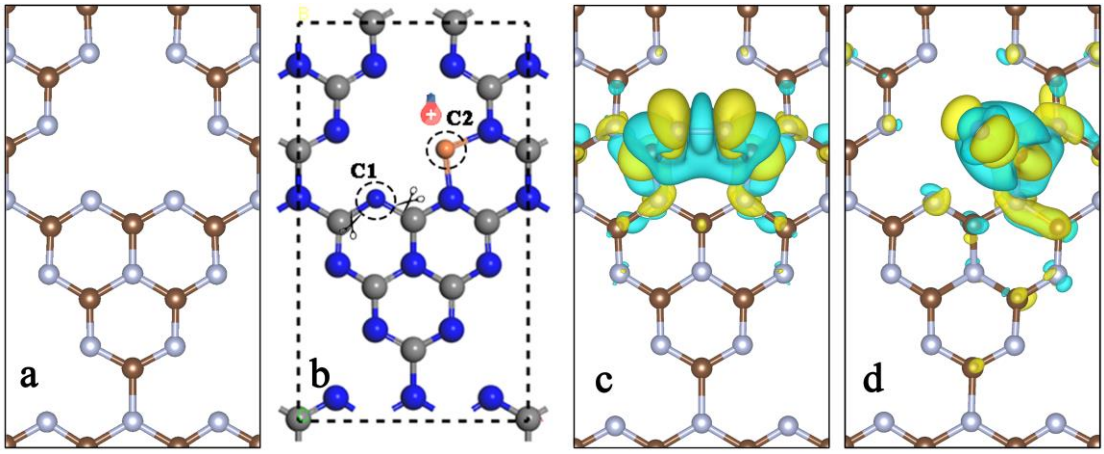

Figure 4.1 (a) Structure of g-C_3N_4; (b) Proposed structure of defect sites in g-C_3N_4; and top view of the optimized charge density difference of the N_2 adsorbed C1 (c) and C2 (d).

Figure 4.1a shows the prefect structure of g-C_3N_4, which consisted of tri-*s*-triazine rings. It is extremely difficult for N_2 molecules to be adsorbed and activated on the surface of pristine g-C_3N_4. However, when defects are induced, the condition can be totally changed. Herein, we proposed two types of defects in the tri-*s*-triazine ring structure: nitrogen vacancy (C1) or an extra carbon (C2) (**Figure 4.1b**). **Figure 4.1c** and **4.1d** are the top-view images of the optimized charge density differences of the nitrogen adsorbed on C1 (c) and C2 (d). Based on the DFT calculation simulations, the defects of g-C_3N_4 can change the charge distribution and accumulate electrons on the defect sites. It can significantly boost the adsorption and cleavage of N_2, which is regarded as the rate-determining step.

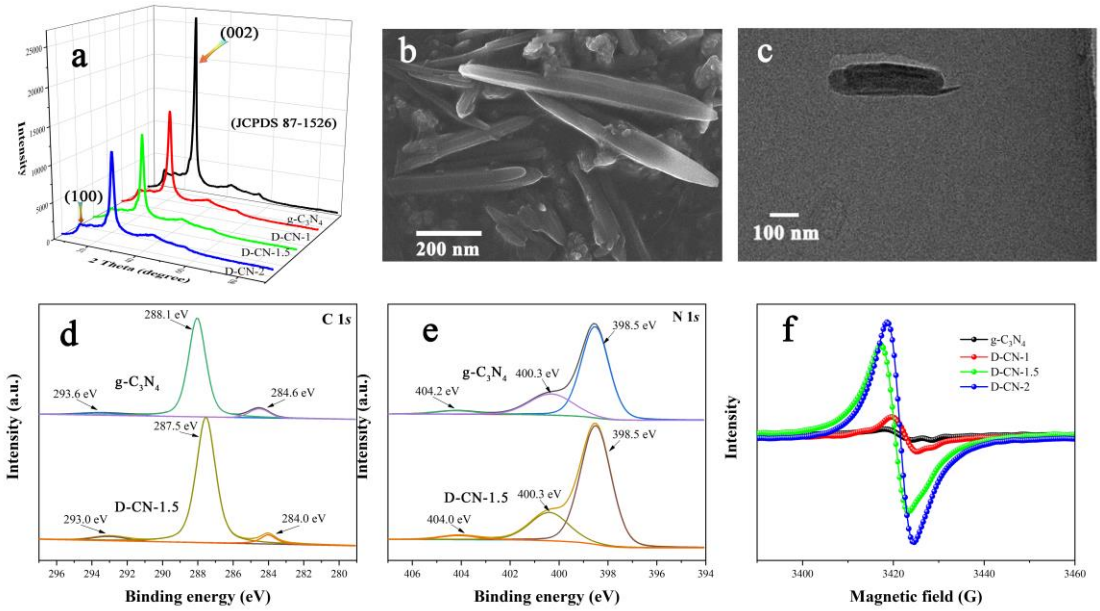

Figure 4.2 (a) The XRD patterns of as prepared samples. The SEM (b) and AFM (c) images of D-CN-1.5. The XPS narrow spectra of C 1s (d) and N 1s (e) of g-C_3N_4 and D-CN-1.5. (f) ESR spectra of as-prepared samples.

To this end, we herein developed a novel approach to prepare defective 1D g-C_3N_4 nanorods by modifying the reaction precursors using hydriodic acid (HI). 2 g precursor was treated with 1, 1.5 and 2 mL of HI and correspondingly, the obtained products were referred as D-CN-1, D-CN-1.5 and D-CN-2, respectively. **Figure 4.2a** are the XRD patterns of both the pristine g-C_3N_4 and the defective g-C_3N_4 samples. All these samples display 2 distinctive peaks at 13.1° and 27.1°, matching to the (100) and (002) crystal planes of g-C_3N_4 (JCPDS 87-1526), respectively (Hao, Hao, et al. 2017). Compared with bulk g-C_3N_4, the D-CN samples show much broaden diffraction peaks, suggesting significantly reduced size and lower crystallinity. When more HI were added to the precursor, the crystallinity of the products gradually decreased while the peak positions of the XRD patterns were fixed, which suggests the products maintain the g-C_3N_4 structure.

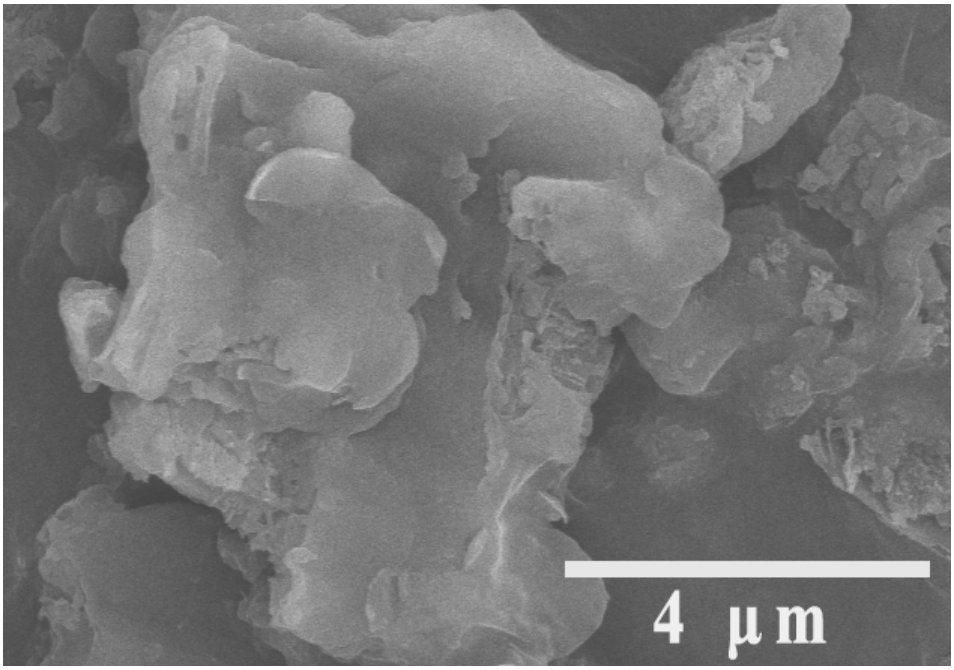

Figure 4.3 SEM image of bulk g-C_3N_4.

SEM was utilized to study the morphology of the prepared samples. From **Figure 4.3**, it can be seen that the products obtained from the direct thermal polymerization of dicyandiamide are bulk g-C_3N_4. The arrangement of bulk g-C_3N_4 with stacked-layer structure can be attributed to the Van der Waals forces of the interlayers. In comparison, D-CN-1.5 has a totally different microcosmic structure, forming elongated nanorods with around 500 nm in length **(Figure. 4.2b)**. Transmission electron microscope was employed to further study the dimensions of the D-CN-1.5 sample (**Figure 4.2c**). Compared with the bulk samples, nanorods are capable of separating charges because of their elongated nature, boosting the photocatalytic reaction rate.

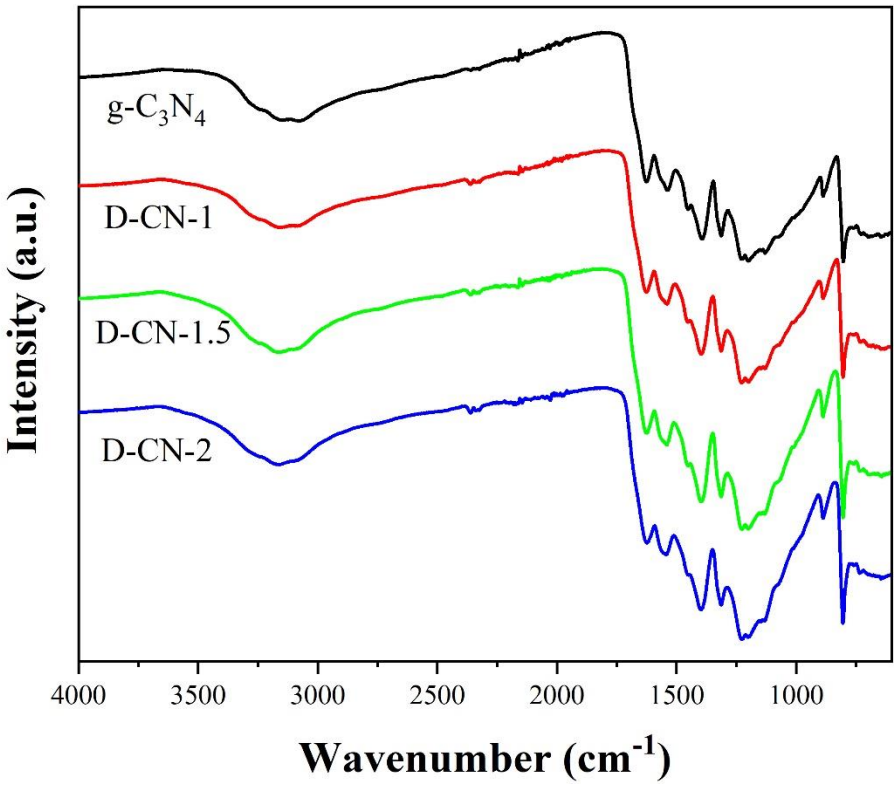

Figure 4.4 Comparison of FTIR spectra of prepared samples.

To further characterize the composition of prepared samples, FTIR spectra of the samples were conducted. As shown in **Figure 4.4**, all the samples have similar spectra, where the peaks at 1627 cm^{-1} can be accredited to the stretching vibration of C=N. The peaks at 1227, 1314 and 1395 cm^{-1} are accredited to the aromatic stretching of C–N, and the broad peaks at 3150 cm^{-1} are caused by the stretching modes of terminal NH_2 or NH groups (Yan & Yang 2011). Notably, compared with bulk g-C_3N_4, the bending vibration of triazine units of D-CN at 803 cm^{-1} showed a slight shift towards higher wavenumber (**Figure 4.5**), indicating the change of the coordination environment of N=C–N (Li et al. 2018). Both XRD and FTIR results confirm that all the samples are g-C_3N_4 and the shift of N=C–N in D-CN samples might be induced by the presence of defects.

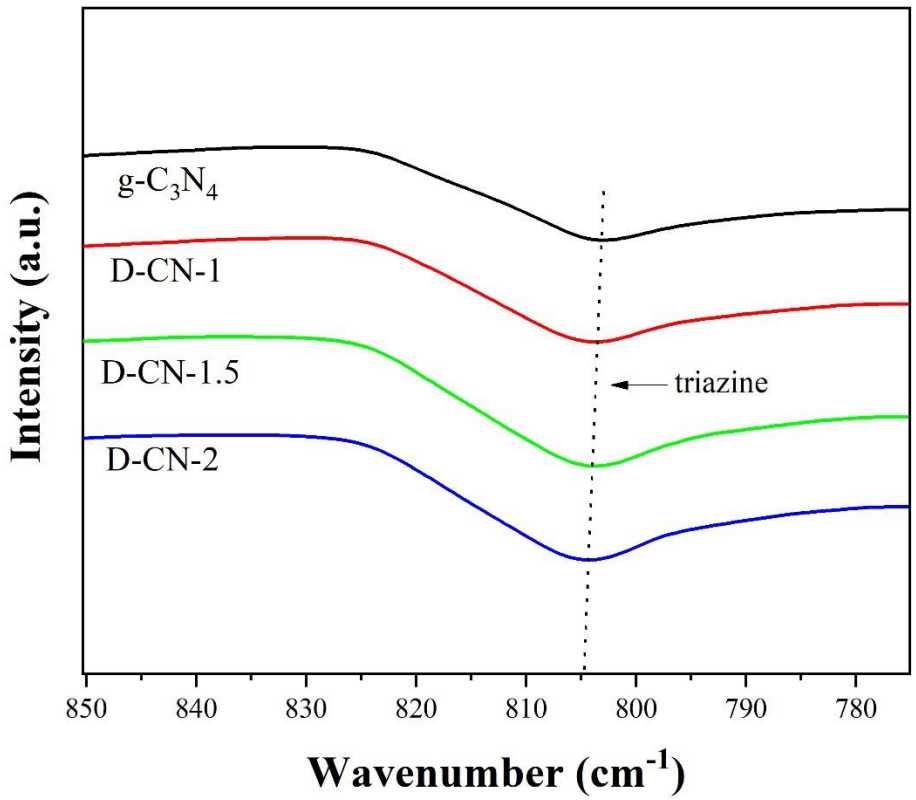

Figure 4.5 Comparison of FTIR spectra of prepared samples in a narrow range.

Then XRF and XPS characterizations were further used to confirm the composition of the samples. According to the XRF results, all the prepared samples were nearly totally composed of C_3N_4 (＞99.75%). The amount of iodine in D-CN-1, D-CN-1.5 and D-CN-2 are 0.13, 0.18 and 0.19, respectively. It indicated that almost all HI had been evaporated during the thermal decomposition process and the iodine concentration does not influence the photocatalytic activity. XPS spectra of the products confirm that the samples are mainly composed of C and N elements and no iodine species are detected (**Figure 4.6**). The XPS spectra of C 1*s* for the pristine sample (**Figure 4.2d**) show three peaks at 293.6, 288.1 and 284.6 eV, which are corresponding to the conjugated π electrons, sp^2-hybridized carbon and C–C, respectively (Hao, Hao, et al. 2017). While for D-CN-1.5, these peaks have a shift of 0.6 eV towards lower binding energy, which

is due to the shift of the coordination environment of the unsaturated C atoms caused by defects (Lu, Hao, et al. 2018). There is not much difference in the energy range around 400 eV between g-C_3N_4 and D-CN-1 (**Figure 4.2e**). The three peaks at 404.2, 400.3 and 398.5 eV correspond to the charging effect, tertiary nitrogen and sp^2-hybridized nitrogen, respectively (**Figure 4.2e**) (Bai et al. 2020).

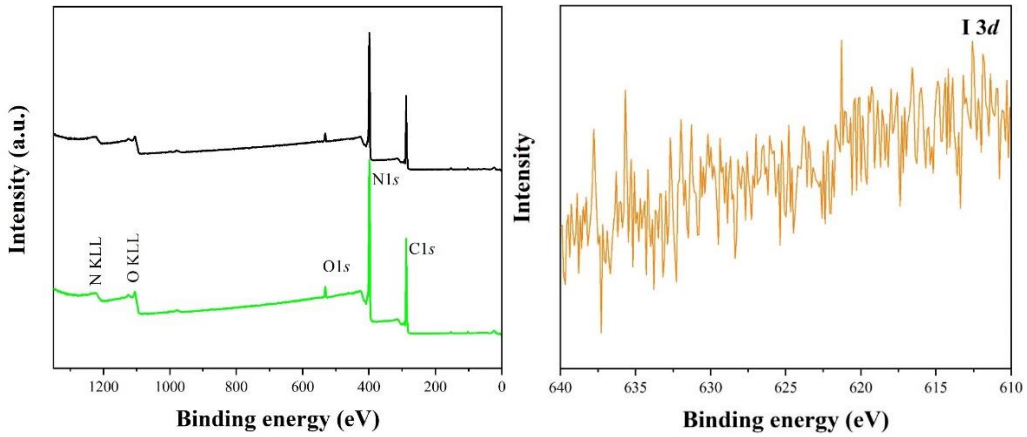

Figure 4.6 XPS survey spectra of g-C_3N_4 and D-CN-1.5, and XPS spectra of iodine in D-CN-1.5.

ESR spectroscopy was further used to characterize the defects within the samples (**Figure 4.2f**). It is extremely difficult to prepare defect-free g-C_3N_4 through the thermal decomposition process. Therefore, as expected, the ESR spectrum of bulk g-C_3N_4 shows a weak signal indicating the presence of defects, which is caused by the lone electrons of sp^2-C atoms in the π-conjugated aromatic rings. For the defective samples, the intensity of ESR signals gradually increased when more HI was added to the precursors during the synthesis, indicating that the introduction of HI can modify the arrangement of g-C_3N_4 and lead to the formation of more defects and excess electron concentration. The D-CN-1.5 showed the highest photocatalytic performance, and it is

perhaps caused by the proper amounts of defect which can change the surface charge distribution. As a result, the electrons are accumulated at the defect sites, which can contribute to the activation and cleavage of N_2 molecules. When too many defects are generated in the products, the transfer and separation of electron-hole pairs may be obstructed, causing the reduction of photocatalytic performance.(Chen et al. 2018; Wang, Mao, et al. 2019; Wang, Zhang, et al. 2019) The atomic concentration of elements from XPS was used to evaluate the defect type (**Table 4.1**). In g-C_3N_4, the C atomic is 40.54% and in D-CN-1.5 it increased to 41.87%, which can confirm the defect type is the extra carbon (C2).

Element / Sample	g-C_3N_4	D-CN-1.5
C	**40.54**	**41.87**
N	**56.72**	**55.32**
O	**2.74**	**2.81**

Table. 4.1 The atomic concentration table of g-C_3N_4 and D-CN-1.5

4.3.2 Photocatalytic activity, selectivity and stability

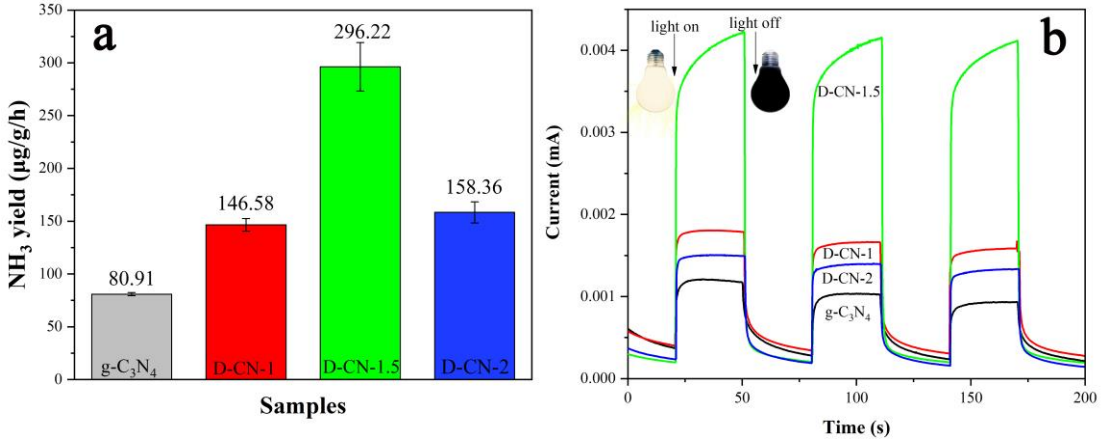

Figure 4.7 (a) Photocatalytic NH_3 yield rate of the prepared samples under simulated sunlight irradiation. (b) Photocurrent of prepared samples.

The photocatalytic reduction of nitrogen to NH_3 was employed to understand the photocatalytic performance of prepared samples. As shown in **Figure 4.7a**, the photocatalytic NH_3 yield rate of bulk g-C_3N_4 is 80.91 μg/g/h while all the defective g-C_3N_4 nanorods samples exhibit significantly higher photocatalytic N_2-fixation performance than bulk g-C_3N_4, Among all the samples, D-CN-1.5 presents the highest NH_3 yield rate of 296.22 μg/g/h, which is 3.66-fold as that of bulk g-C_3N_4. It is mainly caused by the proper amounts of defect can change the surface charge distribution. As a result of the electrons are accumulated at the defect sites, which contribute to the activation and cleavage of N_2 molecules. When too many defects are generated in the products, the transfer and separation of electron-hole pairs may be obstructed, resulting in the reduction of photocatalytic performance (Chen et al. 2018; Wang, Mao, et al. 2019; Wang, Zhang, et al. 2019).

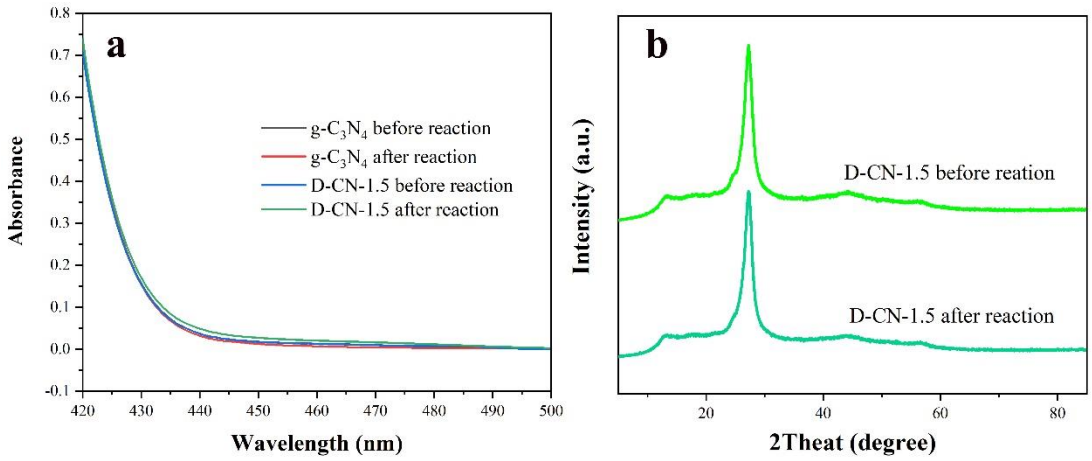

Figure 4.8 (a) UV-vis spectra of the N_2H_4 detection results, and the XRD patterns of D-CN-1.5 before and after reaction.

The NH_3 yield selectivity is also crucial for the photocatalytic N_2 reduction. Herein, the

concentration of N_2H_4 was also conducted. As shown in **Figure 4.8a**, no N_2H_4 was detected before and after the photocatalytic reaction for both g-C_3N_4 and D-CN-1.5, indicating a high NH_3 selectivity. To study the stability of D-CN-1.5, the XRD patterns of this sample before and after photocatalytic N_2 reduction were observed (**Figure 4.8b**). After long time irradiation and photocatalytic reaction, the XRD pattern of D-CN-1.5 did not show a significant decrease, which can prove that it has good stability. As g-C_3N_4 is a kind of nitrogen-based, there may be some concerns about the source of NH_3. To address this issue, we used argon (Ar) to compare the differences with N_2 (**Figure 4.9**). After 8-h light irradiation with Ar bubbled in, the NH_3 yield rates were less than 20 μg/g/h, while for the reactions with N_2, the NH_3 yield rates were significantly higher, indicating the majority of NH_3 yield are from the N_2 fixation reaction, rather than the decomposition of g-C_3N_4.

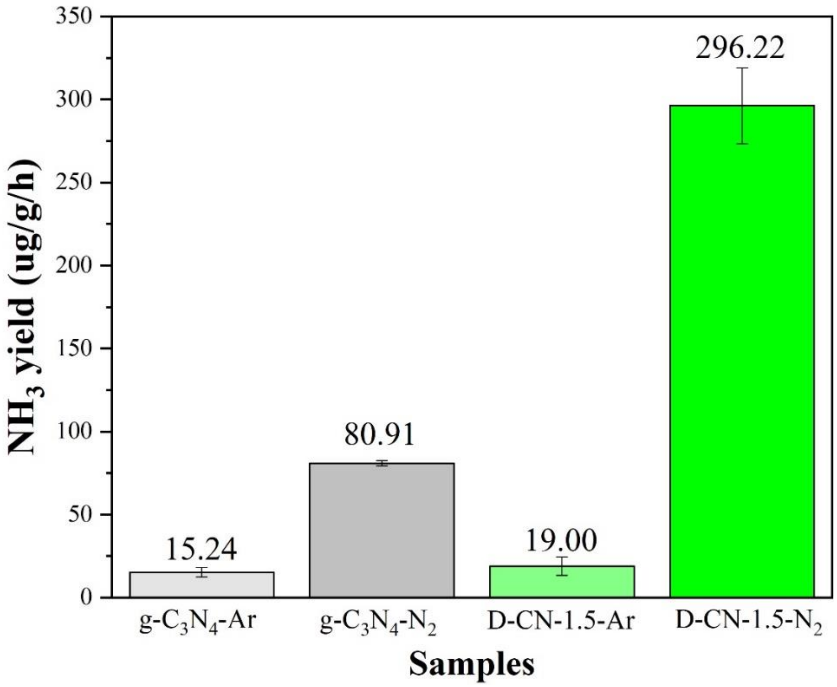

Figure 4.9 The NH_3 yield comparation of N_2 and Ar bubbled into the reaction system.

The stability is an important property for photocatalysts. **Figure 4.10a** is the SEM image of D-CN-1.5 after adsorption, which shows a clear 1D structure and it means the sample can keep stable after adsorption. Herein, we used the D-CN-1.5 in four cycles to study its stability. As shown in **Figure 4.10b**, the N_2 yield gradually decrease and the D-CN-1.5 still have 84.10% photocatalytic activity after four cycles, indicating good stability.

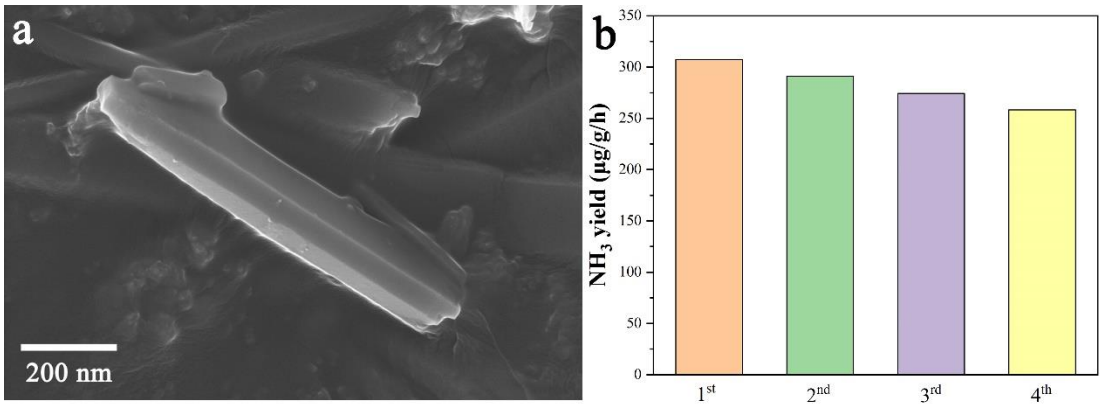

Figure 4.10 (a) The SEM image of D-CN-1.5 after adsorption. (b) Cycle stability of D-CN-1.5 in four cycles.

4.3.3 Mechanisms for the enhanced activity

Then characterizations were carried out to seek the reasons for the improved photocatalytic N_2-fixation performance by the novel surface defective 1D g-C_3N_4 nanorods. The photocurrent test is an approach to directly investigate the generation and transmission of photoinduced electrons. Shown in **Figure 4.7b**, all the samples showed significant photocurrent signals after light irradiation and the signals disappeared when the light was off. Besides, all the defective g-C_3N_4 samples have stronger photocurrent responses than bulk g-C_3N_4, hinting a stronger concentration and

faster transfer rates of electrons, which is crucial for the photocatalytic nitrogen fixation. Furthermore, EIS of the samples were tested to explore the conductivity of the prepared materials **(Figure 4.11)**. Following the same trend as photocurrent switching, D-CN-1.5 had the smallest arc radius of the EIS Nyquist plot, suggesting that D-CN-1.5 had the highest conductivity and it was beneficial to the effective transfer of photogenerated electrons.

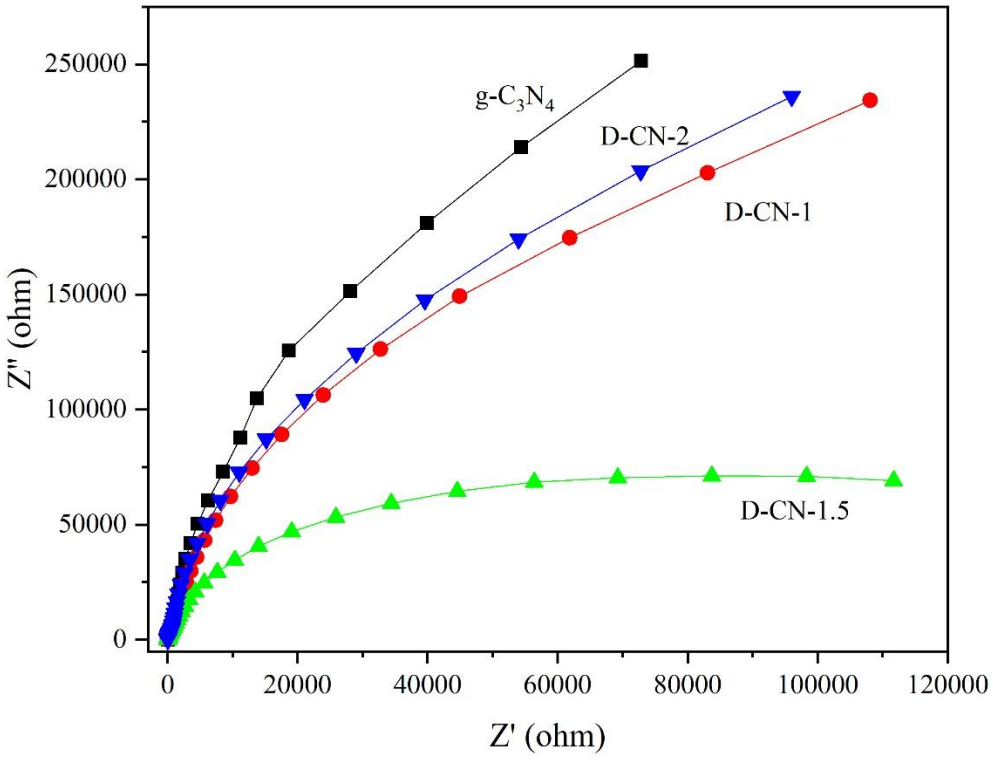

Figure 4.11 ESI of prepared samples.

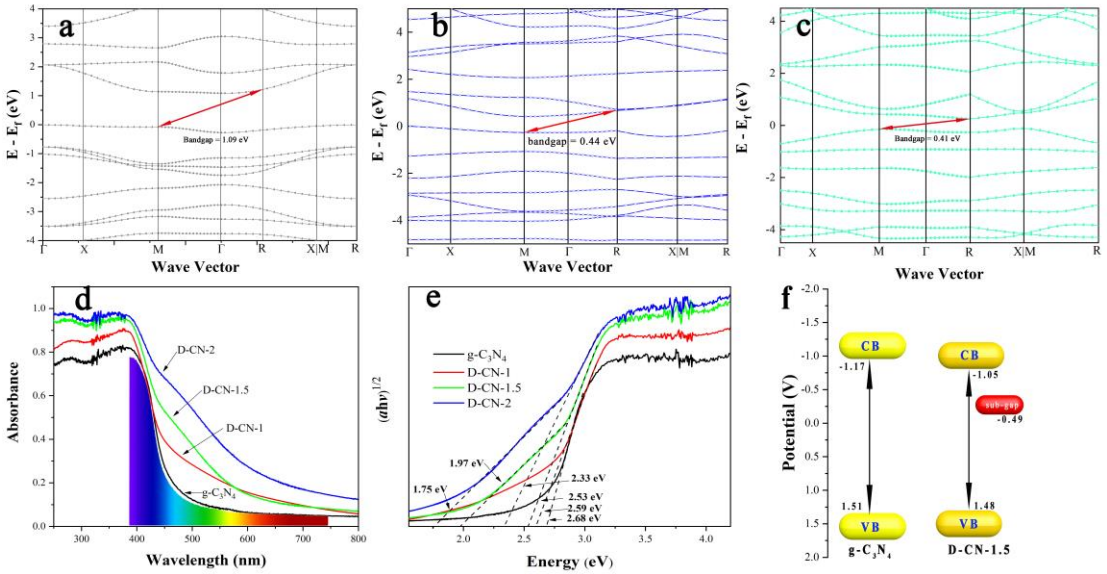

Figure 4.12 The DTF-calculated bandgap of g-C_3N_4 (a) C1 defective g-C_3N_4 (b) and C2 defective g-C_3N_4. UV-vis DRS (d) and bandgap (e) of g-C_3N_4 and defective g-C_3N_4 samples. (f) Band structure of g-C_3N_4 and D-CN-1.5.

The DTF-calculated bandgap arrangement of pristine g-C_3N_4 and two kinds of defective g-C_3N_4 are shown in **Figure 4.12a, b and c**, respectively. The pristine g-C_3N_4 gives a theoretical bandgap of about 1.08 eV (**Figure 4.12a**), which is smaller than the experimentally measured value because the DFT calculation is a ground state theory. After adding nitrogen vacancy or extra carbon in the system, the energy gaps were decreased to 0.44 (C1) and 0.41 (C2) eV, respectively. A narrow bandgap can essentially expand the sunlight-based energy usage proportion in visible light region. UV-vis DRS was applied to evaluate the light absorption of pristine and defective g-C_3N_4 samples. As shown in **Figure 4.12d**, all the samples have strong absorption in the ultraviolet range with the wavelength less than 400 nm. The absorption edge of bulk g-C_3N_4 is located at 460 nm. Compared with bulk g-C_3N_4, the absorption edges of the D-CN samples have much stronger absorption in visible light region, at the same time, the

absorption edges were largely red-shifted. Then the Kubelka-Munk formula was used to calculate the bandgaps and the sub-gaps of defective g-C_3N_4 samples (Ran et al. 2015). As shown in **Figure 4.12e**, the bandgap of g-C_3N_4 is 2.68 eV. While for D-CN-1, D-CN-1.5 and D-CN-2, the bandgap was narrowed to 2.59, 2.53 and 2.33 eV, respectively. With more defects in the samples, the light absorption got stronger. Notably, D-CN-1.5 and D-CN-2 got sub-gaps of 1.97 and 1.75 eV, respectively, being capable of absorbing solar photons in the visible range. According to ESR results, the samples have a different amount of defect. With more HI used, more defects can be generated, leading to the difference in bandgap and band structure. To further study the band structure of g-C_3N_4 and D-CN-1.5, the Mott-Schottky plots were tested (**Figure. 4.13**). According to the results, the CB positions of g-C_3N_4 and D-CN-1.5 are at -1.17 and -1.05 eV, respectively. Associated with the UV-vis DRS data, the valance band positions of these two samples are determined at 1.51 and 1.48 eV (**Figure 4.12f**). Due to the defects of D-CN-1.5, its bandgap is narrower than bulk g-C_3N_4 with a sub-gap at -0.49 eV induced by the presence of abundant defects, which can boost the absorption of visible photons.

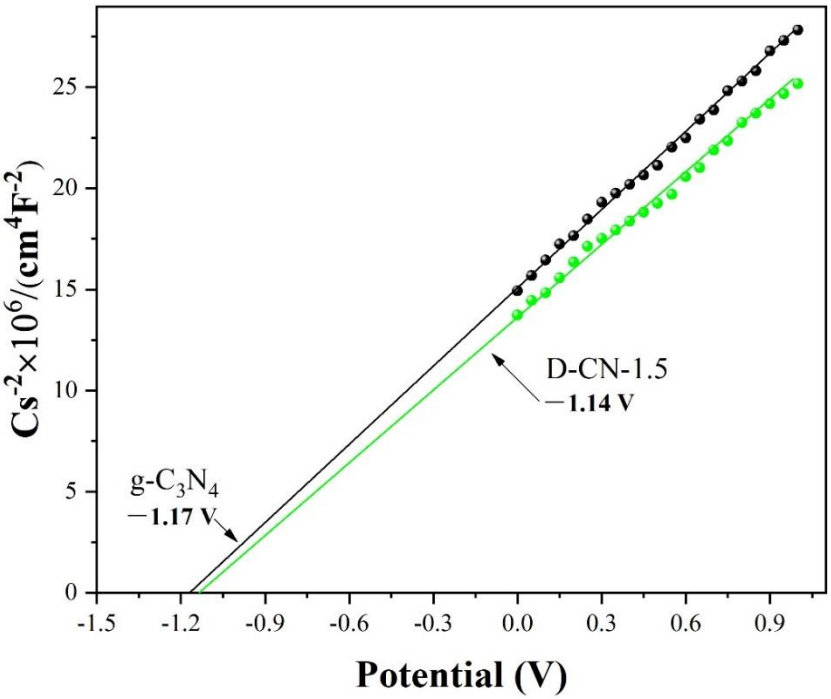

Figure 4.13 Mott-Schottky plots of g-C_3N_4 and D-CN-1.5 obtained at the frequency of 1 kHz.

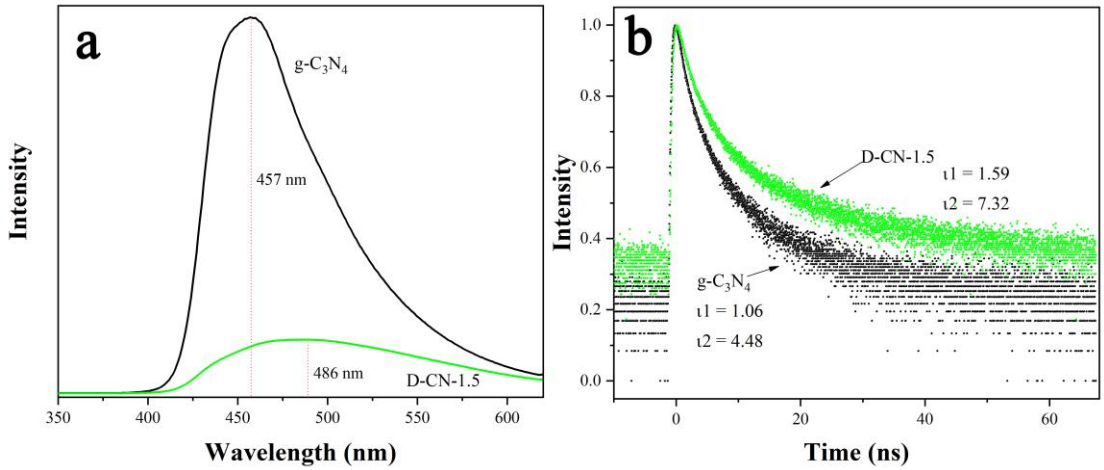

Figure 4.14 The fluorescence spectra (a) and fluorescence decay curve (b) of g-C_3N_4 and D-CN-1.5.

The PL spectra of both pristine and defective g-C_3N_4 were compared in **Figure 4.14a.** PL spectrum of pristine g-C_3N_4 shows a 457 nm-centred broad emission with profiles slightly deviating from a perfect Guanine curve because a subtle increase of PL intensity is observed in the longer wavelengths in the range of 500 nm to 600 nm. In the case of D-CN-1.5, the emission consisted of two types of transitions including a

band edge transition and the transition to the sub-band being below the bottom of the CB of g-C_3N_4, which is consistent with the band structure depicted in **Figure 4.12f.** The emission intensity is indeed lower than that of pristine g-C_3N_4, indicating the recombination of electrons and holes in D-CN-1.5 were significantly restrained. The PL peak of D-CN-1.5 shifted to 486 nm due to the emission from the trap states produced by surface defects. The study of the PL lifetime of the obtained samples enables us to reveal the photophysical dynamics associated with the recombination of electron-hole pairs. Generally, a PL longer lifetime of a certain material correlates to a higher efficiency of charge separation, and it is beneficial to the boosted photocatalytic performance. The PL lifetimes of g-C_3N_4 and D-CN-1.5 were obtained from time-resolved transient PL spectroscopy (**Figure. 4.14b**). Both PL lifetime curves displayed a two-exponential decay. The short/long PL lifetimes for g-C_3N_4 and D-CN-1.5 are 1.06/4.48 ns and 1.59/7.32ns, respectively. It is evident that longer PL lifetimes are observed in D-CN-1.5 which is in consistence with the abundant defects in this sample.

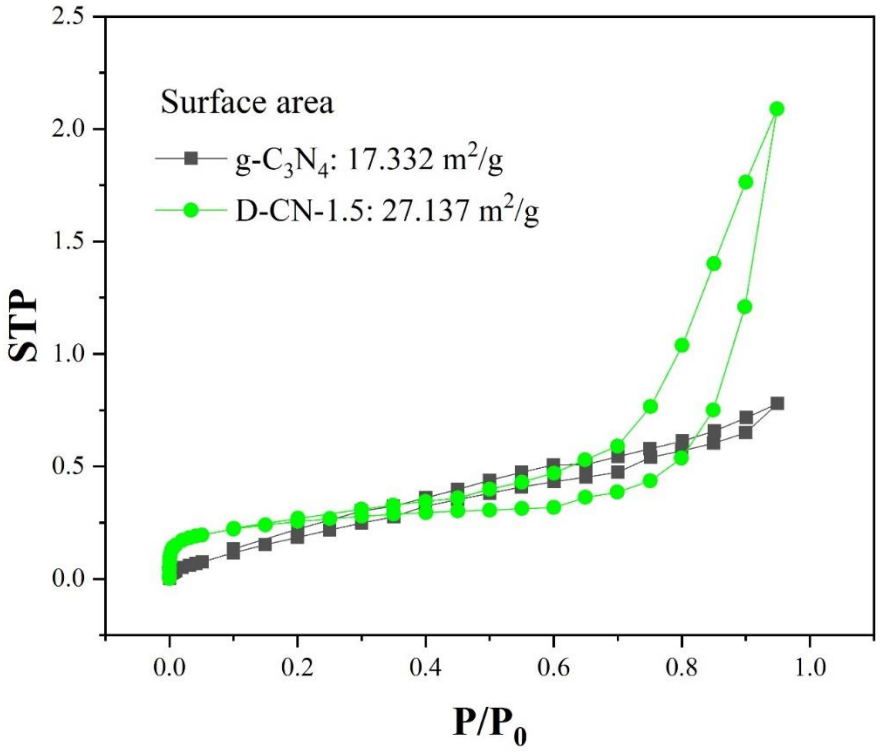

Figure 4.15 N_2 adsorption-desorption isotherm of g-C_3N_4 and D-CN-1.5

BET surface area was then carried out to study the surface area of g-C_3N_4 and D-CN-1.5 (**Figure. 4.15**). The surface of bulk g-C_3N_4 is 17.332 m^2/g, and it is 63.87% as that of D-CN-1.5 (27.137 m^2/g). The increased surface is able to increase the contact between the catalyst and N_2 molecules and it is helpful for the enhanced photocatalytic nitrogen fixation performance.

To further elucidate the NRR mechanism of g-C_3N_4, in particular to reveal how the presence of abundant surface defects can improve their catalytic activity on nitrogen-fixation defective g-C_3N_4, DFT calculation was used to estimate the catalytic site, free energy and chem-adsorption of each elementary step. And the calculations were performed to study the structure-activity relationship in the defective g-C_3N_4 system. In the C1, the dinitrogen was adsorbed on the two neighbor carbon atoms of nitrogen

vacancy, and the free energy profile was shown in **Figure 4.17**. The results indicated that nitrogen molecules indeed would be well captured by the two carbon atoms, because the adsorbed and first hydrogenation steps are exothermic reactions. The real challenge comes from the following hydrogenation steps, and the rate-determining steps are the second and third hydrogenation steps in the distal (0.72 eV) and alternating (0.75 eV), respectively. And in the C2, elementary steps associated with distal, alternating and enzymatic possible pathways of the sample are shown in **Figure 4.16a**. The enzymatic route was excluded, due to the massive input energy (2.86 eV). In the other possible ways, the dinitrogen adsorbed on the extra carbon atom, and the *p* orbit of nitrogen atom was occupied by the carbon atom. Furthermore, the N≡N length was enhanced from 1.10 Å in the free individual nitrogen molecules to 1.18 Å in this condition, indicating that N_2 is activated even the reaction needs input 0.68 eV to complete it. More steps are exothermic in the following reactions, except the step of NH_2* to NH_3 and the last NH_3 desorption (0.41 eV). But all the input values are lower than the first steps, therefore, the nitrogen adsorption step is the rate-determining reaction and the energy barrier is 0.68 eV in the defective g-C_3N_4. Lastly, the HER, competing reaction, was analyzed in **Figure 4.16a** and **Figure 4.17**. The results indicated that the samples had worse HER performance, and the values are -2.06 and -2.16 eV on the C1 and C2, respectively.

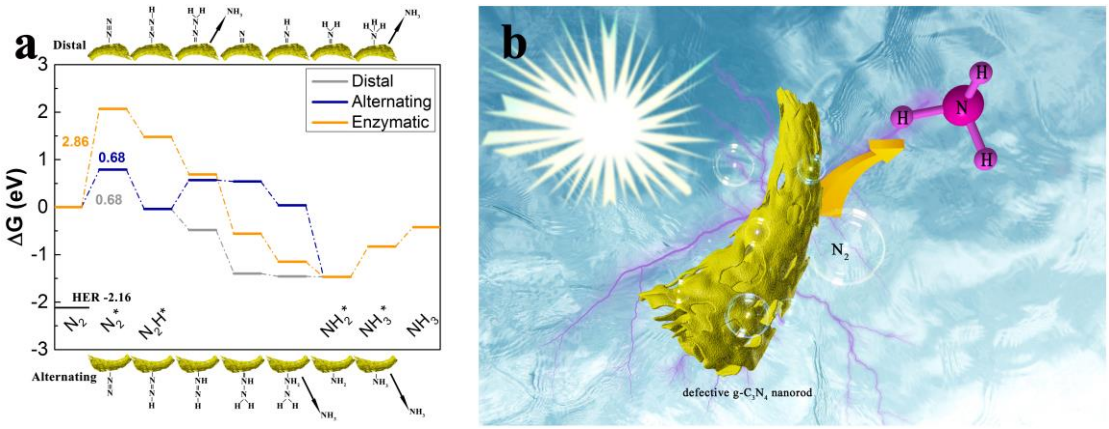

Figure 4.16 (a) Gibbs free energy of the nitrogen reduction reaction on the surface of defective C2. (b) Proposed reaction mechanism on the surface of defective g-C_3N_4 nanorods.

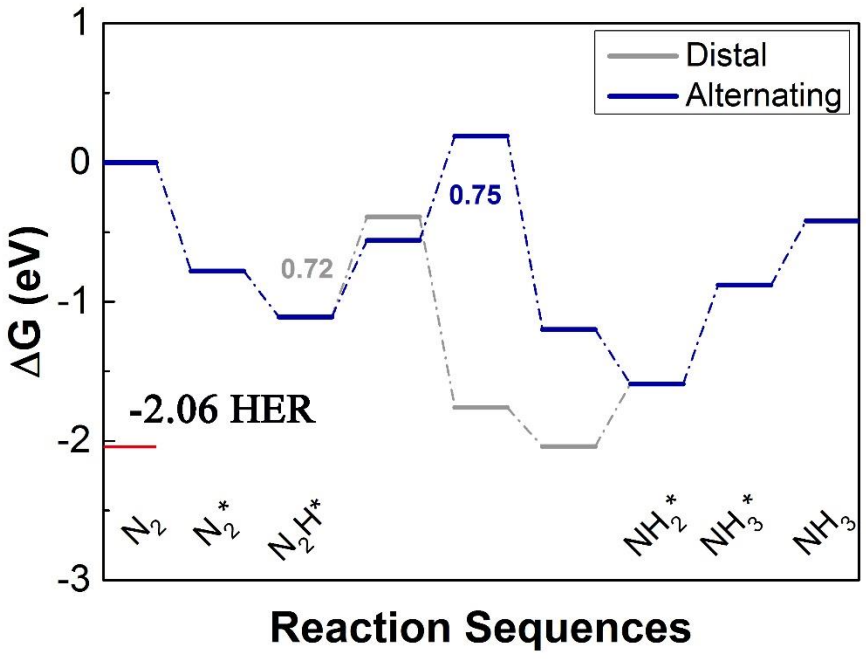

Figure 4.17 Gibbs free energy of the N_2-fixation process of C1.

To summarize, we employed a facile synthetic approach to prepare defective g-C_3N_4 nanorods by using HI-treated precursors. The obtained nanorods were about 500 nm. With more HI added, more defects were created on the outside surface of g-C_3N_4 nanorods. When the amount of used HI was 1.5 mL, the obtained sample showed the

highest photocatalytic NRR activity, which was 3.66-fold as that of bulk g-C_3N_4. Depend on the comprehensive characterizations and DFT calculations, several aspects of the novel defective 1D g-C_3N_4 nanorods were revealed to be capable of enhancing the photocatalytic NRR activity:

(1) The defects can change the surface charge distribution of the catalysts, making electrons accumulated at the active sites, which is helpful to the adsorption of nitrogen.

(2) According to the DFT results, the extra carbons are regarded as the most possible active centres. The N≡N length of the N_2 molecules adsorbed on the active sites can be stretched from 1.10 Å to 1.18 Å. As a result, the cleavage of N_2 became easier, and it is the rate-determining step.

(3) With defects induced to the g-C_3N_4 nanorods, the bandgap and band structure showed consequentially change. Not only the bandgap was narrowed, but also a sub-gap was generated, which could significantly increase the solar energy utilization efficiency.

(4) Due to the 1D confinement effect, the transfer of electrons can be rapidly increased, resulting in a higher photocurrent, longer lifetime and enhanced photocatalytic NRR activity.

As such we proposed a potential mechanism for the involved reactions and the enhanced photocatalytic activity by the defective g-C_3N_4 nanorods (**Figure 4.16b**).

Under solar light irradiation, electrons of defective g-C_3N_4 nanorods are excited and captured at the defect sites on the surfaces. The N_2 molecules are strongly adsorbed at the defect sites and activated by the accumulated electrons. Then the hydrogenation reaction will gradually take place and then NH_3 is produced.

4.4 Conclusion

In this work, we reported a novel preparation of 1D defective g-C_3N_4 nanorods by the facial treatment of precursors. The defects of the catalysts can help to adsorb, activate and cleave the N_2 molecules. Besides, the bandgap was narrowed, leading to higher utilization of solar energy and faster separation of charge carriers. The formed 1D structure can also boost the transfer and separation of electron-hole pairs. In contrast with bulk g-C_3N_4, the photocatalytic N_2 reduction rate of defective g-C_3N_4 nanorods was increased by 3.66 times. The results and finding of this work can provide in-depth visions into the development of novel defective photocatalysts for N_2 fixation.

Chapter 5 Small molecule π-conjugated electron acceptor for highly enhanced photocatalytic nitrogen reduction of BiOBr

Related publication:

Small molecule π-conjugated electron acceptor for highly enhanced photocatalytic nitrogen reduction of BiOBr. (Accepted by Journal of Materials Science & Technology)

5.1 Introduction

NH_3 is a kind of the most crucial industrial ingredients, which has been extensively used in the agricultural, pharmaceutical and chemical industry (Giddey, Badwal & Kulkarni 2013; Lassaletta et al. 2014). The production of NH_3 fertilizers makes it possible for us to provide sustainable agriculture to support the 7 billion population (Erisman et al. 2008). However, the NH_3 is fundamentally generated through the Haber-Bosch process, which enables to convert N_2 and H_2 to NH_3 under high temperature and high pressure (Leigh 2004a). Thus, the Haber-Bosch process is not environmentally friendly, which consumes 2 percent of the global energy and it is able to cause about 1.6% CO_2 emission (Guo et al. 2019). Therefore, it is essential to develop cost-effective, green approaches to synthesize NH_3 under ambient conditions.

In chapter 4, we developed a novel synthesis of 1D defective g-C_3N_4 nanorods by the facial treatment of precursors. The defects of the catalysts can help to adsorb, activate and cleave the nitrogen molecules, resulting in the increased N_2 fixation performance. Besides defect engineering, using electron withdrawing organic molecules to modify semiconductors should be an easier approach with high efficiency, as it is easier to be

controlled than defects. However, research on withdrawing organic molecules modified photocatalysts to enhance photochemical N_2 fixation performance has never been reported.

In recent years, photochemical synthesis of NH_3 has grown into a hot research frontier (Liu, Wang, et al. 2019; Zhang, Zhao, et al. 2019). It utilizes photogenerated electrons to activate and cleavage nitrogen molecules. At the same time, the protons from water can take part in the reaction to form NH_3. Hence, the approach is environmentally friendly and has broad prospect for mass production. While the photochemical synthesis of NH_3 is still limited in laboratory study, because of the poor ammonia yield rate. The main reasons include the low solubility of nitrogen in water, the poor adsorption of N_2 on catalysts as well as the firm bond of N≡N (Tang & Qiao 2019).

Recently, Bi-based materials have shown extensive prospect in artificial N_2 fixation, because of the advantages of the proper bandgap for visible light response, unique layer structure and facile preparation (Li et al. 2017; Li, Tang, et al. 2019; Sim et al. 2020). More importantly, Bi is a less HER active element, which can significantly obstruct the HER (Wang, Shi, et al. 2019b). Since HER is a competing reaction for N_2 reduction, the obstructed HER will benefit the N_2 fixation significantly. Among the family of Bi-based materials, BiOBr composed with $[Bi_2O_2]$ units is regarded as a highly prospective photocatalyst for photocatalytic nitrogen fixation (Chen, Zhang, et al. 2021; Lan et al. 2021; Xue, Chen, Yan, Hu, et al. 2019). The conduction band of BiOBr is occupied by Bi 6p state in the main, and its valence band is occupied by Br 4p state with hybridization with O 2p and Bi 6s orbitals (Huang 2009). The highly dispersive band structure of BiOBr with a low reciprocal effective mass of photoinduced electrons endow electrons and holes to transfer rapidly (Kong et al. 2016). It has already been

confirmed that the natural oxygen vacancies contribute to the successfully photocatalytic N_2 fixation by BiOBr (Li et al. 2015). The BiOBr has the advantages of facile preparation and visible light response. However, the absorption edge of BiOBr is about 430 nm and its visible light utilization is also low (Heidari, Haghighi & Shabani 2020; Shi et al. 2020; Yu et al. 2020). In addition, its photocatalytic activity is not high. Strategies should be invented to enhance the photocatalytic N_2 fixation performance of BiOBr to achieve possible industrial application.

Defect engineering is thought as a highly efficient way to boost the artificial N_2 fixation activity (Di et al. 2019). The defect sites are usually recognized as active sites for photocatalytic nitrogen reduction. The reason is that the defect sites can make N_2 molecules strongly chemisorbed. At the same time, the accumulate electrons at defect sites are fed to the antibonding π^* orbitals of nitrogen molecules, lending to the expansion and weakness of N≡N. As a result, the activation and cleavage of N_2 molecules became much easier (Shi et al. 2019). If the electron concentration on the surface of photocatalysts can be increased, the photocatalytic N_2 fixation activity will also be significantly boosted.

TCNQ is a kind of conjugated organic compound that has been recognized as a unique electron accepter (Bennett et al. 2020). TCNQ can form organic charge-transfer salts, which are of interest in the optical properties, electronic properties and magnetic conductivity (Ni et al. 2020). It has been widely reported that the combination of TCNQ with other photocatalysts can significantly boost light absorption, conductivity and photocatalytic activity (Hayat et al. 2019; Hu et al. 2017; Jiang et al. 2014; Zhang et al. 2016). However, to the best of our knowledge, using π-conjugated electron accepter TCNQ to modify semiconductors to achieve highly efficient photocatalytic N_2 fixation

is never reported.

In this chapter, a facile self-assembly process was employed to get BiOBr-TNCQ composite photocatalysts. Compared with BiOBr, the photocatalytic activity of the optimum sample on N_2 fixation under simulated sunlight irradiation increased 5.49 times. The introduction of TCNQ to BiOBr enables to significantly increase the solar energy absorption, conductivity, and separation of electron-hole pairs. More importantly, the remarkable electron-withdrawing property of TCNQ can accumulate electrons on the surface of catalysts, making the adsorption and activation of nitrogen molecules much easier. Correspondingly, the photochemical N_2 fixation performance was greatly boosted. The results of this work may give some vision to the development of self-assembly and high-performance photocatalysts.

5.2 Experimental section

5.2.1 Preparation of BiOBr nanosheets

BiOBr spheres consisted of nanosheets were prepared by a facile solvothermal reaction (**Figure 1a**). 7.5 mmol of $Bi(NO_3)_3 \cdot 5H_2O$ and 7.5 mmol of KBr was added to 80 mL of ethylene glycol. After that, the mixture was stirred for 2 h and then pureed into a 100-mL polytetrafluoroethylene autoclave. The autoclave was put in a drying oven and reacted at 160 °C for 12 h. When the temperature decreased to 25 °C, the solid in the autoclave was collected and washed by ethanol 5 times. Finally, the obtained samples were dried at 60 °C in air and BiOBr spheres were successfully obtained.

5.2.2 Self-assembly of BiOBr and TCNQ

As shown in **Figure 1a**, BiOBr microspheres (1 g) consisted of nanosheets and a certain amount of TCNQ (0.05, 0.15 and 0.20 g) was added to 100 mL of THF solution. The

beaker was covered with parafilm and the suspension was magnetically stirred for 2 h. After that, the parafilm was removed and the magnetic stir was still on to make THF evaporated. Finally, the THF could be fully evaporated and uniform TCNQ modified BiOBr microspheres were obtained. The prepared samples were named as BiOBr-TCNQ-1, BiOBr-TCNQ-2 and BiOBr-TCNQ-3, respectively. Due to the opposite electrical properties of BiOBr and TCNQ, the electrostatic self-assembly can be achieved (-40.93 mV of TCNQ and +3.38 mV of BiOBr).

5.2.3 Characterization

The XRD patterns of the samples were tested with a Bruker D8 Discover XRD with intense Cu *K*α radiation (40 kV and 40 mA, λ = 1.5406 Å) at room temperature. The morphology observation on the materials was carried out using a Zeiss Supra 55VP SEM, with an operating voltage of 5-15 kV. The images of EDS for elemental mapping were obtained with the Oxford Ultim Max. The XPS was tested with Thermo Fisher Scientific K-Alpha+. The UV-vis diffuse reflectance spectra (DRS) of prepared samples were obtained from a Perkin Elmber Lambda 950 UV/VIS/NIR spectrometer, using high-purity $BaSO_4$ as the blank reference. A FT-IR Spectroscopy (Nicolet 6700 FTIR) was used to characterize the functional moieties of prepared samples. PL spectra were obtained from a Shimadzu RF-6000 fluorescence spectrometer excited at 325 nm. The photocurrent and EIS of the samples were obtained from an electrochemical working station (CHI-760E) in 0.1 M Na_2SO_4 solution. The counter electrode was a Pt wire, and the reference electrode was an Ag/AgCl electrode. The working electrodes were prepared as follow: 7 mg of samples and 0.7 mL ethanol were mixed in 5 mL cuvettes; after that, the cuvettes were sonicated for 4 h to disperse the samples in the solvent homogeneously; then the suspension was evenly coated on ITO glasses (5 × 2 cm) and dried in air for 12 h. When testing photocurrent, the light was provided by a

300 W Xenon lamp (HSX-F300, Beijing NBET Technology Co., Ltd) and its intensity was 600 mW/cm^2, and no voltage was used. EIS was tested in the frequency from 0.01 to 1×10^5 Hz the initial voltage was 0.5 V and the amplitude was 0.005 V. A Bruker EMX X-Band ESR spectrometer was used to test the ESR spectra of samples.

5.2.4 Photocatalytic nitrogen fixation

Herein, a self-established system was used to study the photocatalytic N_2 reduction performance. Firstly, 20 mg of prepared samples and 100 mL of distilled water were added to the quartz reactor. Then the reactor was put on the magnetic stir and high-purity nitrogen was continuously bubbled in for 2 h to remove other gases in the system. After that, the gas outage side of the reactor was closed and N_2 was kept bubbling at the speed of 10 mL/min. At the same time, the solar simulator (300 W Xenon lamp HSX-F300 produced by Beijing NBET Technology Co., Ltd)) was turned on and the photocatalytic reaction started. The photocatalytic N_2 fixation reaction lasted 8 h and 2 mL of solution was sampled in each 2 h. The concentration of NH_3 was measured by Nessler's reagent colourimetry. In details, 2 mL of sample solution was mixed with 0.1 mL of potassium sodium tartrate solution (ρ = 500 g/L) and 0.1 mL of Nessler's reagent. After 20 min, the absorbance of the solution was recorded at 420 nm. The UV-vis spectrometer method was also used to detect hydrazine. The color reagent was the mixture of 0.5 g of 4-(Dimethylamino)benzaldehyde, 2.5 mL of HCl and 25 mL of ethanol. Two milliliter of color reagent and 2 mL of sample were mixed and the absorbance was measured at 458 nm. To further confirm the source of NH_3-N, the 1H-NMR spectra were measured (Bruker 400 MHz). Firstly, 0.5 mL of sample solution, 0.1 mL of DMSO-d6 and 10 μL of 1M H_2SO_4 were mixed. Then the solution was immediately tested by the NMR.

5.3 Results and discussion

5.3.1 Structure and morphology

Firstly, the SEM was used to study the morphology of the prepared samples. BiOBr had a sphere structure consisted of nanosheets. The diameter of the spheres was about 1 μm (**Figures 5.1b, e**). In contrast, the morphology of BiOBi-TCNQ is quite different from BiOBr. As shown in **Figure 5.1d**, in BiOBi-TCNQ-2, TCNQ was coated on the BiOBr spheres uniformly, forming a core-shell structure. **Figures 5.1 g-k** are the energy dispersive spectra for elemental mapping of Bi, Br, O, C and N in BiOBi-TCNQ-2, which can further confirm the components of BiOBi-TCNQ samples. According to the HRTEM results, the main exposed crystal plane of BiOBr is the (001) plane (**Figure 5.1f**).

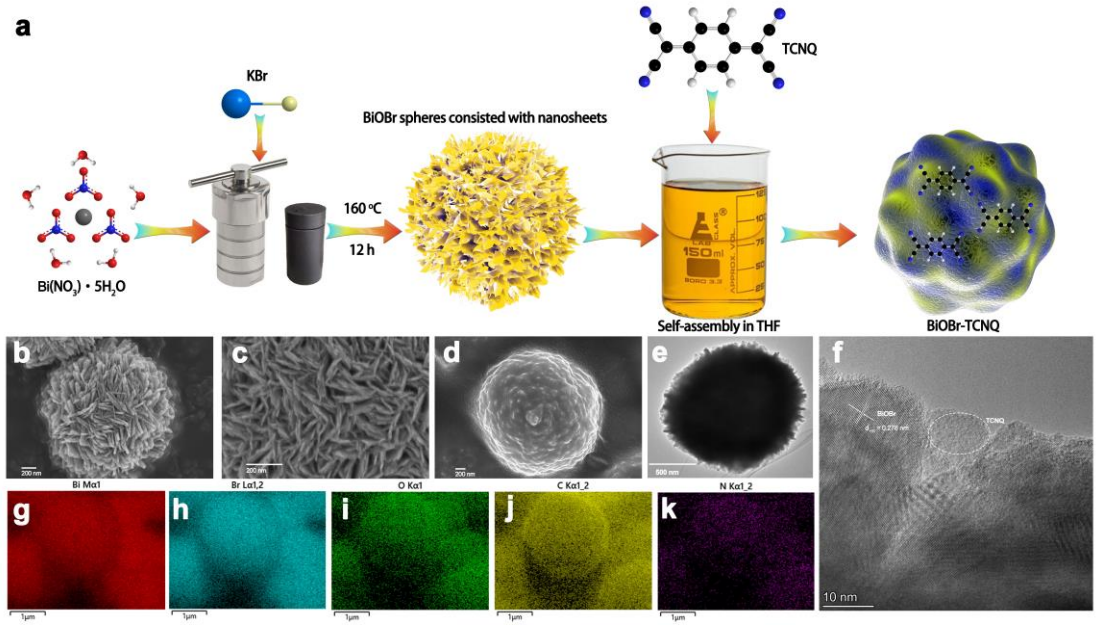

Figure 5.1 (a) Schematic illustration of the preparation of BiOBr nanosheets and the self-assembly process with TCNQ. (b), (c) The SEM images of BiOBr. (d) The SEM image of BiOBr-TCNQ-2. (e) The TEM image of BiOBr sphere. (f) The high-resolution TEM image of BiOBr-TCNQ-2 and the energy dispersive spectra for elemental mapping of Bi (G), Br (h), O (i), C (j) and N (k).

Figure 5.2a shows the XRD patterns of synthesized samples. The diffraction peaks of BiOBr fitted well with the standard card JCPDS 73-2061, indicating BiOBr was successfully prepared (Xia et al. 2016). The BiOBr-TCNQ samples showed the same diffraction peaks as BiOBr, because TCNQ is a kind of amorphous organic molecules and it does not have diffraction peaks. Then we used FTIR to further study the components of prepared samples. As shown in **Figure 5.2b,** TCNQ had 4 obvious peaks between the wavenumber of 2300 to 500 cm^{-1}. The peak at 2221 cm^{-1} is the typical stretching of C≡N. The peak at 1539 cm^{-1} is attributed to the stretching vibration of C=C. The peak at 1349 cm^{-1} can be assigned to the in-plane bending vibration peak of C–H bonds, and the peak at 857 cm^{-1} is the out-plane bending vibration of C–H bonds (Bhadu et al. 2018). In the FTIR spectrum of BiOBr, the two peaks at 507 and 770 cm^{-1} are contributed to the Bi–O of BiOBr. The peak around 1600 cm^{-1} is attributed to the adsorbed water (Gupta et al. 2017; Tu et al. 2012). In the spectra of BiOBr-TCNQ samples, both the characteristic peaks of BiOBr and TCNQ appeared, indicating the BiOBr-TCNQ samples were successfully fabricated. Notably, the peak of C–H bonds and Bi–O bonds showed a slight shift towards a higher wavenumber (**Figure 5.3**), which is probably caused by the interaction between BiOBr and TCNQ. After that, X-ray photoelectron spectrum was used to further study the components of the samples. **Figure 5.2c** showed the narrow O 1*s* spectra of BiOBr and BiOBr-TCNQ-2. BiOBr had 3 peaks at 533.6, 531.9 and 530.6 eV, which were attributed to the adsorbed water, adsorbed oxygen and the lattice oxygen of BiOBr (Yan et al. 2020; Yu et al. 2017). In contrast, the new peak that appeared at 532.8 eV was the formation of C–O bonds between BiOBr and TCNQ. As for the peaks of Bi 4*f*, two peaks in the spectrum of BiOBr appeared at 165.3 and 160.0 eV, and they were assigned to Bi $4f_{7/2}$ and Bi $4f_{5/2}$. While in BiOBr-TCNQ-2, the peaks shifted to 165.1 and 159.8, which were caused by

the strong interaction between BiOBr and TCNQ (**Figure 5.2d**). Based on the SEM, HRTEM, XRD, FTIR and XPS results, it can be concluded that BiOBr-TCNQ samples were successfully fabricated.

Then, EPR spectra were utilized to analyze the characteristic of unpaired electrons of the prepared samples. As shown in **Figure 5.2e**, the pristine BiOBr had a weak EPR signal, which was caused by its oxygen defects. During the solvothermal synthesis of BiOBr, it is really difficult to get a prefect crystal and there are always some oxygen defects. When TCNQ was added, the BiOBr-TCNQ samples got a much stronger EPR signal in the spectra, which were caused by the delocalized π electrons of TCNQ (**Figure 5.2f**). The stronger electron concentration on TCNQ can boost the adsorption and cleavage of N_2 molecules, leading to significantly enhanced photocatalytic activity. Depend on the characterizations, a possible structure of BiOBr-TCNQ was proposed (Inserted image of Figure 2f). Along the (001) plane, TCNQ was bridged with the oxygen atom of BiOBr via the C–O bonds.

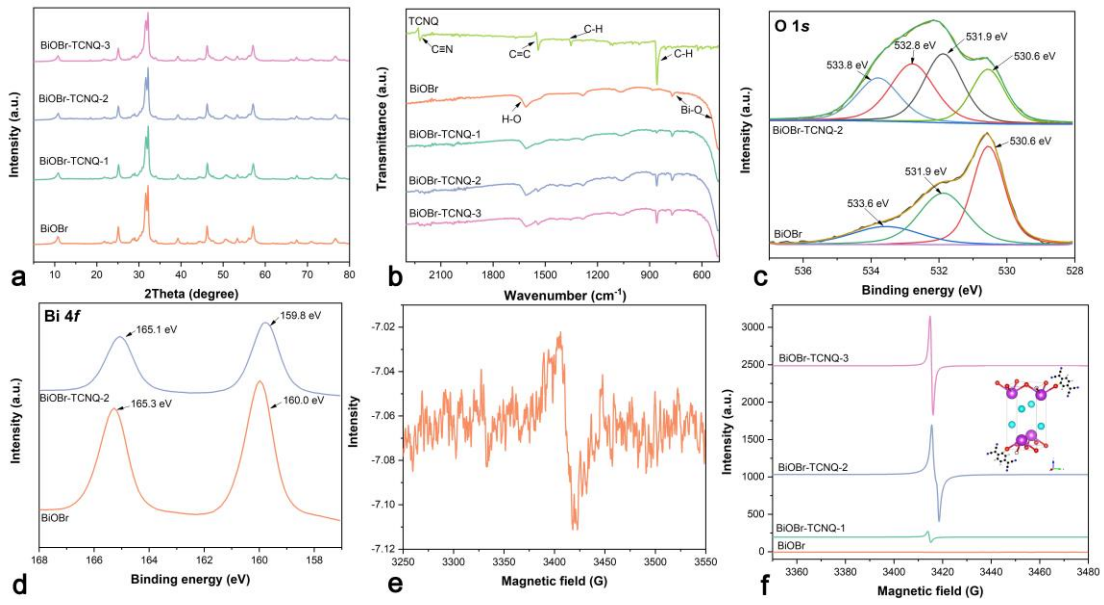

Figure 5.2 (a) The XRD patterns of BiOBr and BiOBr-TCNQ samples in the range of 5 to 80 degrees. (b) The FTIR spectra of BiOBr and BiOBr-TCNQ between 2300 to 500 cm^{-1}. The narrow XPS spectra of O1*s* (c) and Bi 4*f* (d). The EPR spectra of BiOBr (e) and BiOBr-TCNQ samples (f).

Inserted image in Figure 2f: The proposed possible structure of BiOBi-TCNQ sample.

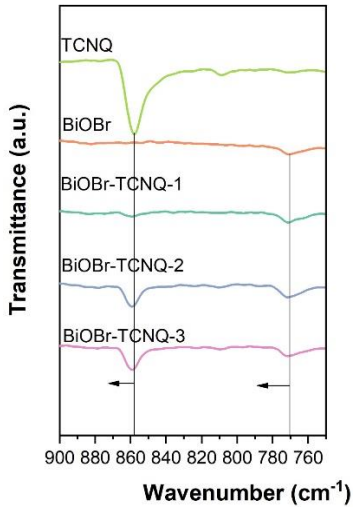

Figure 5.3 The zoom-in part of FTIR spectra of prepared samples.

5.3.2 Photocatalytic nitrogen fixation activity

Herein, we used simulated solar light irradiation to study the photocatalytic nitrogen fixation activity of prepared photocatalysts. During the light irradiation, the NH_3 concentration gradually increased over time (**Figure 5.4a**). After 8-h simulated sunlight irradiation, the NH_3 concentration in the reactor of BiOBr reached 0.76 mg/L. All the BiOBr-TCNQ samples showed higher photocatalytic nitrogen fixation performance than BiOBr. The NH_3 yield was calculated and shown in **Figure 5.4b**, where BiOBr-TCNQ-2 had the highest NH_3 yield of 2.617 mg/h/g_{cat} which was 5.49 time as that of pristine BiOBr. The remarkable photocatalytic N_2 fixation activity of BiOBr-TCNQ is higher than most reported BiOBr-based photocatalysts (**Table 5.1**). When too much TCNQ was added, the photocatalytic activity decreased, which was probably due to TCNQ can obstruct the light absorption of BiOBr, leading to the decrease of photogenerated electron amount and the decrease of photocatalytic activity.

Table 5.1 The comparison among the reported BiOBr-based photocatalysts for N_2 fixation and the

results of this work

Photocatalysts	Light range	NH_3 yield	Ref
BiOBr with oxygen vacancy	Visible light	104.2 μmol/h/g	(Li et al. 2015)
Bi/BiOBr	Visible light	15.9 μmol/h/g	(Huang et al. 2021)
Fe/BiOBr	Visible light	46.1 μmol/h/g	(Chen, Zhang, et al. 2021)
H-Bi@ BiOBr	Visible light	181.2 μmol/h/g	(Hua et al. 2019)
H-BiOBr	Simulated solar light	About 100 μmol/h/g	(Bi et al. 2018)
Bi2MoO6/BiOBr	Simulated solar light	90.7μmol/h/g	(Xue, Chen, Yan, Hu, et al. 2019)
Bi@BiOBr–Bi_2MoO_6	Simulated solar light	167.2 μmol/h/g	(Lan et al. 2021)
BiOBr-TCNQ	Simulated solar light	186.93 μmol/h/g	This work

Then isotope labelling experiment with $^{15}N_2$ gas was carried out to confirm the yield NH_3 came from the cleavage and fixation N_2 gas, rather than other trace pollutants from the air. **Figure 5.4c** showed the NMR spectra of $^{15}NH_4Cl$ standard solution and the final photoreduction production of $^{15}N_2$ by BiOBi-TCNQ-2. They both showed two peaks with a coupling constant of 73.14 Hz. The $^{15}NH_3$ concentration of the solution after the photocatalytic N_2 reduction of BiOBi-TCNQ-2 was calculated to be 4.19 mg/L, which matched the results obtained by UV-vis spectrophotometry. Besides, the selectivity is good as no hydrazine is detected (**Figure 5.5**). The NMR results can confirm that the formation of NH_3 is attributed to the photocatalytic reduction of N_2 gas. Cycle stability is an important property for photocatalysts. Herein, we ran the photocatalytic N_2

reduction reaction of BiOBi-TCNQ-2 four times to evaluate its stability (**Figure 5.4d**). After 4-time usage, the NH_3 yield was 2.140 mg/h/g_{cat}, which was 81.8% as the fresh sample, indicating good stability for reuse.

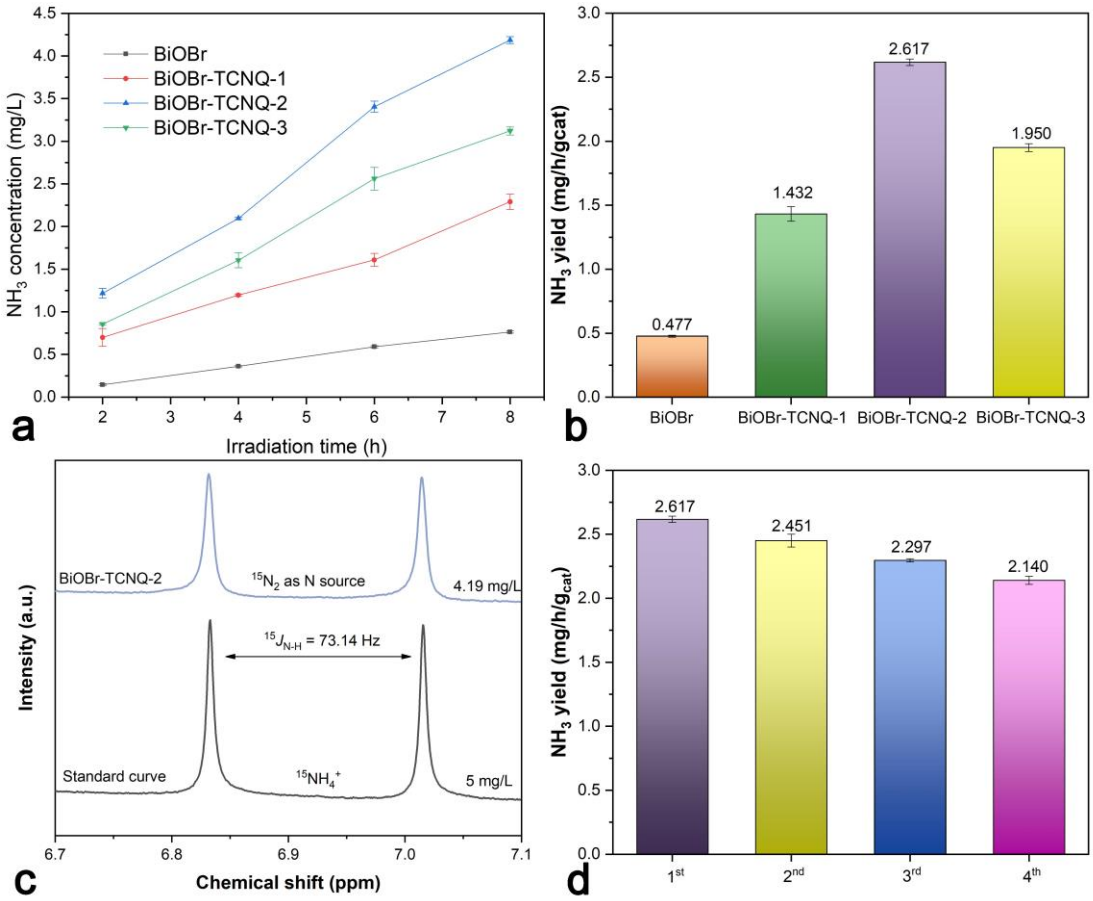

Figure 5.4 (a) The ammonia concentration changes over time. (b) The NH_3 yield by prepared samples. (c) The NMR spectra of $^{15}NH_4Cl$ standard solution and the final photoreduction production of $15N_2$ by BiOBi-TCNQ-2. (d) The NH_3 yield of BiOBi-TCNQ-2 in cycle uses.

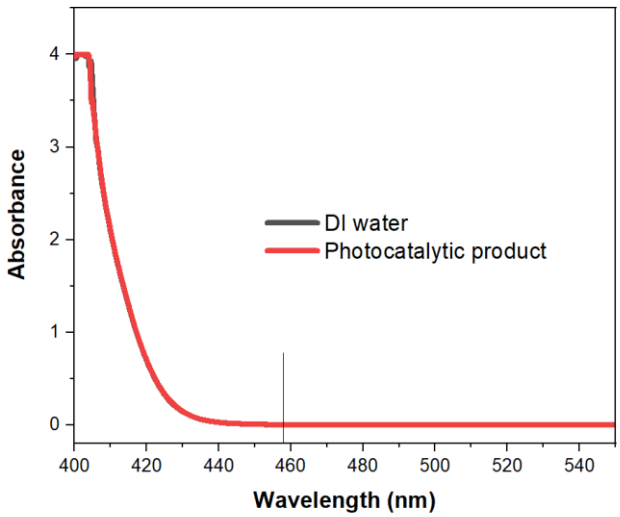

Figure 5.5 The UV-vis spectra of the solution to detect hydrazine with color reagent.

5.3.3 Mechanisms of the enhanced photocatalytic N_2 reduction

Herein, a series of characterizations about optical and electrochemical properties were carried out to reveal the mechanisms for the significantly increased photocatalytic N_2 fixation performances. Firstly, UV-vis DRS were measured to study the light absorption property of BiOBr, TCNQ and BiOBr-TCNQ samples. As shown in **Figure 5.6a**, BiOBr had an absorbance edge at 429 nm, indicating a bandgap of 2.9 eV. With TCNQ coated on the surface of BiOBr spheres, the BiOBr-TCNQ samples got higher solar energy absorption in the visible-light range. The more TCNQ added, the higher light absorption the composite samples got. Notably, a new peak appeared at 573 nm, which can be identified as the charge transfer absorption peaks (Jiang et al. 2014). The generation of the new charge-transfer absorption peak can boost the light absorption and enhance the photocatalytic activity. **Figure 5.6b** was the PL spectra of BiOBr and BiOBr-TCNQ-2. The PL spectra intensity of BiOBr-TCNQ-2 was much lower than that of BiOBr, indicating a lower recombination speed of photogenerated electron-hole pairs, which is beneficial to the enhanced photocatalytic activity. The photocurrent is a

direct technique to reflect the concentration of photogenerated electrons. As displayed in **Figure 5.6c**, the average photocurrent of BiOBr was only 0.8 μA. However, the average photocurrent of BiOBr-TCNQ-2 was about 32 μA, and it was 40-fold as that of pristine BiOBr. Since TCNQ is an excellent electron acceptor, it can accumulate photogenerated electrons as well as boost the separation of electron-hole pairs. As a result, the photocurrent was significantly increased and the BiOBr-TCNQ-2 showed the remarkable photocatalytic N_2 fixation activity. The conductivity is also important for the migration of photogenerated charge carriers. Herein, EIS was used to compare the conductivity of BiOBr and BiOBr-TCNQ-2. As shown in **Figure 5.6d**, the arc radius of the EIS Nyquist plot of BiOBr-TCNQ-2 is much smaller than that of pristine BiOBr. The EIS results illustrated the inclusion of TCNQ can increase the conductivity and accelerate the separation of photogenerated charge carriers.

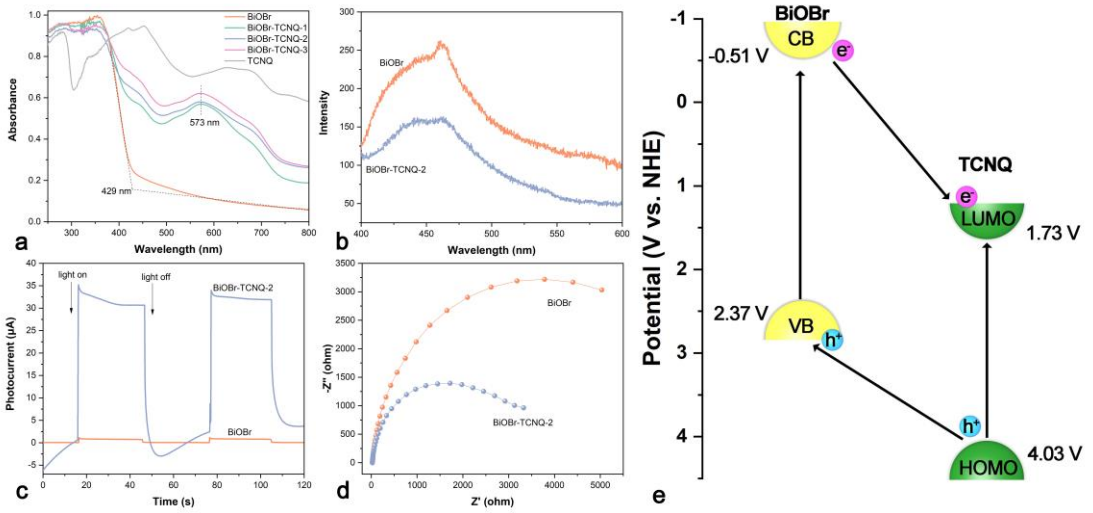

Figure 5.6 (a) The UV-vis DRS spectra of BiOBr, TCNQ and BiOBr-TCNQ samples. (b) The photoluminescence spectra, (c) photocurrent response and (d) electrochemical impedance spectroscopy of BiOBr and BiOBr-TCNQ-2. (e) The mechanisms of the separation and transfer of photogenerated electron-hole pairs for the remarkable photocatalytic N_2 fixation performance.

Based on these experimental results, a scheme was proposed to clarify the mechanisms of the separation and transfer of photogenerated electron-hole pairs for the remarkable photocatalytic N_2 fixation performance of BiOBr-TCNQ-2 (**Figure 5.6e**). The bandgap

of BiOBr is about 2.9 eV and the HOMO–LUMO gap of TCNQ is about 2.3 eV. The valance band and conduction band of BiOBr are at 2.37 and -0.51 V (vs. NHE) (Huang et al. 2015). The HOMO and LOMO orbital of TCNQ are at 4.03 and 1.73 V (vs. NHE) (Jiang et al. 2014). Under simulated solar light irradiation, electrons on the valance band of BiOBr and the HOMO orbital can be excited, leaving holes on the valance band and HOMO orbital. The holes can transfer from the HOMO orbital to the valance band of BiOBr. Electrons can be accumulated on the LUMO orbital of TCNQ because of its positive LUMO position and the unique electron-withdrawing property. Based on the well-match band structure, delocalized π electrons of TCNQ and the electron-withdrawing property of TCNQ, the separation and transfer of photoinduced electron-hole pairs in the BiOBr-TCNQ-2 sample were significantly accelerated. The accumulated electrons can strengthen the adsorption of N_2 molecules on the surface of catalysts, boosting the cleavage of N≡N bonds. As a result, the photocatalytic N_2 reduction to ammonia efficiency increased 5.6 times. We noted that BiOBr-TCNQ-3 showed lower photocatalytic N_2 fixation activity than BiOBr-TCNQ-2, that is because too much TCNQ can block the light absorption and excitation of BiOBr.

5.4 Conclusion

In this chapter, a novel BiOBr-TCNQ photocatalyst was prepared via a facile self-assembly method. Due to the well-match band structure of TCNQ and BiOBr, the separation and transfer of photogenerated electron-hole pairs were significantly boosted. More importantly, the abundant delocalized π electrons of TCNQ, and the strong electron-withdrawing property of TNCQ made electrons efficiently accumulated on the surface of catalysts, leading to a remarkable photocatalytic activity. Compared with the pristine BiOBr, the optimized BiOBr-TCNQ sample showed a 5.6-fold photocatalytic

N_2 reduction activity. This work might open a new avenue for optimizing the electronic structure of photocatalysts to achieve highly efficient photochemical reductions.

Chapter 6. A green synthesis of Ru modified g-C_3N_4 nanosheets for enhanced photocatalytic ammonia synthesis

Related publication:

A green synthesis of Ru modified g-C_3N_4 nanosheets for enhanced photocatalytic ammonia synthesis. Energy Materials Advances. 2021, 2021, 9761263.

6.1 Introduction

NO_3^- is a necessary nutrient for plants, whereas high-level of NO_3^- enter the food chain via water sources can be toxic and hazardous to the ecosystem (Santamaria 2006; Swann 1975; Yue et al. 2019). The main culprits of NO_3^- pollution includes agricultural runoff, fertilizer abuse, septic systems, industrial plants and irrigation systems (Wick, Heumesser & Schmid 2012). Currently, NO_3^- contamination has been a serious environmental concern as it can affect the quality of groundwater and surface water, causing health problems to humans (He et al. 2019; Kumar et al. 2020). In an oxygen-deficient environment, for example, in the digestive systems, NO_3^- can be converted to more toxic NO_2^- (Lidder & Webb 2013; Lundberg, Weitzberg & Gladwin 2008). Nitrite is able to transform low-ferritin into methemoglobin in people's body, resulting in the loss of oxygen transportation. It can likewise respond with optional amine mixtures to deliver cancer-causing nitrosamines (Motevalli et al. 2019). Thus it is urgent to develop a novel strategy to remove NO_3^- pollution with high efficiency and selectivity.

NH_3 is an important industrial ingredient widely used in fertilizers, pharmaceutical industries and other areas (Kobayashi et al. 2019; Tong et al. 2020). More importantly,

it is also an essential energy source. The decomposition of ammonia is a low-cost and facile process, therefore, using NH_3 as a H_2 carrier is able to solve the H_2 storage problem to a certain extent (Wang et al. 2013; Zhao et al. 2019). With the increase of the global population, the demand for NH_3 keeps increasing. Currently, NH_3 is above all synthesized with the Haber process, where N_2 and water gas are converted to NH_3 under high temperature and high pressure with the assist of catalysts (Xue, Chen, Yan, Zhao, et al. 2019). Every year, the synthesis of NH_3 consumes about 2% of global energy, leading to serious carbon dioxide emission. Thus, it is urgent to develop a green synthesis of NH_3 under surrounding conditions.

Recently, photocatalytic synthesis of NH_3 has become a hot research frontier, where researchers are mainly focusing on the reduction of gaseous nitrogen (Guo et al. 2019; Liu, Li, Wu, et al. 2019; Zhang, Zhao, et al. 2019). In chapter 4 and chapter 5, we used the nano-structure control and organic π-conjugated molecule modification to improve the photocatalytic N_2 fixation efficiency. However, the research on photochemical N_2 fixation is still limited in the laboratory, because the strong bond energy of N≡N bonds and the poor solubility of N_2 make the catalytic NH_3 yield efficiency low (Guo et al. 2019). Compared with N_2, the required energy for the cleavage of N=O is only 21.68% as that of N≡N bonds. In addition, the solubility of NO_3^- is 40000 times higher than that of N_2. Therefore, if the waste NO_3^- can be converted to NH_3, the conversion of environmental hazards to valuable energy resources will be more sustainable for the planet.

g-C_3N_4 is a kind of metal-free organic material, which is a rising star in photocatalysis

because it has the advantages of facile synthesis, wide sources and good photocatalytic activity for redox reactions (Fu et al. 2019). In recent years, several kinds of g-C_3N_4-based photocatalysts have been prepared and applied in NO_3^- wastewater treatment, such as TiO_2/g-C_3N_4 (Zhang et al. 2020), Mn_2O_3/g-C_3N_4 (Zhao et al. 2018), g-C_3N_4@AgPd heterojunction (Liu et al. 2020) etc. However, the main aim is to convert NO_3^- to N_2 to reduce environmental hazards. Compared with the generation of N_2, the reduction of NO_3^- to NH_3 is more challenging in terms of kinetics and thermodynamics, as it is an eight-electron process with multiple steps (Hirakawa et al. 2017). On the other hand, many ruthenium-containing compounds exhibit good catalytic properties because of their unique electronic structure (Baek et al. 2020; Cao et al. 2019; Li, Shan, et al. 2019; Lin et al. 2019). Meanwhile, Ru can absorb the light in the visible range, and it is being massively studied for solar-energy utilizations (Elcheikh Mahmoud et al. 2019; Hennessey et al. 2019). Nevertheless, toxic reducing agents like ethylene glycol are usually required to reduce Ru^{3+} to Ru^0, making the synthesis complex, dangerous and un-ecofriendly (Li, Zhang, et al. 2019). Until now, Ru adjusted g-C_3N_4 photocatalysts for highly efficient NO_3^- reduction to NH_3 has never been reported, and the reaction mechanism is not clear.

In this chapter, we report a green synthesis of Ru adjusted g-C_3N_4 nanosheets with enhanced activity on the photochemical reduction of NO_3^- to NH_3. Herein, waste green tea bags were used to reduce the Ru^{3+}, and the photocatalytic activity of the optimized sample was 2.93-fold as that of bulk g-C_3N_4 under simulated sunlight irradiation. Depend on experimental and theoretical results, the introduction of Ru to g-C_3N_4 can

not only boost the solar energy utilization, the adsorption of NO_3^-, but also boost the separate speed of electron-hole pairs. The thermodynamic energy barrier for the rate-determining step in NO_3^- reduction to NH_3 process is calculated to be less than 0.75 eV, which is much lower than the competing H_2 generation (0.98 eV) and N_2 formation (1.36 eV), leading to the preference of generating NH_3. This research might provides a novel approach to prepare metallic particle-based photocatalysts for highly efficient photocatalytic NO_3^- reduction to synthesize NH_3.

6.2 Experimental sections

6.2.1 Synthesis of g-C_3N_4 nanosheets

g-C_3N_4 was prepared via the thermal polymerization of dicyandiamide. Firstly, 5 g of dicyandiamide was put in a 50-mL corundum crucible without the lid. Then the crucible was transferred into the oven and heated from 25 to 540 °C with the temperature-increase rate of 4 °C/min. After heating at 540 °C for 4 h in air, the bulk g-C_3N_4 was obtained. The g-C_3N_4 nanosheets were obtained via the ultrasonic peeling of bulk g-C_3N_4 in H_2O. In details, 500 mg of bulk g-C_3N_4 was added in 800 mL H_2O and put under ultrasonic bath for 24 h. Finally, the ultrathin g-C_3N_4 nanosheets were successfully obtained and named as 2D-CN.

6.2.2 Synthesis of Ru/g-C_3N_4

Herein, we used waste green tea as the reduction regent to prepare Ru modified g-C_3N_4 (**Scheme 6.1**). To get simulated waste tea bags, 5 tea bags were put in boiled water for 20 min. Then the 5 used tea bags were put in 500 mL and boiled for 30 min. After that,

the tea water was gone through a filter for further use. A certain amount of $RuCl_3$ and 0.5 g of g-C_3N_4 nanosheets were put into 150 mL prepared tea water and under magnetic stir for 24 h. Finally, the powder was cleaned by H_2O and ethanol for 5 times, and then dried at 60 °C for 4 h. The amounts of $RuCl_3$ used were 0.005, 0.01 and 0.038 g, and the obtained samples were named as CN-Ru-0.5, CN-Ru-1 and CN-Ru-3, respectively.

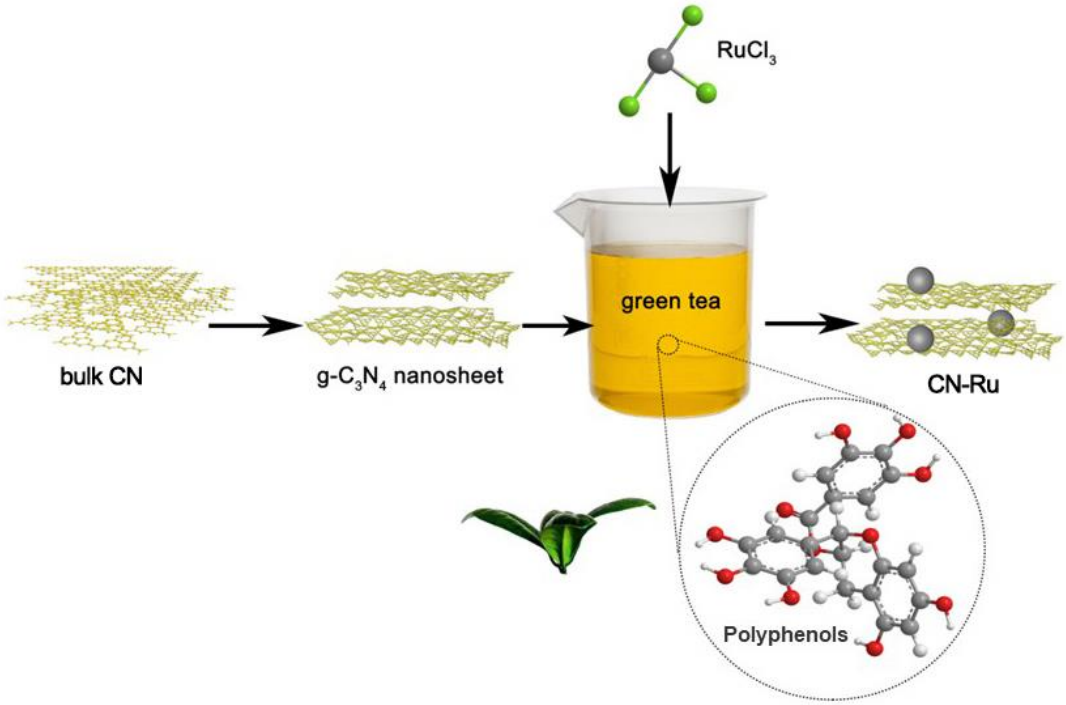

Scheme 6.1 Schematic illustration of the preparation of Ru modified g-C_3N_4 nanosheets.

6.2.3 Characterizations

The XRD patterns of the samples were tested with a Bruker D8 Discover XRD with intense Cu *K*α radiation (40 kV and 40 mA, λ = 1.5406 Å) at room temperature. The morphology observation on the materials was carried out using a Zeiss Supra 55VP SEM, with an operating voltage of 5 kV. HAADF-STEM and energy dispersion X-ray spectroscopy mapping were performed on a double-corrected FEI Themis-Z 60-300 TEM equipped with ChemiSTEM EDS detector system for ultra-high count rates. The

XPS of the samples were tested with a Thermo Fisher Scientific K-Alpha+ X-ray photoelectron spectroscopy. The UV-vis DRS of prepared samples were obtained from a Perkin Elmber Lambda 950 UV/VIS/NIR spectrometer, using high-purity $BaSO_4$ as the blank reference. PL spectra were obtained from a Shimadzu RF-6000 fluorescence spectrometer excited at 325 nm. The photocurrent and EIS curves of the samples were obtained from an electrochemical working station (CHI-760E) in 0.1 M Na_2SO_4 solution.

6.2.4 Photocatalytic activity testing

The photocatalytic nitrate reduction performance was carried out with a self-made quartz reactor under simulated sunlight irradiation. During the reaction process, the light intensity was 600 mW/cm^2 (HSX-F300) and it was measured by a radiometer. The distance between the light and the reactor was 10 cm. Firstly, 20 mg of the samples were weighed and put into the reactor. Then 95 mL of $NaNO_3$ (10 mg/L) solution and 5 mL of formic acid (200 μL/L) was added. Before the reaction, argon was purged into the solution to remove air. After 2-h strong stir to make the powder catalysts uniformly dispersed in the solution, the light was turned on and the light irradiation lasted 4 h. In each hour, 3 mL of liquid was sampled from the reactor. The concentration of ammonium was measured by UV-vis spectrometer using Nessler's reagent method and was further verified by 1H-NMR analysis. The concentration of NO_3^- and NO_2^- were measure by a high-pressure integrated capillary anion chromatography.

6.2.5 Density functional calculation

The calculations of geometry structures and energies were carried out by DFT with Vienna ab-initio simulation package (VASP) (Kresse & Furthmüller 1996a, 1996b; Kresse, Furthmüller & Hafner 1994; Kresse & Hafner 1993). The interactions between ion cores and valence electrons were illustrated by the projector augmented wave (PAW) method (Blöchl 1994; Kresse & Joubert 1999). The generalized gradient approximation with the Perdew-Burke-Ernzerhof was adopted as the exchange-correlation functional (Perdew, Burke & Ernzerhof 1996). The used kinetic cutoff energy was 400 eV. The integration of the Brillouin zone was conducted using a 3 × 3 × 1 Monkhorst-Pack grid (Monkhorst & Pack 1976). The geometries were optimized using a force-based conjugate-gradient method (Kresse & Furthmüller 1996b), until the energy was converted to 1.0×10^{-4} eV/atom and the force to 0.05 eV/Å. In this study, the spin polarization was also considered.

g-C_3N_4 was prepared with a 2 × 2 supercell and CN-Ru was constructed by inserting three Ru atoms into the above g-C_3N_4 model. In the optimization process, all the atoms were allowed to relax. A vacuum layer of 10 Å was applied with the c direction normal to the surface to avoid periodic interactions.

To investigate the stability of NO_3^- on g-C_3N_4 and CN-Ru, the adsorption energies were performed, as follows,

$$E_{ads} = E_{NO3@S} - E_{NO3} - E_S$$

Where $E_{NO3@S}$ is the total energy of NO_3 and substrate (S= C_3N_4 and CN-Ru), E_{NO3} and E_S are the energies of isolated NO_3 and substrates, respectively. The more negative

value corresponds to the more stable chemical adsorption.

To reveal the activity of NO_3^- reduction process, the free energy diagrams was estimated as follows:

$$\Delta G = \Delta E + \Delta ZPE - T\Delta S$$

where ΔE was the total energy change based on the DFT calculations, ZPE and S was the zero-point energy and entropy, respectively, T was the temperature (298.15 K). The free energy of ($H^+ + e^-$) at standard conditions is assumed as the energy of 1/2 H_2 (Nørskov et al. 2004).

6.3 Results and discussion

6.3.1 Structure and morphology

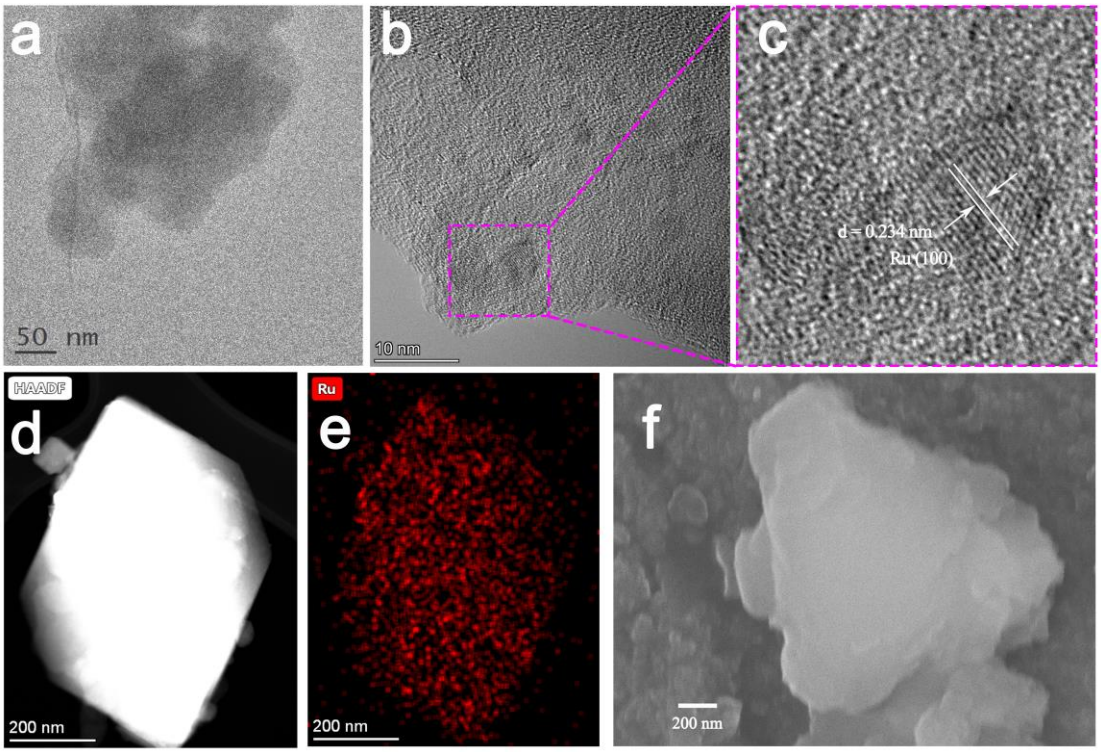

Figure 6.1 HRTEM image of g-C_3N_4 nanosheets (a), CN-Ru-1 (b) and the zoom-in part of the lattice (c), high-angle annular dark-field image (d), energy dispersive spectroscopy for Ru element mapping (e), and SEM image of CN-Ru-1 (f).

In the XRD patterns of g-C_3N_4 (**Figure 6.2**), 2 distinct peaks at 13.1 and 27.1° can be

assigned to the (100) and (002) crystal plane diffraction (JCPDS 87-1526) (Hao, Hao, et al. 2017). After peeled off by ultrasonic power, the peak intensity decreased, indicating the reduced crystallinity. Since the loaded amount of Ru is not high, it cannot be detected by XRD. Then HRTEM and SEM were used to explore the morphology of the prepared samples. As shown in **Figure 6.1a**, the g-C_3N_4 nanosheets showed an ultrathin film layer structure. The CN-Ru-1 sample had the same morphology as 2D-CN with Ru particles loaded on the g-C_3N_4 nanosheets (dark spots in **Figure 6.1b**). The size of the Ru particles was less than 5 nm. To further investigate the lattice, the Ru particles were zoomed in and displayed in **Figure 6.1c**. The lattice distance of 0.234 nm can be indexed to the (100) of metallic Ru. Additionally, the HAADF image and EDS for Ru element mapping were obtained to further confirm the component of the CN-Ru sample. As exhibited in **Figures 6.1d and 6.1e**, Ru particles are uniformly distributed on g-C_3N_4 nanosheets. SEM analysis was also employed to study the morphology of CN-Ru-1 (**Figure 6.1f**). In the SEM image, we can only see the nanosheet structure of g-C_3N_4, since the size of Ru particles was too small to be observed by SEM.

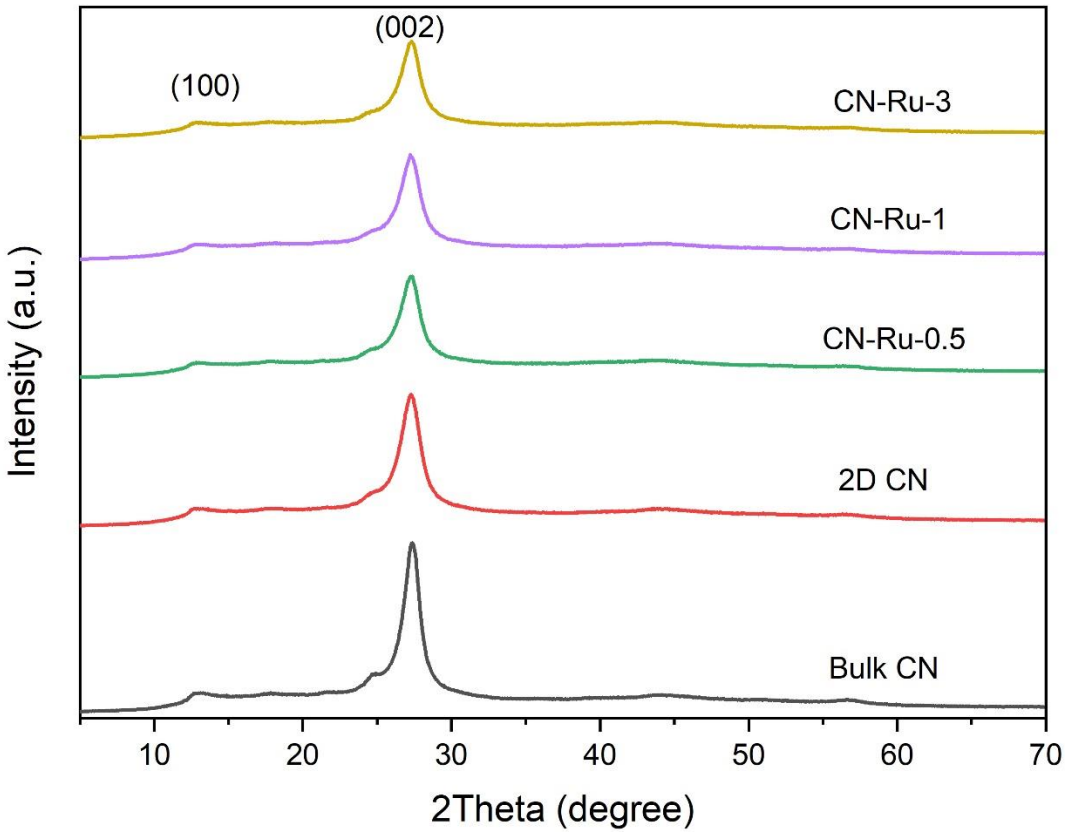

Figure 6.2 The XRD patterns of bulk CN, 2D-CN and CN-Ru samples.

Then XPS was used to study the components of the prepared samples. **Figure 6.3a** and **6.3b** are the narrow C 1*s* spectra of 2D-CN and CN-Ru-1. The three peaks of 2D-CN at 293.6, 287.9 and 284.6 eV can be assigned to the conjugated π electrons, sp^2-hybridized C and C–C bonds. Compared with 2D-CN, two new peaks appeared in the narrow XPS spectra of C of CN-Ru-1. The peak at 286.1 eV was attributed to C–O which came from the green tea (**Figure 6.3b**) (Kehrer et al. 2019). The other new peak at 280.2 eV is associated with Ru^0 (Khaniya et al. 2020). Both 2D-CN and CN-Ru-1 have 3 peaks in the narrow N 1*s* spectra. In **Figure 6.3c**, the three peaks at 404.4, 400.0 and 398.4 eV of 2D-CN are attributed to the charging effect, tertiary nitrogen and sp^2-hybridized nitrogen. Notably, the three peaks of N of CN-Ru-1 shifted to 404.9, 400.1 and 398.6 eV, which was caused by the interaction between 2D-CN and Ru (Lu, Hao,

et al. 2018).

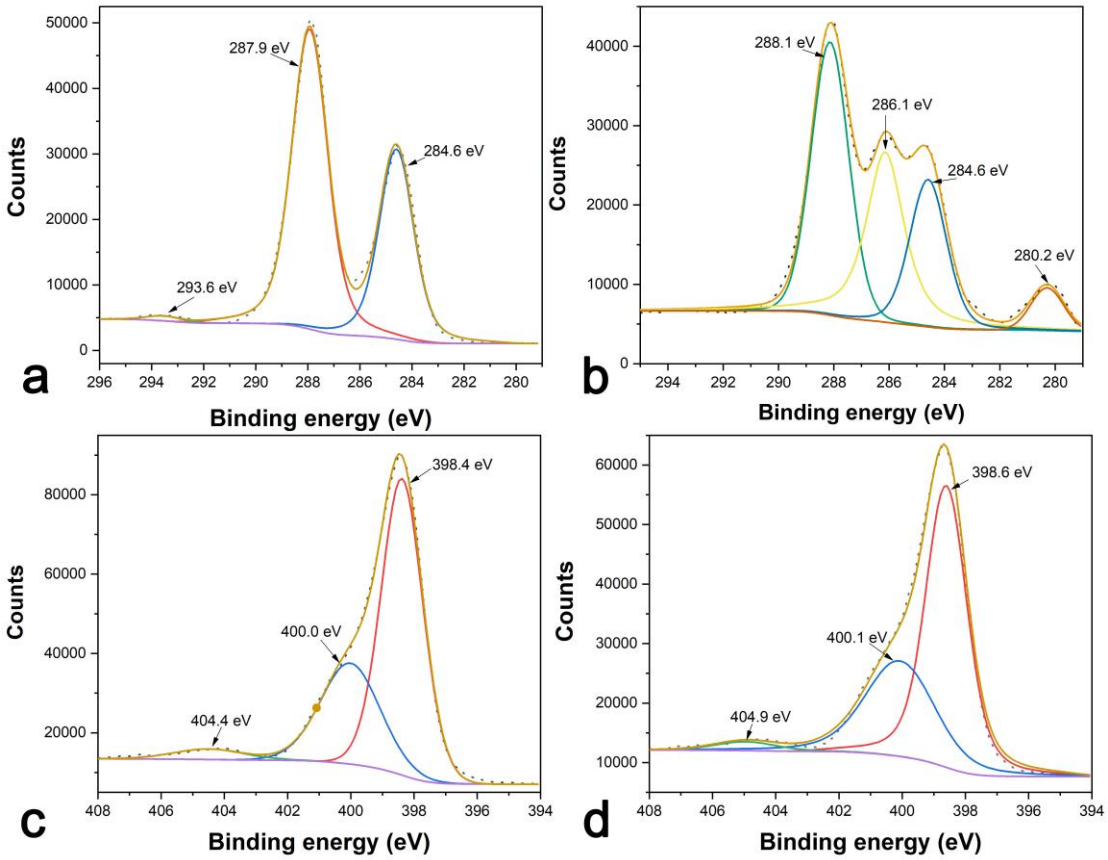

Figure 6.3 Narrow C 1*s* XPS spectra of 2D-CN (a) and CN-Ru-1 (b). Narrow N 1*s* XPS spectra of 2D-CN (c) and CN-Ru-1 (d).

Based on the XRD, SEM, TEM and XPS results, we can say that metallic Ru particle modified g-C_3N_4 nanosheets were successfully fabricated.

6.3.2 Enhanced photocatalytic NO_3^- reduction to NH_3

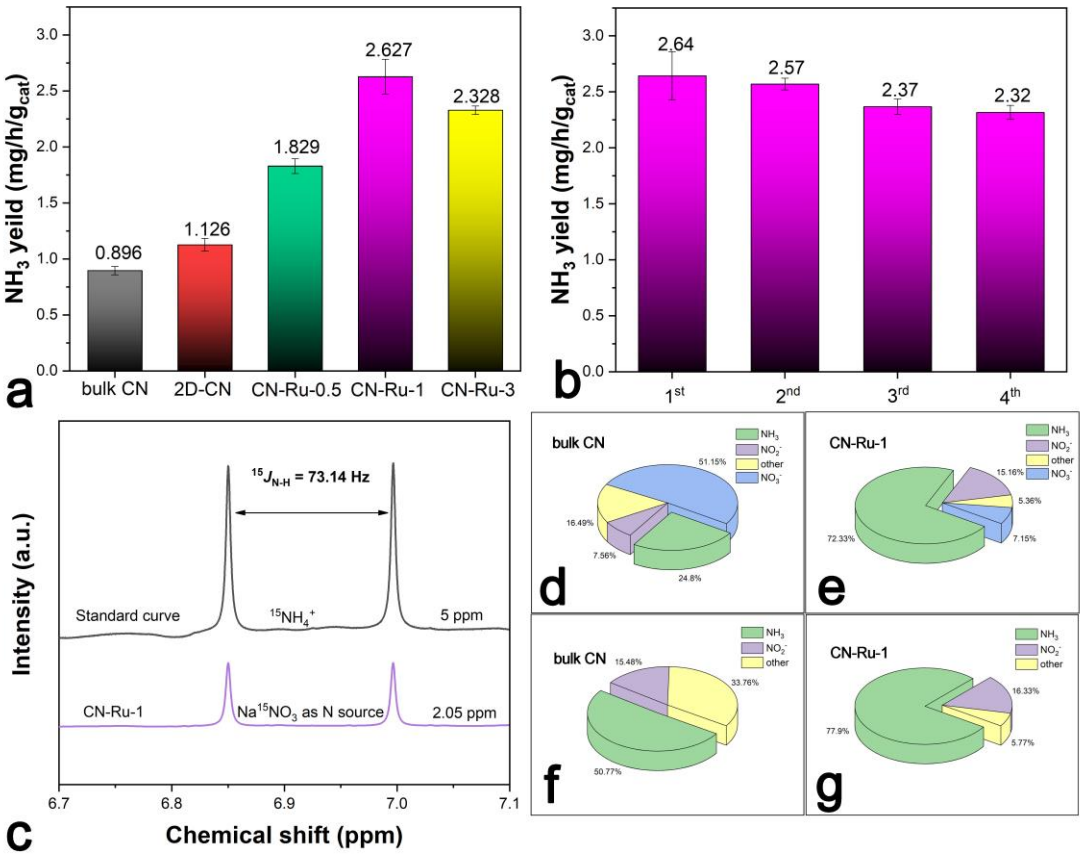

Figure 6.4 (a) Photocatalytic activity of bulk CN, 2D-CN and CN-Ru samples, and (b) cycle stability of CN-Ru-1. (c) The NMR spectra of $^{15}NH_4Cl$ standard solution and the final photoreduction production of $Na^{15}NO3$ by CN-Ru-1. The proportions of productions and NO_3^- after photocatalytic reaction by (d) bulk CN and (e) CN-Ru-1. The selectivity of photocatalytic reduction of NO_3^- by (f) bulk CN and (g) CN-Ru-1.

Herein, we used photocatalytic NO_3^- reduction to NH_3 to evaluate the catalytic activity of samples. After 4-hour simulated sunlight irradiation, all the samples exhibited apparent photocatalytic activity on the reduction of NO_3^- to NH_3 (**Figure 6.4a**). The NH_3 yield rate of 2D-CN was 1.126 mg/h/g_{cat}, and it was 1.26-fold as that of bulk g-C_3N_4. When metallic Ru was used to modify the 2D-CN, the photocatalytic activity increased remarkably. Among all the samples, CN-Ru-1 was the most active one (2.627 mg/h/g_{cat}) and its activity is 2.93 times better than bulk g-C_3N_4. Cycle stability is crucial

for the study and application of photocatalysts. After the fourth cycle, the NH_3 yield of CN-Ru-1 was still 2.32 mg/h/g_{cat}, which was 88.16% as the fresh catalyst, indicating good cycle stability for re-usage (**Figure 6.4b**).

To confirm the source of NH_3 generated, we carried on the ^{15}N isotope experiment with $Na^{15}NO_3$. A series of $^{15}NH_4Cl$ solutions with different concentrations were firstly used to generate a standard line and then the concentration of photocatalytic reactions can be analyzed. As shown in **Figure 6.4c**, the standard 1H-NMR spectrum of $^{15}NH_3$ had two peaks with a coupling constant of 73.14 Hz. In the solution after photocatalytic reaction of CN-Ru-1 with $^{15}NO_3^-$, two characteristic $^{15}NH_3$ peaks were also found, and the calculated concentration of NH_3 was 2.05 mg/L, which well matched the results of UV-vis spectrophotometry. The NMR results can confirm that the formation of NH_3 is attributed to the photocatalytic reduction of NO_3^-.

Besides NH_3, there might be some other products of the NO_3^- reduction. Herein, we used ion chromatography to measure the concentration of NO_3^- and NO_2^-. After 4-h light irradiation, bulk CN reduced 48.85% of the NO_3^- (10 mg/L), 50.77% of which was converted to NH_3. Under the same condition, CN-Ru-1 eliminated 92.85% of NO_3^- and the NH_3 selectivity was 77.9% (**Figure 6.4d**). The UV-vis spectrophotometry, 1H-NMR and ion chromatography results confirmed that both the NO_3^- conversion rate and NH_3 selectivity were significantly increased by CN-Ru-1, compared with bulk CN.

In **Table 6.1**, we summarized several typical g-C_3N_4, TiO_2 and other materials for photocatalytic NO_3^- reduction in literature for comparison. Many materials can achieve highly efficient NO_3^- removal, whereas the ammonia selectivity is quite low. Pd/TiO_2

can get a high NH_3 selectivity of 76.9%, but its catalytic activity is really poor (Kominami et al. 2001). Nevertheless, the CN-Ru-1 reported in this work can simultaneously realize both high NO_3^- removal and high NH_3 selectivity.

Table 6.1 The activity and NH_3 selectivity over g-C_3N_4, TiO_2 and other materials.

Materials	**Light range**	**Reaction time**	**NO_3^- removal**	**NH_3 selectivity**	**Reference**
Mn_2O_3/g-C_3N_4	UV-vis	2 h	94.5%	N/A	(Zhao et al. 2018)
g-C_3N_4@AgPd	365 nm	3 h	87.4%	N/A	(Liu et al. 2020)
TiO_2/g-C_3N_4	visible	16 h	40.3%	Less than 15%	(Zhang et al. 2020)
Cu_2O-Cu^0@Fe^0	365 nm	1 h	100%	Less than 5%	(Zhang, Wang, et al. 2019)
AgCl/TiO_2	365 nm	30 min	94.5%	Less than 8%	(Geng et al. 2018)
Ag_2O/P_{25}	365 nm	4 h	97.2%	Less than 17%	(Ren et al. 2015)
Pd/$GdCrO_3$	365 nm	100 min	95.5%	Less than 2%	(Hou et al. 2018)
P_{25}	365 nm	2 h	52.5%	6%	(Liu et al. 2016)
Pd/TiO_2	365 nm	3 h	2.6%	76.9%	(Kominami et al. 2001)
Cu/TiO_2	365 nm	3 h	100%	45%	(Sa et al. 2009)
g-C_3N_4/Ru	UV-vis	4 h	92.85%	77.90%	This work

6.3.3 Mechanism of the enhanced performance

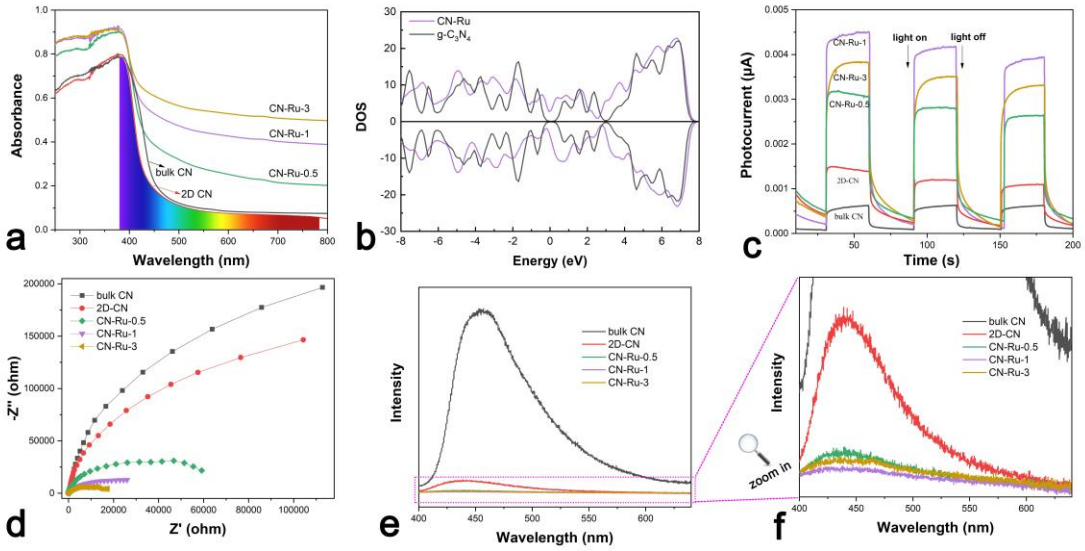

Figure 6.5 UV-vis DRS of bulk CN, 2D-CN and CN-Ru samples (a). Density of states of g-C_3N_4 and CN-Ru (b). Photocurrent response (c), EIS (d) and PL spectra (e, f) of bulk CN, 2D-CN and CN-Ru samples.

Light absorption is an essential step for photocatalytic reaction. **Figure 6.5a** showed the UV-vis DRS of bulk CN, 2D-CN and CN-Ru samples. The absorption edge of bulk CN was at about 460 nm, indicating a bandgap of 2.70 eV. When bulk CN was converted to 2D-CN, the absorption edge had a blue shift to 430 nm, with a wider bandgap of 2.88 eV. When the 2D-CN was modified by metallic Ru particles, the absorption edge showed a redshift. Meanwhile, the light absorption in the visible light region was also significantly increased. The increased light absorption enabled to make the catalysts absorb more photons, boosting the solar energy utilization ratio. The density of states of g-C_3N_4 and CN-Ru are calculated by DFT (**Figure 6.5b)**. Compared with g-C_3N_4, the introduction of metallic Ru can bring some metallicity to the composite catalysts, which is beneficial to the transfer and separation of photocatalytic generated electron-hole pairs (Wang et al. 2018).

In order to explore more direct evidence about the transfer and separation of photogenerated electron-hole pairs, the photocurrent response, EIS and PL spectra of bulk CN, 2D-CN and CN-Ru samples were tested. **Figure 6.5c** is the photocurrent response image. All the tested samples had apparent and rapid photocurrent response under simulated sun light irradiation. Among all the samples, the photocurrent intensity of CN-Ru-1 was the strongest, which followed the same trend as the photocatalytic activity, indicating that CN-Ru-1 had the fastest separation and transfer of electrons and holes. In the EIS Nyquist plot, the bulk CN had the largest arc radius because of its poor conductivity. The 2D-CN got a smaller arc radius as it had better conductivity than bulk CN. When the 2D-CN got modified by metallic Ru, the arc radius of the EIS Nyquist plot significantly decreased, because Ru had strong conductivity. The more metallic Ru loaded, the better conductivity the sample got. The PL spectra of bulk CN, 2D-CN and CN-Ru samples were displayed in **Figure 6.5e** and **f**. Bulk CN showed a broad and strong emission spectrum with profiles slightly deviating from a perfect Guanine curve centred at about 460 nm. Compared with bulk CN, the PL intensity of the other samples decreased significantly, which mean the recombination of photoinduced charge carriers was obstructed, and it is helpful for the enhanced photocatalytic activity (Du et al. 2017). Experimental results on NO_3^- reduction have revealed that Ru modified g-C_3N_4 plays a crucial role in improving NH_3 yield compared with pure g-C_3N_4. To indeed reveal the reaction mechanism and the origin of high activity and selectivity of CN-Ru, the density functional theory calculation is performed. NO_3^- adsorption, the first step of NO_3^- reduction, was first calculated, and the optimized adsorption structures, as well as the

adsorption energies are listed in **Figure 6.6a** and **b**. The adsorption energy of NO_3^- on g-C_3N_4 was -1.85 eV and it was -3.75 eV on CN-Ru. It is clearly seen that Ru modification increased the NO_3^- stability by 2.03 times compared with pristine g-C_3N_4, indicating the following NO_3^- reduction step proceeds more easily, consistent with the experimental observations.

Furthermore, metallic Ru particles involve a high spin density on Ru cluster and positive Bader charge, as well as a zero-gap, which can enhance the electron transfer ability (**Figures 6.6.c** and **d**). Since Ru cluster got a positive Bader charge, the photocatalytic generated electrons for g-C_3N_4 can be accumulated on Ru, making it as the active sites. At the same time, the CN-Ru system got some magnetic properties, and the spin density is concentrated on Ru. All these electronic structure results are responsible for the enhanced photochemical reduction of NO_3^- on CN-Ru.

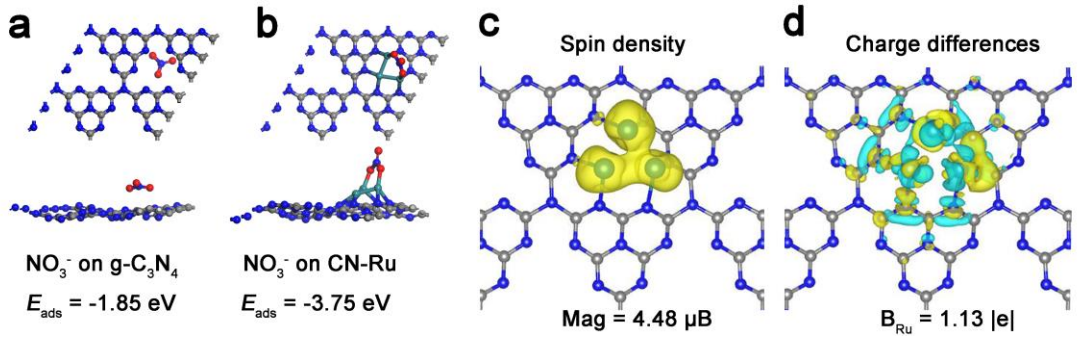

Figure 6.6 Adsorption structures and calculated adsorption energies of NO_3^- adsorbed on g-C_3N_4 (a) and CN-Ru (b). Optimized spin density (c) and charge differences (d) of CN-Ru.

To indeed reveal the role of metallic Ru particles in the NO_3^- reduction process, the free energy diagrams of NO_3^- reduction on g-C_3N_4 and CN-Ru were calculated. Compared with the generation of NH_3, there are two main competing reactional products for the photocatalytic reduction of NO_3- including H_2 and N_2. For g-C_3N_4, it is very easy to

take part in hydrogen generation reaction, while the formation of N_2 is very difficult because a higher thermodynamic energy barrier of 2.33 eV should be overcome (**Figure 6.7a**). As for CN-Ru, the thermodynamic energy barriers of the formation of H_2 and N_2 are 0.98 and 1.36 eV (**Figure 6.7b**). All free energy curves are down-hill from NO_3^- to HNO_2 and although the reaction pathway is different, the thermodynamic energy barrier for the rate-determining step in this process is all calculated to be less than 0.75 eV (**Figure 6.7c**), which is much lower than those of 2H→H_2 (0.98 eV) and 2N→N_2 (1.36 eV), suggesting that induced Ru cluster played a key role in the enhancement of the photocatalytic activity and selectivity for NO_3^- reduction to form NH_3, in fine agreement with the experimental results.

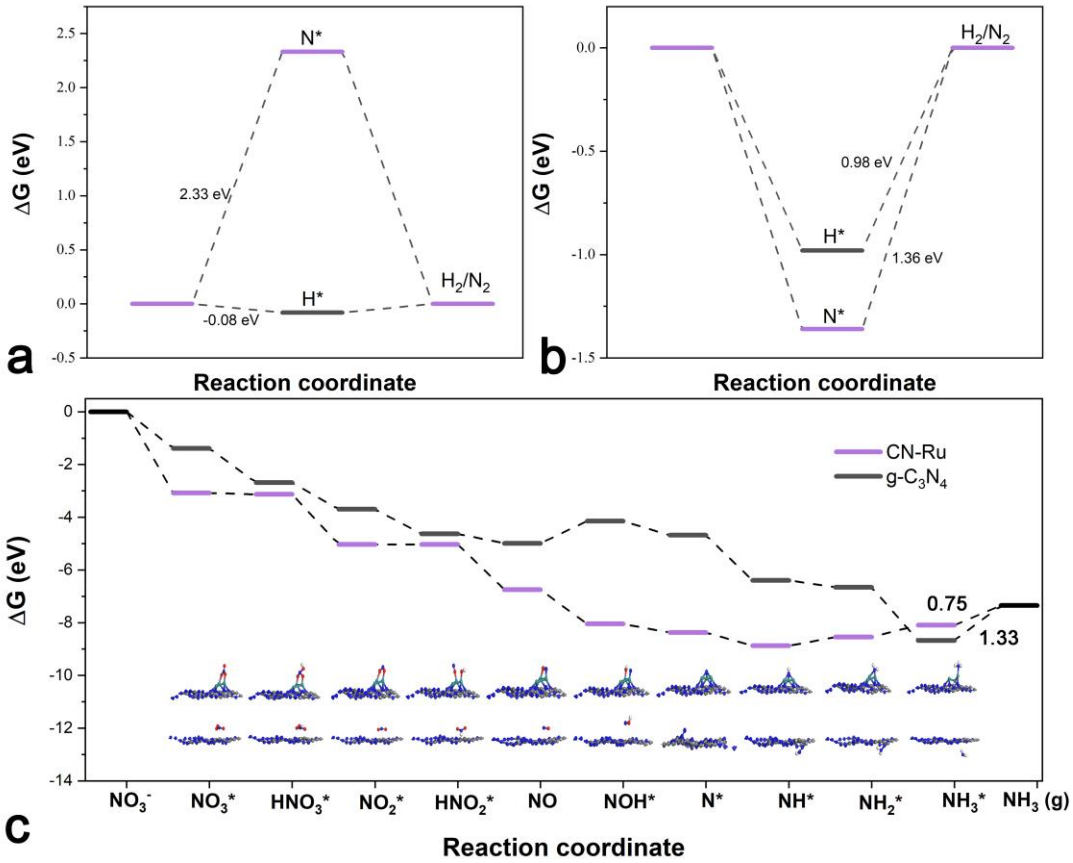

Figure 6.7 Calculated free energy differences between the formation of H_2 and N_2 on g-C_3N_4 (a) and CN-Ru (b). Calculated free energy changes of NO_3^- reduction to NH_3 on g-C_3N_4 and CN-Ru

(c).

Based on the experimental and calculated results, the mechanism for the highly boosted photocatalytic NO_3^- reduction to NH_3 activity can be summarized as follow. Firstly, the introduction of metallic Ru caused a redshift of the absorption edge as well as broad absorption in visible light range, which boosted the absorption of photons and the utilization of solar light. Secondly, CN-Ru samples have much better conductivity and higher separation efficiency of photogenerated electron-hole pairs than g-C_3N_4. Thirdly, the high spin density of Ru cluster and its positive Bader charge can accumulate electrons, making the adsorption and cleavage of NO_3^- easier. More importantly, the thermodynamic energy barrier for the rate-determining step in this process is all calculated to be less than 0.75 eV (**Figure 6.7c**), which is much lower than the competing H_2 generation (0.98 eV) and N_2 formation (1.36 eV), leading to the preference of generating NH_3.

Meanwhile, the average reduction potential of green tea is about 0.219 V, indicating that the approach reported in this work can be expanded to the synthesis of other metal-based materials.(Oakes 2013) In **Figure 6.8**, we summarized the elements that can be reduced to zero-valent theoretically, including Tc, Ru, Cu, etc., which would potentially use the proposed approach.(Vanýsek 2012)

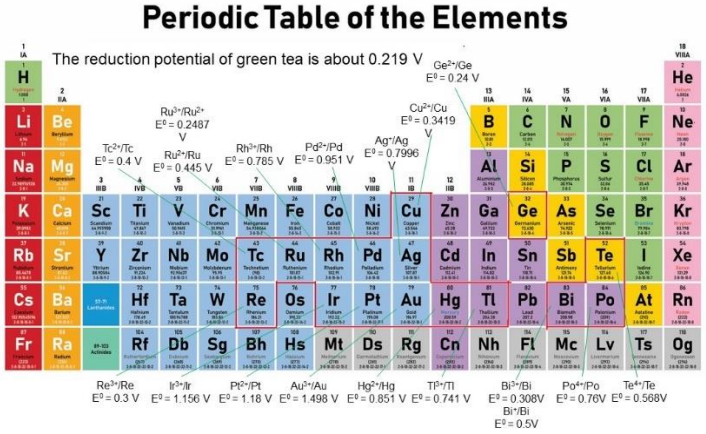

Figure 6.8 The elements that can be reduced by green tea theoretically.

6.4 Conclusion

In summary, we used a facile and green approach to synthesize novel metallic Ru modified g-C_3N_4 nanosheets as catalysts for enhanced photochemical NO_3^- reduction to NH_3. The optimal sample (CN-Ru-1) had the highest NH_3 yield rate of 2.627 mg/h/g_{cat} and it was 2.93 times as that of bulk CN. After 4-hour light irradiation, CN-Ru-1 eliminated 92.85% of NO_3^- and the NH_3 selectivity was 77.9%. After four cycles, the sample still had good photocatalytic performance (88.16% as the fresh catalyst). NMR and ^{15}N isotope labelling provided solid evidence that the N of NH_3 was from the reduction of NO_3^-. The g-C_3N_4 nanosheets modified by metallic Ru particles have stronger light absorption, better conductivity and more rapid separation of electron-hole pairs. With the enhanced adsorption energy of NO_3^- and the low thermodynamic energy barriers, the photocatalytic activity and selectivity were increased significantly. The results and findings of this work may provide a new platform for the facile and green synthesis of metal particles modified photocatalysts for reducing NO_3^- to NH_3 under ambient conditions.

Chapter 7 Boosted selective catalytic nitrate reduction to ammonia on carbon/bismuth/bismuth oxide photocatalysts

Related publication:

Boosted selective catalytic nitrate reduction to ammonia on carbon/bismuth/bismuth oxide photocatalysts. Journal of Cleaner Production. (Major revision)

7.1 Introduction

Nitrate contamination is a serious environmental pollution, which has caused severe deterioration to both surface water and groundwater(Koh, Lee & Lee 2020; Kumar et al. 2020). The nitrate pollutant sources include the abuse of fertilizers, the use of animal manure, the seepage of domestic and industrial wastewater, the overexploitation of groundwater, the deposition of atmospheric nitrogen oxides, etc (Liu, Wu & Zhang 2005; Peña-Haro, Pulido-Velazquez & Sahuquillo 2009; Wakida & Lerner 2005). Nitrate can be accumulated in plants and livestock via the food chain, and it may eventually get into the human body. A high level of nitrate is toxic to human, as it can be converted to nitrite, causing respiratory and reproductive system problems. Besides, it is particularly harmful to infants (Ahada & Suthar 2018; Rehman et al. 2020; Rezaei et al. 2019). Therefore, highly efficient and cost-effective approaches should be developed to minimize the hazards of nitrate.

It is difficult for nitrate to form co-precipitation of being adsorbed, since nitrate has high solubility and good stability. Thus, the traditional wastewater treatment

approaches are not suitable for nitrate wastewater purification (Fernández-Nava et al. 2008; Park & Yoo 2009). The current industrial nitrate wastewater treatment methods mainly include reverse osmosis (Schoeman & Steyn 2003), electrodialysis (Elmidaoui et al. 2001), ion exchange (Samatya et al. 2006), catalytic denitrification (Pintar, Batista & Levec 2001), chemical denitrification (Li et al. 2017) and biological denitrification (Soares 2000). The reverse osmosis, electrodialysis and ion exchange for nitrate treatment are expensive and not suitable for mass application. Chemical denitrification would generate a lot of by-productions and can lead to secondary pollution. Biological denitrification usually cost a long period and the removal efficiency is relatively low. Compared with these mentioned methods, catalytic denitrification has better potential because it can convert nitrates to nitrogen or ammonia in a very short time (Kapoor & Viraraghavan 1997; Lemaignen et al. 2002). But better catalysts with low cost and high activity still need further investigation.

In recent years, using photocatalytic technology for the treatment of nitrate wastewater has become a hot issue (Freire et al. 2020; Velu et al. 2021). The photoexcited electrons can convert nitrate to ammonia or nitrogen within a few hours (Hirakawa et al. 2017). The photocatalytic nitrate reduction to ammonia is of great significance particularly, which is a process of converting waste chemicals to valuable resources. Nevertheless, the photocatalytic activity is usually not high because most photogenerated electrons and holes get recombined, and only a tiny amount of charge carriers can transfer to the surface of catalysts to take part in the photocatalytic reactions (Wu et al. 2015). During the nitrate reduction process, the reactions involve a lot of complex processes towards

the formation of nitrogen and ammonia (Garcia-Segura et al. 2018). Across these reactions, the nitrate to ammonia usually has low selectivity, because it is an 8-electron process and is difficult to be achieved dynamically and thermodynamically (Hirakawa et al. 2017). Thus, photocatalytic synthesis of ammonia with nitrate as nitrogen source is still challenging. In chapter 6, we reported a Ru cluster modified g-C_3N_4 for enhanced photocatalytic nitrate reduction to ammonia activity and selectivity. While the selectivity is still not high enough for further application. Thus we are seeking approaches to increase the selectivity and photocatalytic activity.

Recently, bismuth-based photocatalysts have shown outstanding performance in photochemical redox reactions (Hao, Wang, et al. 2017; Liu, Hu & Yu 2020; Lu, Hao, et al. 2018). More importantly, bismuth-based materials are high-potential candidates for artificial NH_3 synthesis under surrounding conditions, because of the advantages of the unique structure (Guo et al. 2019). Nevertheless the photocatalytic activity has not reached the requirement for mass application. Using localized surface plasmon resonance of noble metals to enhance the photocatalytic activity of bismuth-based materials is an effective strategy as the noble metals usually work as a co-catalyst to boost the solar energy absorption and charge separation (Zhou et al. 2012). For instance, Hu et al. found that the surface plasmon resonance of aurum can provide sufficient energy for the activation and cleavage of N_2 molecules (Hu et al. 2019). Chen et al. reported an aurum nanoparticle modified metal-organic framework photocatalyst, which can achieve an ammonia yield of 18.9 mmol/g/h (Chen, Hao, et al. 2021). Hou et al. prepared a core-shell Ag/SiO_2@TiO_2, and the photocatalyst showed remarkable

photocatalytic removal of high-concentration nitrate, since the SPR of Ag (Hou et al. 2021). It has been confirmed that metallic bismuth also has surface plasmon resonance recently (Dong et al. 2014). However, using the surface plasmon resonance of bismuth to improve photocatalytic nitrate reduction has not been reported. Meanwhile, the synthesis of metallic bismuth usually requires the consumption of sodium borohydride, which is flammable, corrosive and toxic. As such, more reliable synthesis is urgently desired.

In this chapter, we report a novel and facile of bismuth/bismuth oxide photocatalysts, which showed a highly efficient photocatalytic reduction of nitrate and remarkable selectivity for the generation of ammonia due to the surface plasmon of metallic bismuth and enhanced separation of electron-hole pairs by carbon. No strong reducing reagent was used in the preparation process. The results of this work may contribute to the advance of artificial ammonia synthesis under ambient conditions.

7.2 Experimental section

7.2.1 Synthesis of materials

In this chapter, a facile one-pot approach was employed to synthesize BiO-Bi materials. In details, 6 mmol of $Bi(NO_3)_3 \cdot 5H_2O$ was added to 80 mL of ethylene glycol and stirred for 2 h to get a uniform solution. Then the solution was poured into a 100-mL polytetrafluoroethylene autoclave. The solvothermal reactions happened under different temperatures (120, 140, 160 and 180 °C). After cooled to room temperate, the obtained powder was washed with H_2O and ethanol 5 times. Then the samples were

dried at 60 °C for 24 h in air and the obtained samples were named as BiO-120, BiO-140, BiO-160 and BiO-180, respectively.

7.2.2 Characterizations

The XRD patterns of the samples were tested with a Bruker D8 Discover XRD with intense Cu *K*α radiation (40 kV and 40 mA, λ = 1.5406 Å) at room temperature. The morphology observation on the materials was carried out using a Zeiss Supra 55VP SEM, with an operating voltage of 5-15 kV. The images of EDS for elemental mapping were obtained with the Oxford Ultim Max. The Transmission electron microscopy images were obtained from a FEI Themis-Z Double-corrected 60-300 kV S/TEM. The XPS was tested with Thermo Fisher Scientific K-Alpha+. The UV-vis DRS of prepared samples were obtained from a Perkin Elmber Lambda 950 UV/VIS/NIR spectrometer, using high-purity BaSO4 as the blank reference. A FT-IR Spectroscopy (Nicolet 6700 FTIR) was used to characterize the functional moieties of prepared samples. The photocurrent and EIS of the samples were obtained from an electrochemical working station (CHI-760E) in 0.1 M Na_2SO_4 solution. The counter electrode was a Pt wire, and the reference electrode was an Ag/AgCl electrode. The working electrodes were prepared as follow: 7 mg of samples and 0.7 mL ethanol were mixed in 5 mL cuvettes; after that, the cuvettes were sonicated for 4 h to disperse the samples in the solvent homogeneously; then the suspension was evenly coated on ITO glasses (5 × 2 cm) and dried in air for 12 h. When testing photocurrent, the light was provided by a 300 W Xenon lamp (HSX-F300, Beijing NBET Technology Co., Ltd) and its intensity was 600 mW/cm^2, and no voltage was used. EIS was tested in the frequency from 0.01 to 1 × 10^5 Hz the initial voltage was 0.5 V and the amplitude was 0.005 V.

7.2.3 Evaluation of photocatalytic nitrate reduction

The photocatalytic nitrate reduction performance was carried out with a self-made quartz reactor under simulated sunlight irradiation. During the reaction process, the light intensity was 600 mW/cm^2 (HSX-F300) and it was measured by a radiometer. The distance between the light and the reactor was 10 cm. Firstly, 20 mg of the samples were weighed and put into the reactor. Then 100 mL of $NaNO_3$ (20 mg/L) solution was added. Before the reaction, argon was purged into the solution to remove air. After 2-h strong stir to make the powder catalysts uniformly dispersed in the solution, the light was turned on and the light irradiation lasted 4 h. In each hour, 3 mL of liquid was sampled from the reactor. The concentration of ammonium was measured by UV-vis spectrometer using Nessler's reagent method and was further verified by 1H-Nuclear magnetic resonance spectroscopy (NMR) analysis. The concentration of NO_3^- and NO_2^- were measure by a high-pressure integrated capillary anion chromatography.

7.2.4 DFT calculation

In this study, the calculations were carried out utilizing the DFT within the generalized-gradient approximation (GGA) with the exchange-correlation functional of Perdew-Burke-Ernzerhof (PBE). It has been implemented in the Vienna Ab Initio Simulation Package (VASP), which spans reciprocal space with a plane-wave basis and uses the projector-augmented wave (PAW) method (Kresse & Furthmüller 1996b). For the plane-wave basis set, a cutoff energy of 500 eV was used. The total energy was converged to 10^{-4} eV and the residual forces on atoms were below 0.01 eV Å^{-1}.The valence configurations including valence and semicore electrons for Bi and O are

$6s^2 6p^3$ and $2s^2 2p^4$, respectively.

7.3 Results and discussion

7.3.1 Morphology and structure

Firstly, XRD patterns of the samples prepared were measured to study the components of them. As shown in **Figure 7.1a**, the samples prepared under different temperature have different components. The samples BiO-120 and BiO-140 mainly contain α-Bi_2O_3 (COD 1010004). When the temperature reached 160 °C, the characteristic peak of metallic bismuth (COD 9008576) appeared. The XRD patterns of Bi increased when the temperature was 180 °C. During the hydrothermal reaction of $Bi(NO_3)_3 \cdot 5H_2O$ in ethylene glycol solution, the product was mainly α-Bi_2O_3 when the temperature was 120-140 °C. When the temperature was higher than 160 °C, metallic Bi can be generated, which was caused by the reducibility of ethylene glycol. **Figure 1b** showed the crystal structure of α-Bi_2O_3 and metallic Bi. The α-Bi_2O_3 belongs to the P 1 21/c 1 space group (a = 5.83 Å, b = 8.14 Å, c = 7.48 Å), and bismuth belongs to R -3 m: R group (a = b = c = 4.7459 Å). Then XPS was used to further study the components of the samples. In the narrow Bi spectra of BiO-120 (**Figure 1c**), two peaks at 166.8 and 161.6 eV were attributed to the Bi^{3+} of α-Bi_2O_3. While in the spectra of BiO-160, the two peaks of Bi were located at 164.4 and 159.8 eV, indicating the valance state change of Bi^{3+} to Bi^0. In the narrow spectra of O, BiO-120 had a peak at 533.0 eV and it was attributed to the Bi-O bonds in α-Bi_2O_3. BiO-160 showed two peaks in the narrow O spectra. The peak at 531.5 is attributed to the Bi-O bonds in α-Bi_2O_3, and it got a shift to lower binding energy because of the interaction between Bi and α-Bi_2O_3. Notably, a

new peak appeared at 535.1 eV, which can be assigned to C-O bonds (Myers et al. 2018). It means that BiO-160 also contain some carbon from the decomposition of ethylene glycol.

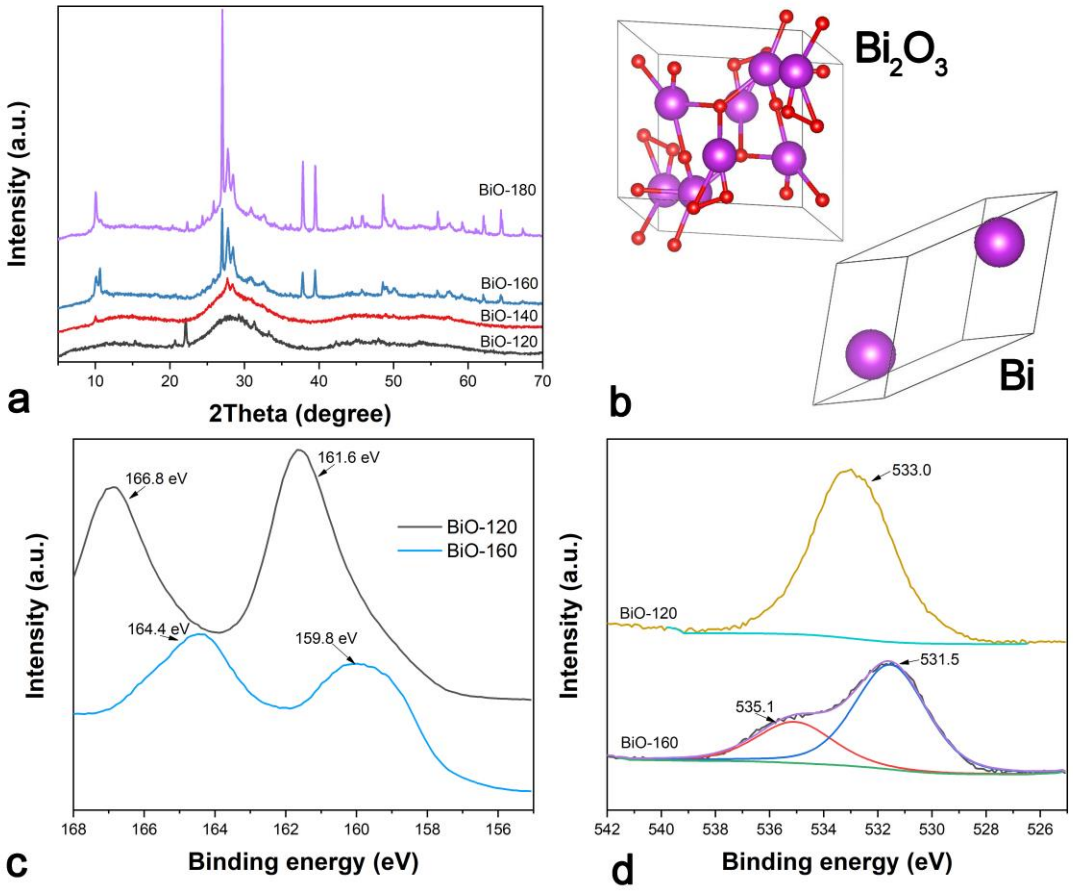

Figure 7.1 (a) The XRD patterns of prepared bismuth/bismuth oxide samples. (b) The crystal structure of Bi_2O_3 and metallic bismuth. (c) The narrow XPS spectra of Bi of BiO-120 and BiO-160. (d) The narrow XPS spectra of O of BiO-120 and BiO-160.

Then we used SEM and TEM to reveal the morphology and structure of the samples. **Figure 7.2a** and **b** are the SEM images of BiO-120 and BiO-160. They were both in sphere structure with a diameter of about 150 nm. Compared with BiO-120, the spheres of BiO-160 are more regular because the higher preparation temperature is beneficial to the growth of crystals. The TEM image of BiO-120 can further confirm its sphere

morphology and size (**Figure 7.2c**). Since BiO-120 is composed of amorphous α-Bi_2O_3, it had no lattice fringes (**Figure 7.2d**). In contrast, BiO-160 had apparent lattice fringes of 0.327 nm, which is contributed to the (012) plane of metallic Bi (**Figure 7.2e**) (Zhang, Sun, et al. 2019). **Figure 7.2f** is the HADDF image of BiO-160, which had a sphere structure matching the SEM results. Then EDS-mapping was employed to further confirm the components of BiO-160. It can be seen that C, O and Bi are uniformly distributed in the BiO-160 spheres, which fit the XRD and XPS results.

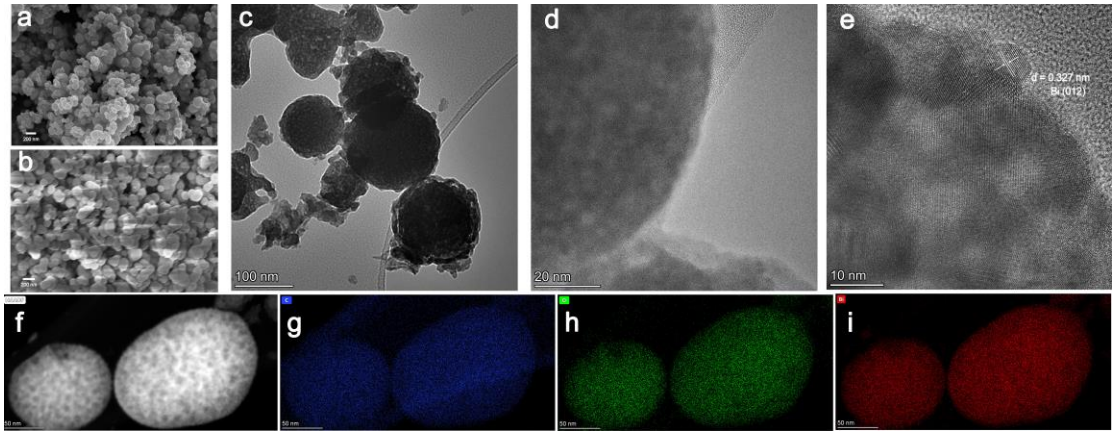

Figure 7.2 The SEM images of BiO-120 (a) and BiO-160 (b). The TEM images of BiO-120 (c, d) and BiO-160 (e). The HADDF TEM image of BiO-160 (f) and EDS mapping of C (g), O (h) and Bi (i) of BiO-160.

Herein, sodium nitrate was used as the nitrogen source for the photocatalytic synthesis of ammonia by prepared samples. As shown in **Figure 7.3a**, under simulated solar light irradiation, the ammonia concentration gradually increased as time went by. Among the samples, BiO-160 showed the highest photocatalytic activity, which had an NH_3 yield of 6.43 mg/h/g_{cat}, and it is 3.65-fold as that of BiO-120 (**Figure 7.3b**). Then we studied the cycle stability of BiO-160. After 4-time usage, the ammonia yield can be 5.67 mg/h/g_{cat} (**Figure 7.3c**), which was 88.18% as the fresh sample, indicating good

stability for reusage. In order to further confirm the ammonia is from the decomposition and reaction of nitrate, isotope-labelled sodium nitrate ($Na^{15}NO_3$) was used as the nitrogen source for photocatalytic ammonia synthesis. As shown in **Figure 7.3d**, the photocatalytic production had two NMR peaks with a coupling constant of 73.1 Hz, which matched the NMR spectra of $^{15}NH_4Cl$ well. The calculated NH_3 concentration produced by the photoreduction of $Na^{15}NO_3$ in 4 h was 5.23 mg/L (similar to the UV-Vis spectrophotometry results in **Figure 7.3a**).

7.3.2 Photocatalytic activity and selectivity

In the nitrate reduction process, nitrate is firstly converted to NO_2^-, followed by a further reduction to ammonia or other products. If the reduction of NO_2^- is not complete, the rest NO_2^- will be more dangerous as NO_2^- is more toxic than NO_3^-. Thus the reaction selectivity of NO_3^- reduction is of great significance. Herein, we calculated the NO_3^- reduction selectivity by BiO-120 and BiO-160. As shown in **Figure 7.3e** and **g**, BiO-120 can remove 39.37% of NO_3^- in 4-h simulated solar light irradiation, and the NH_3 selectivity is 65.21%, the selectivity towards NO_2^- is 28.2%. In the same condition, BiO-160 eliminated 98.72% of NO_3^- (**Figure. 7.3f**), and the main product is NH_3 (95.00%). The selectivity of NO_2^- by BiO-160 in 4 h was 4.47% (**Figure. 7.3h**). If the reaction time is expanded, the rest small amount of NO_2^- can be totally eliminated.

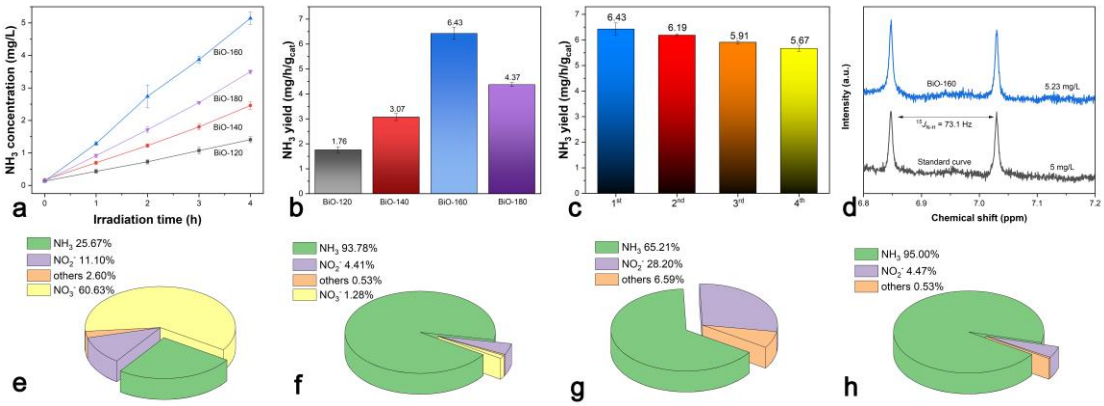

Figure 7.3 (a) The ammonia concentration in the photocatalytic reaction system with time went by. (b) The ammonia yield of prepared samples. (c) The cycle stability of BiO-160 used for 4-time nitrate reduction. (d) The NMR spectra of $^{15}NH_4^+$ standard solution and the final photoreduction production of $^{15}NO_3^-$ by BiO-160. The proportions of productions and NO_3^- after photocatalytic reaction by (e) BiO-120 and (f) BiO-160. The selectivity of photocatalytic reduction of NO_3^- by (g) BiO-120 and (h) BiO-160.

7.3.3 Mechanisms

The band structure properties and electrochemical characterizations were carried out to reveal the mechanisms for the improvement of photocatalytic activity. **Figure 7.4a** is the band structure of α-Bi_2O_3 obtained by DFT calculation, which had an indirect bandgap of 2.59 eV. Then we used UV-vis DRS to study the light absorption property of prepared samples (**Figure 7.4b**). BiO-120 had an absorption edge at 362 nm, indicating it has a bandgap of 3.43 eV. With the preparation temperature increased, the sphere size increased and metallic bismuth and carbon were formed, leading to the redshift of absorption edge and the enhanced broad absorption in visible-light range. The enhanced solar energy absorption can increase the solar energy utilization efficiency, which is crucial for photocatalysis. After that, the photocurrent and EIS were measured to compare the separation and migration of photogenerated charge carriers. As displayed in **Figure 7.4c**, all the samples can rapidly generate photocurrent when

the light was turned on and the photocurrent decreased immediately when the light was turned off. Among all the sample, BiO-160 showed the highest photocurrent with an average value of 0.22 μA, which is about 2.93-fold as that of BiO-120. The photocurrent results illustrate that BiO-160 can generate the highest amount of electrons, which is crucial for photocatalytic NO_3^- reduction. The smaller arc radius of the EIS Nyquies plots of semiconductors usually refect a better conductivity. **Figure 7.4d** showed the EIS Nyquies plots of prepared samples. The sample BiO-120 had the largest arc radius of the EIS Nyquies plots, and the arc radius gradually decreased with the preparation temperature increased. Although BiO-160 had better photocatalytic activity than BiO-180, the arc radius of the EIS Nyquies plots of BiO-180 is smaller than that of BiO-160, the reason is it contains more metallic bismuth and carbon, which can contribute to the better conductivity. The specific surface area is an important property for catalysts. Herein, we measured the surface area of BiO-120 and BiO-160. The surface area of BiO-120 was 6.162 m^2/g and it was 5.064 m^2/g for BiO-160. The surface area decreased with the preparation temperature increased, which was probably caused by the growth of crystals. In this study, the surface area is not the key fact that influence the photocatalytic activity.

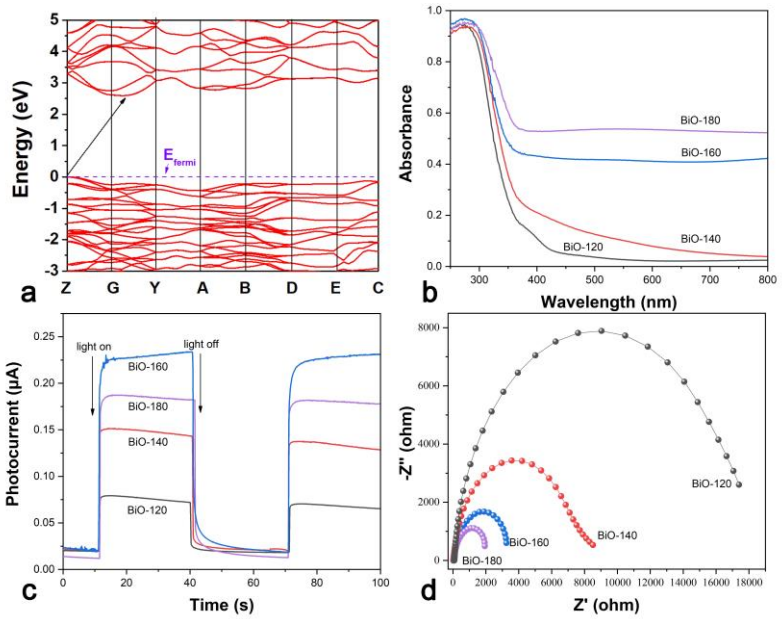

Figure 7.4 (a) The DFT calculated band structure of Bi_2O_3. (b) The UV-vis DRS spectra of prepared bismuth/bismuth oxide samples. (c) The photocurrent response of prepared samples with the light on and off. (d) The EIS Nyquist plots of prepared-sample electrodes in the dark.

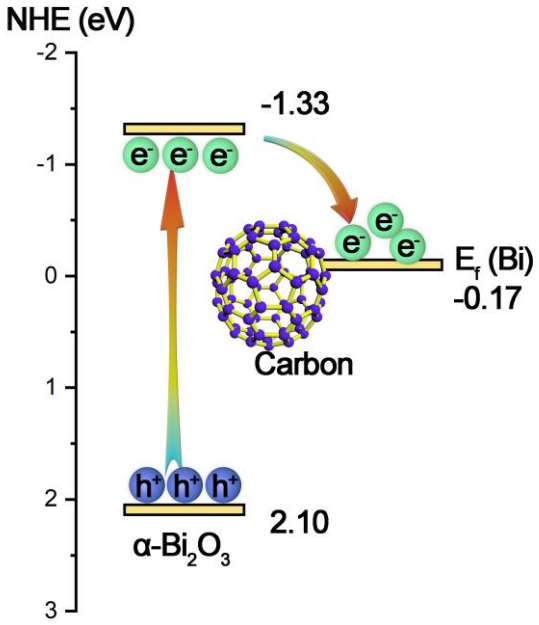

Figure 7.5 The band structure and possible separation pathways of photogenerated charge carriers for enhanced photocatalytic activity.

Depend on the above experimental results, the mechanisms for the exact materials formation and enhanced photocatalytic activity are proposed (**Figure7.5**). When the preparation temperature was 120-140 °C, $Bi(NO_3)_3 \cdot 5H_2O$ intended to be converted to

α-Bi_2O_3 in ethylene glycol solution in the autoclave. When the temperature increased to 160 °C, ethylene glycol can be decomposed, generating some carbon to the α-Bi_2O_3. Besides, the alcoholic hydroxyl of ethylene glycol can reduce some Bi^{3+}, leading to the formation of metallic Bi.

The VB of α-Bi_2O_3 is chiefly contributed by the O 2*p* and Bi 6*s* orbitals, and its CB is contributed by the Bi 6*p* orbitals (Sharma et al. 2017). The VB and CB of α-Bi_2O_3 were located at 2.10 and -1.33 eV (vs. NHE), respectively (Guo et al. 2018). The Fermi energy of metallic Bi is at -0.17 eV (Hao, Wang, et al. 2017). Under simulated solar light irradiation, electrons on the VB of α-Bi_2O_3 are excited and they will transfer to the CB of α-Bi_2O_3. At the same time, abundant electrons can be generated on metallic Bi due to its surface plasma effect. Since the Fermi energy of metallic Bi is closed to the CB of α-Bi_2O_3, the photogenerated electrons on α-Bi_2O_3 can be accumulated on the Fermi level of Bi, rather than recombination with holes. Besides, the carbon from the decomposition of ethylene glycol can improve the conductivity of the composite materials, which is beneficial to the migration of electrons. As a result, the separation of photogenerated electron-hole pairs can be significantly boosted, leading to the remarkable photocatalytic activity for nitrate reduction to ammonia.

7.4 Conclusion

In this work, a facile synthesis of carbon/bismuth/bismuth oxide was reported, which showed remarkable performance of photocatalytic reduction of nitrate to ammonia. Compared with α-Bi_2O_3, the photocatalytic ammonia yield of the optimum sample

increased 3.65 times. Besides, the ammonia selectivity increased from 65.21% to 95.00%. The highly boosted photochemical performance was associate with the surface plasma effect of metallic bismuth. Meanwhile, the formation of carbon enables to boost the transfer of electrons. Under light irradiation, electrons can be accumulated on metallic bismuth, boosting the reduction of nitrate. The results of this work may contribute to the research of novel plasma bismuth-based materials and the study of photocatalytic nitrate reduction.

Chapter 8 Conclusions and recommendations

8.1 Conclusions

In this thesis, several strategies and novel nanomaterials were invented to achieved highly efficient artificial ammonia synthesis under ambient conditions, including nanostructure control, metal modification, small π-conjugated molecule modification, plasma modification.

We reported a novel synthesis of 1D defective g-C_3N_4 nanorods by the facial treatment of precursors. The defects of the catalysts can help to adsorb, activate and cleave the N_2 molecules. Besides, the bandgap was narrowed, leading to higher utilization of solar energy and rapider separation of charge carriers. The formed 1D structure can also boost the transfer and separation of electron-hole pairs. Compared with bulk g-C_3N_4, the photocatalytic N_2 reduction rate of defective g-C_3N_4 nanorods was increased by 3.66 times.

A novel BiOBr-TCNQ photocatalyst was prepared via a facile self-assembly method. Due to the well-match band structure of TCNQ and BiOBr, the separation and transfer of photogenerated electron-hole pairs were significantly boosted. More importantly, the abundant delocalized π electrons of TCNQ, and the strong electron-withdrawing property of TNCQ made electrons efficiently accumulated on the surface of catalysts, leading to a remarkable photocatalytic activity. Compared with the pristine BiOBr, the optimized BiOBr-TCNQ sample showed a 5.6-fold photocatalytic N_2 reduction activity.

We used a facile and green approach to synthesize novel metallic Ru modified g-C_3N_4 nanosheets as photocatalysts for enhanced NO_3^- reduction to NH_3. The optimal sample (CN-Ru-1) had the highest NH_3 yield rate of 2.627 mg/h/g_{cat} and it was 2.93 times as that of bulk CN. After 4-hour light irradiation, CN-Ru-1 eliminated 92.85% of NO_3^- and the NH_3 selectivity was 77.9%. After four cycles, the sample still had good photocatalytic performance (88.16% as the fresh catalyst). NMR and ^{15}N isotope labelling provided solid evidence that the N of NH_3 was from the reduction of NO_3^-. The g-C_3N_4 nanosheets modified by metallic Ru particles have stronger light absorption, better conductivity and more rapid separation of electron-hole pairs. With the enhanced adsorption energy of NO_3^- and the low thermodynamic energy barriers, the photocatalytic activity and selectivity were increased significantly.

A facile synthesis of carbon/bismuth/bismuth oxide was reported, which showed remarkable performance of photocatalytic reduction of nitrate to ammonia. Compared with α-Bi_2O_3, the photocatalytic ammonia yield of the optimum sample increased 3.65 times. Besides, the ammonia selectivity increased from 65.21% to 95.00%. The highly enhanced photocatalytic performance was attributed to the surface plasma effect of metallic bismuth. Meanwhile, the formation of carbon enables to boost the transfer of electrons. Under light irradiation, electrons can be accumulated on metallic bismuth, boosting the reduction of nitrate. The results of these series may contribute to the research of novel plasma bismuth-based materials and the study of photocatalytic nitrate reduction.

Herein, we found the nanostructure control, metal modification, small π-conjugated molecule modification, plasma modification can all significantly improve the photochemical artificial ammonia synthesis efficiency. The experimental approaches and mechanisms were detailed studied. The research outcomes may contribute to the knowledge of psychical chemistry, materials chemistry, nanotechnology and environmental engineering.

8.2 Recommendations

Currently, researches on photocatalytic ammonia synthesis are mainly focused on preparing highly efficient powder catalysts for nitrogen fixation. Beyond it, here are some interesting aspects with broad application prospects.

(1) Looking for ionic liquid or some other solutes that have good solubility of nitrogen, since the poor solubility significantly limits the nitrogen fixation reaction.

(2) Besides nitrogen reduction, researchers should pay more attention to the synthesis of ammonia using other nitrogen-based wastes like nitrate, nitrite, nitrogen oxides etc., because converting these wastes to resource is more sustainable and eco-friendly than nitrogen fixation.

(3) Combining nitrogen cycle with other redox reactions like CO_2 reduction etc. enable to be used to synthesize other high-value chemicals, which is of higher significance.

(4) To be mass applied for artificial ammonia synthesis, strategies should be developed to solve the cycle problems of powder photocatalysts.

(5) Combining microbial reactors with photocatalytic reactions can significantly increase the efficiency and it has wide prospect.

Reference

Ahada, C.P. & Suthar, S. 2018, 'Groundwater nitrate contamination and associated human health risk assessment in southern districts of Punjab, India', *Environmental science and pollution research*, vol. 25, no. 25, pp. 25336-47.

Alshammari, A. & Jiang, Z. 2016, 'KE Cordova in Semiconductor Photocatalysis-Materials, Mechanisms and Applications', *InTech, Rijeka, Croatia*.

Alshammari, A., Jiang, Z. & Cordova, K.E. 2016, 'Metal organic frameworks as emerging photocatalysts', *Semiconductor Photocatalysis: Materials, Mechanisms and Applications*, pp. 302-41.

Azofra, L.M., Li, N., MacFarlane, D.R. & Sun, C. 2016, 'Promising prospects for 2D d^2–d^4 M $_3C_2$ transition metal carbides (MXenes) in N_2 capture and conversion into ammonia', *Energy & Environmental Science*, vol. 9, no. 8, pp. 2545-9.

Baek, K., Jeon, W.C., Woo, S., Kim, J.C., Lee, J.G., An, K., Kwak, S.K. & Kang, S.J. 2020, 'Synergistic effect of quinary molten salts and ruthenium catalyst for high-power-density lithium-carbon dioxide cell', *Nature communications*, vol. 11, no. 1, pp. 1-9.

Bai, S., Zhang, N., Gao, C. & Xiong, Y. 2018, 'Defect engineering in photocatalytic materials', *Nano Energy*, vol. 53, pp. 296-336.

Bai, X., Wang, X., Lu, X., Liang, Y., Li, J., Wu, L., Li, H., Hao, Q., Ni, B.-J. & Wang, C. 2020, 'Surface defective g-C_3N_4-xCl_x with unique spongy structure by polarization effect for enhanced photocatalytic removal of organic pollutants', *Journal of Hazardous Materials*, vol. 398, p. 122897.

Bai, X.J., Yan, S.C., Wang, J.J., Wang, L., Jiang, W.J., Wu, S.L., Sun, C.P. & Zhu, Y.F. 2014, 'A simple and efficient strategy for the synthesis of a chemically tailored g-C_3N_4 material', *Journal of Materials Chemistry A*, vol. 2, no. 41, pp. 17521-9.

Bai, Y., Ye, L.Q., Chen, T., Wang, L., Shi, X., Zhang, X. & Chen, D. 2016, 'Facet-Dependent Photocatalytic N_2 Fixation of Bismuth-Rich Bi_5O_7I Nanosheets', *ACS Applied Materials & Interfaces*, vol. 8, no. 41, pp. 27661-8.

Bennett, T.H., Pamu, R., Yang, G., Mukherjee, D. & Khomami, B. 2020, 'A new platform for development of photosystem I based thin films with superior photocurrent: TCNQ charge transfer salts derived from ZIF-8', *Nanoscale Advances*, vol. 2, no. 11, pp. 5171-80.

Bhadu, G.R., Chaudhari, J.C., Rebary, B., Patidar, R. & Srivastava, D.N. 2018, 'Correlating growth mechanism and morphology in Cu-TCNQ organometallic complex: A microscopic study', *Micron*, vol. 107, pp. 85-93.

Bi, Y., Wang, Y., Dong, X., Zheng, N., Ma, H. & Zhang, X. 2018, 'Efficient solar-driven conversion of nitrogen to ammonia in pure water via hydrogenated bismuth

oxybromide', *RSC advances*, vol. 8, no. 39, pp. 21871-8.

Blöchl, P.E. 1994, 'Projector augmented-wave method', *Physical review B*, vol. 50, no. 24, p. 17953.

Cao, L., Luo, Q., Chen, J., Wang, L., Lin, Y., Wang, H., Liu, X., Shen, X., Zhang, W. & Liu, W. 2019, 'Dynamic oxygen adsorption on single-atomic Ruthenium catalyst with high performance for acidic oxygen evolution reaction', *Nature Communications*, vol. 10, no. 1, pp. 1-9.

Cao, S.W., Low, J.X., Yu, J.G. & Jaroniec, M. 2015, 'Polymeric Photocatalysts Based on Graphitic Carbon Nitride', *Advanced Materials*, vol. 27, no. 13, pp. 2150-76.

Chen, L.-W., Hao, Y.-C., Guo, Y., Zhang, Q., Li, J., Gao, W.-Y., Ren, L., Su, X., Hu, L. & Zhang, N. 2021, 'Metal–Organic Framework Membranes Encapsulating Gold Nanoparticles for Direct Plasmonic Photocatalytic Nitrogen Fixation', *Journal of the American Chemical Society*, vol. 143, no. 15, pp. 5727-36.

Chen, T., Hao, Q., Yang, W.J., Xie, C.L., Chen, D.M., Ma, C., Yao, W.Q. & Zhu, Y.F. 2018, 'A honeycomb multilevel structure Bi_2O_3 with highly efficient catalytic activity driven by bias voltage and oxygen defect', *Applied Catalysis B-Environmental*, vol. 237, pp. 442-8.

Chen, X., Zhang, X., Li, Y.-H., Qi, M.-Y., Li, J.-Y., Tang, Z.-R., Zhou, Z. & Xu, Y.-J. 2021, 'Transition metal doping BiOBr nanosheets with oxygen vacancy and exposed {102} facets for visible light nitrogen fixation', *Applied Catalysis B: Environmental*, vol. 281, p. 119516.

Choi, H., Peters, A.W., Noh, H., Gallington, L.C., Platero-Prats, A.E., DeStefano, M.R., Rimoldi, M., Goswami, S., Chapman, K.W., Farha, O.K. & Hupp, J.T. 2019, 'Vapor-Phase Fabrication and Condensed-Phase Application of a MOF-Node-Supported Iron Thiolate Photocatalyst for Nitrate Conversion to Ammonium', *ACS Applied Energy Materials*, vol. 2, no. 12, pp. 8695-700.

Comer, B.M. & Medford, A.J. 2018, 'Analysis of Photocatalytic Nitrogen Fixation on Rutile TiO2(110)', *Acs Sustainable Chemistry & Engineering*, vol. 6, no. 4, pp. 4648-60.

Cooper, J.K., Gul, S., Toma, F.M., Chen, L., Glans, P.A., Guo, J.H., Ager, J.W., Yano, J. & Sharp, I.D. 2014, 'Electronic Structure of Monoclinic $BiVO_4$', *Chemistry of Materials*, vol. 26, no. 18, pp. 5365-73.

Council, N.R. 2004, 'Committee on Alternatives and Strategies for Future Hydrogen Production and Use', *The Hydrogen Economy: Opportunities, Costs, Barriesr, and R&D Needs*.

Cucka, P. & Barrett, C. 1962, 'The crystal structure of Bi and of solid solutions of Pb, Sn, Sb and Te in Bi', *Acta Crystallographica*, vol. 15, no. 9, pp. 865-72.

Dai, Z., Qin, F., Zhao, H.P., Ding, J., Liu, Y.L. & Chen, R. 2016, 'Crystal Defect Engineering of Aurivillius Bi_2MoO_6 by Ce Doping for Increased Reactive Species Production in Photocatalysis', *ACS Catalysis*, vol. 6, no. 5, pp. 3180-92.

Di, J., Xia, J., Chisholm, M.F., Zhong, J., Chen, C., Cao, X., Dong, F., Chi, Z., Chen, H., Weng, Y.-X., Xiong, J., Yang, S.-Z., Li, H., Liu, Z. & Dai, S. 2019, 'Defect-Tailoring Mediated Electron-Hole Separation in Single-Unit-Cell Bi_3O_4 Br Nanosheets for Boosting Photocatalytic Hydrogen Evolution and Nitrogen Fixation', *Advanced Materials,* vol. 31, no 28, p. e1807576.

Dong, F., Xiong, T., Sun, Y.J., Zhao, Z.W., Zhou, Y., Feng, X. & Wu, Z.B. 2014, 'A semimetal

bismuth element as a direct plasmonic photocatalyst', *Chemical Communications*, vol. 50, no. 72, pp. 10386-9.

Dong, F., Zhao, Z., Sun, Y., Zhang, Y., Yan, S. & Wu, Z. 2015, 'An Advanced Semimetal-Organic Bi Spheres-g-C_3N_4 Nanohybrid with SPR-Enhanced Visible-Light Photocatalytic Performance for NO Purification', *Environmental Science & Technology*, vol. 49, no. 20, pp. 12432-40.

Du, Y., Hao, Q., Chen, D., Chen, T., Hao, S., Yang, J., Ding, H., Yao, W. & Song, J. 2017, 'Facile fabrication of heterostructured bismuth titanate nanocomposites: The effects of composition and band gap structure on the photocatalytic activity performance', *Catalysis Today*, vol. 297, pp. 255-63.

Elcheikh Mahmoud, M., Audi, H., Assoud, A., Ghaddar, T.H. & Hmadeh, M. 2019, 'Metal–Organic Framework Photocatalyst Incorporating Bis (4′-(4-carboxyphenyl)-terpyridine) ruthenium (II) for Visible-Light-Driven Carbon Dioxide Reduction', *Journal of the American Chemical Society*, vol. 141, no. 17, pp. 7115-21.

Elmidaoui, A., Elhannouni, F., Sahli, M.M., Chay, L., Elabbassi, H., Hafsi, M. & Largeteau, D. 2001, 'Pollution of nitrate in Moroccan ground water: removal by electrodialysis', *Desalination*, vol. 136, no. 1-3, pp. 325-32.

Erisman, J.W., Sutton, M.A., Galloway, J., Klimont, Z. & Winiwarter, W. 2008, 'How a century of ammonia synthesis changed the world', *Nature Geoscience*, vol. 1, no. 10, pp. 636-9.

Fernández-Nava, Y., Maranon, E., Soons, J. & Castrillón, L. 2008, 'Denitrification of wastewater containing high nitrate and calcium concentrations', *Bioresource Technology*, vol. 99, no. 17, pp. 7976-81.

Franklin, E.C. 1922, 'The ammono carbonic acids', *Journal of the American Chemical Society*, vol. 44, pp. 486-509.

Freire, J.M., Matos, M.A., Abreu, D.S., Becker, H., Diogenes, I.C., Valentini, A. & Longhinotti, E. 2020, 'Nitrate photocatalytic reduction on TiO_2: metal loaded, synthesis and anions effect', *Journal of Environmental Chemical Engineering*, vol. 8, no. 4, p. 103844.

Fu, J.W., Xu, Q.L., Low, J.X., Jiang, C.J. & Yu, J.G. 2019, 'Ultrathin 2D/2D WO_3/g-C_3N_4 step-scheme H_2 production photocatalyst', *Applied Catalysis B-Environmental*, vol. 243, pp. 556-65.

Fujishima, A. & Honda, K. 1972, 'Electrochemical photolysis of water at a semiconductor electrode', *Nature*, vol. 238, no. 5358, pp. 37-8.

Gao, H., Cao, R., Xu, X., Zhang, S., Yongshun, H., Yang, H., Deng, X. & Li, J. 2019, 'Construction of dual defect mediated Z-scheme photocatalysts for enhanced photocatalytic hydrogen evolution', *Applied Catalysis B: Environmental*, vol. 245, pp. 399-409.

Gao, H., Cao, R., Zhang, S., Yang, H. & Xu, X. 2018, 'Three-dimensional hierarchical g-C_3N_4 architectures assembled by ultrathin self-doped nanosheets: extremely facile hexamethylenetetramine activation and superior photocatalytic hydrogen evolution', *ACS applied materials & interfaces*, vol. 11, no. 2, pp. 2050-9.

Gao, X.M., Shang, Y.Y., Liu, L.B. & Fu, F. 2019a, 'Chemisorption-enhanced photocatalytic nitrogen fixation via 2D ultrathin p-n heterojunction AgCl/delta-Bi_2O_3 nanosheets', *Journal of Catalysis*, vol. 371, pp. 71-80.

Gao, X.M., Shang, Y.Y., Liu, L.B. & Fu, F. 2019b, 'Multilayer ultrathin Ag-delta-Bi_2O_3 with ultrafast charge transformation for enhanced photocatalytic nitrogen fixation', *Journal of Colloid and Interface Science*, vol. 533, pp. 649-57.

Garcia-Segura, S., Lanzarini-Lopes, M., Hristovski, K. & Westerhoff, P. 2018, 'Electrocatalytic reduction of nitrate: Fundamentals to full-scale water treatment applications', *Applied Catalysis B-Environmental*, vol. 236, pp. 546-68.

Geng, Z., Chen, Z., Li, Z., Qi, X., Yang, X., Fan, W., Guo, Y., Zhang, L. & Huo, M. 2018, 'Enhanced photocatalytic conversion and selectivity of nitrate reduction to nitrogen over AgCl/TiO_2 nanotubes', *Dalton Transactions*, vol. 47, no. 32, pp. 11104-12.

Giddey, S., Badwal, S.P.S. & Kulkarni, A. 2013, 'Review of electrochemical ammonia production technologies and materials', *International Journal of Hydrogen Energy*, vol. 38, no. 34, pp. 14576-94.

Greeley, J., Jaramillo, T.F., Bonde, J., Chorkendorff, I.B. & Norskov, J.K. 2006, 'Computational high-throughput screening of electrocatalytic materials for hydrogen evolution', *Nature Materials*, vol. 5, no. 11, pp. 909-13.

Guo, J.-g., Liu, Y., Hao, Y.-j., Li, Y.-l., Wang, X.-j., Liu, R.-h. & Li, F.-t. 2018, 'Comparison of importance between separation efficiency and valence band position: The case of heterostructured Bi_3O_4Br/α-Bi_2O_3 photocatalysts', *Applied Catalysis B: Environmental*, vol. 224, pp. 841-53.

Guo, W.H., Zhang, K.X., Liang, Z.B., Zou, R.Q. & Xu, Q. 2019, 'Electrochemical nitrogen fixation and utilization: theories, advanced catalyst materials and system design', *Chemical Society Reviews*, vol. 48, no. 24, pp. 5658-716.

Gupta, G., Kaur, A., Sinha, A. & Kansal, S.K. 2017, 'Photocatalytic degradation of levofloxacin in aqueous phase using Ag/AgBr/BiOBr microplates under visible light', *Materials Research Bulletin*, vol. 88, pp. 148-55.

Han, N., Wang, Y., Yang, H., Deng, J., Wu, J.H., Li, Y.F. & Li, Y.G. 2018, 'Ultrathin bismuth nanosheets from in situ topotactic transformation for selective electrocatalytic CO_2 reduction to formate', *Nature Communications*, vol. 9, p. 8.

Hao, C., Liao, Y., Wu, Y., An, Y., Lin, J., Gu, Z., Jiang, M., Hu, S. & Wang, X. 2020, 'RuO2-loaded TiO_2-MXene as a high performance photocatalyst for nitrogen fixation', *Journal of Physics and Chemistry of Solids*, vol. 136. p. 109141.

Hao, Q., Chen, T., Wang, R.T., Feng, J.R., Chen, D.M. & Yao, W.Q. 2018b, 'A separation-free polyacrylamide/bentonite/graphitic carbon nitride hydrogel with excellent performance in water treatment', *Journal of Cleaner Production*, vol. 197, pp. 1222-30.

Hao, Q., Hao, S.M., Niu, X.X., Li, X., Chen, D.M. & Ding, H. 2017, 'Enhanced photochemical oxidation ability of carbon nitride by pi-pi stacking interactions with graphene', *Chinese Journal of Catalysis*, vol. 38, no. 2, pp. 278-86.

Hao, Q., Niu, X.X., Nie, C.S., Hao, S.M., Zou, W., Ge, J.M., Chen, D.M. & Yao, W.Q. 2016, 'A highly efficient g-C_3N_4/SiO_2 heterojunction: the role of SiO_2 in the enhancement of visible light photocatalytic activity', *Physical Chemistry Chemical Physics*, vol. 18, no. 46, pp. 31410-8.

Hao, Q., Wang, R., Lu, H., Xie, C.a., Ao, W., Chen, D., Ma, C., Yao, W. & Zhu, Y. 2017, 'One-pot synthesis of C/Bi/Bi_2O_3 composite with enhanced photocatalytic activity', *Applied Catalysis B-Environmental*, vol. 219, pp. 63-72.

Hao, Y.C., Dong, X.L., Zhai, S.R., Ma, H.C., Wang, X.Y. & Zhang, X.F. 2016, 'Hydrogenated Bismuth Molybdate Nanoframe for Efficient Sunlight-Driven Nitrogen Fixation from Air', *Chemistry-A European Journal*, vol. 22, no. 52, pp. 18722-8.

Hao, Y.C., Guo, Y., Chen, L.W., Shu, M., Wang, X.Y., Bu, T.A., Gao, W.Y., Zhang, N., Su, X., Feng, X., Zhou, J.W., Wang, B., Hu, C.W., Yin, A.X., Si, R., Zhang, Y.W. & Yan, C.H. 2019, 'Promoting nitrogen electroreduction to ammonia with bismuth nanocrystals and potassium cations in water', *Nature Catalysis*, vol. 2, no. 5, pp. 448-56.

Hayat, A., Shaishta, N., Mane, S.K.B., Khan, J. & Hayat, A. 2019, 'Rational Ionothermal copolymerization of TCNQ with PCN semiconductor for enhanced Photocatalytic full water splitting', *ACS applied materials & interfaces*, vol. 11, no. 50, pp. 46756-66.

He, B., He, J., Wang, L., Zhang, X. & Bi, E. 2019, 'Effect of hydrogeological conditions and surface loads on shallow groundwater nitrate pollution in the Shaying River Basin: Based on least squares surface fitting model', *Water research*, vol. 163, p. 114880.

Heidari, S., Haghighi, M. & Shabani, M. 2020, 'Sunlight-activated BiOCl/BiOBr–$Bi_{24}O_{31}Br_{10}$ photocatalyst for the removal of pharmaceutical compounds', *Journal of Cleaner Production*, vol. 259, p. 120679.

Hennessey, S., Farràs, P., Benet-Buchholz, J. & Llobet, A. 2019, 'A Bpp-based dinuclear ruthenium photocatalyst for visible light-driven oxidation reactions', *Catalysis Science & Technology*, vol. 9, no. 23, pp. 6760-8.

Hirakawa, H., Hashimoto, M., Shiraishi, Y. & Hirai, T. 2017, 'Selective Nitrate-to-Ammonia Transformation on Surface Defects of Titanium Dioxide Photocatalysts', *ACS Catalysis*, vol. 7, no. 5, pp. 3713-20.

Hoffman, C.A., Meyer, J.R., Bartoli, F.J., Divenere, A., Yi, X.J., Hou, C.L., Wang, H.C., Ketterson, J.B. & Wong, G.K. 1993, ' Semimetal-to-semiconductor transition in bismuth thin-films', *Physical Review B*, vol. 48, no. 15, pp. 11431-4.

Hong, S.J., Lee, S., Jang, J.S. & Lee, J.S. 2011, 'Heterojunction $BiVO_4/WO_3$ electrodes for enhanced photoactivity of water oxidation', *Energy & Environmental Science*, vol. 4, no. 5, pp. 1781-7.

Hou, Z., Chen, F., Wang, J., François-Xavier, C.P. & Wintgens, T. 2018, 'Novel $Pd/GdCrO_3$ composite for photo-catalytic reduction of nitrate to N_2 with high selectivity and activity', *Applied Catalysis B: Environmental*, vol. 232, pp. 124-34.

Hou, Z., Chu, J., Liu, C., Wang, J., Li, A., Lin, T. & François-Xavier, C.P. 2021, 'High efficient photocatalytic reduction of nitrate to N_2 by Core-shell Ag/SiO_2@ $cTiO_2$ with synergistic effect of light scattering and surface plasmon resonance', *Chemical Engineering Journal*, vol. 415, p. 128863.

Hsieh, S.H., Lee, G.J., Chen, C.Y., Chen, J.H., Ma, S.H., Horng, T.L., Chen, K.H. & Wu, J.J. 2012, 'Synthesis of Pt Doped Bi_2O_3/RuO_2 Photocatalysts for Hydrogen Production from Water Splitting Using Visible Light', *Journal of Nanoscience and Nanotechnology*, vol. 12, no. 7, pp. 5930-6.

Hu, C., Chen, X., Jin, J., Han, Y., Chen, S., Ju, H., Cai, J., Qiu, Y., Gao, C. & Wang, C. 2019, 'Surface plasmon enabling nitrogen fixation in pure water through a dissociative mechanism under mild conditions', *Journal of the American Chemical Society*, vol. 141, no. 19, pp. 7807-14.

Hu, P., Liu, L., An, W., Liang, Y. & Cui, W. 2017, 'Use of a core-shell composite Ag_3PO_4@ TCNQ to improve photocatalytic activity and stability', *Applied Surface Science*, vol. 425, pp. 329-39.

Hua, C., Dong, X., Wang, Y., Zheng, N., Ma, H. & Zhang, X. 2019, 'Bi-modified 3D BiOBr microsphere with oxygen vacancies for efficient visible-light photocatalytic performance', *Journal of Materials Science*, vol. 54, no. 13, pp. 9397-413.

Huang, H., Han, X., Li, X., Wang, S., Chu, P.K. & Zhang, Y. 2015, 'Fabrication of multiple heterojunctions with tunable visible-light-active photocatalytic reactivity in BiOBr–BiOI full-range composites based on microstructure modulation and band structures', *ACS applied materials & interfaces*, vol. 7, no. 1, pp. 482-92.

Huang, W.L. 2009, 'Electronic structures and optical properties of BiOX (X= F, Cl, Br, I) via DFT calculations', *Journal of computational chemistry*, vol. 30, no. 12, pp. 1882-91.

Huang, Y., Zhu, Y., Chen, S., Xie, X., Wu, Z. & Zhang, N. 2021, 'Schottky Junctions with Bi Cocatalyst for Taming Aqueous Phase N_2 Reduction toward Enhanced Solar Ammonia Production', *Advanced Science*, vol. 8, no. 6, p. 2003626.

Huynh, W.U., Dittmer, J.J. & Alivisatos, A.P. 2002, 'Hybrid nanorod-polymer solar cells', *Science*, vol. 295, no. 5564, pp. 2425-7.

Jia, G.H., Sitt, A., Hitin, G.B., Hadar, I., Bekenstein, Y., Amit, Y., Popov, I. & Banin, U. 2014, 'Couples of colloidal semiconductor nanorods formed by self-limited assembly', *Nature Materials*, vol. 13, no. 3, pp. 302-8.

Jiang, W., Zhang, M., Wang, J., Liu, Y. & Zhu, Y. 2014, 'Dramatic visible activity in phenol degradation of TCNQ@ TiO_2 photocatalyst with core–shell structure', *Applied Catalysis B: Environmental*, vol. 160, pp. 44-50.

Kandemir, T., Schuster, M.E., Senyshyn, A., Behrens, M. & Schloegl, R. 2013, 'The Haber-Bosch Process Revisited: On the Real Structure and Stability of "Ammonia Iron" under Working Conditions', *Angewandte Chemie-International Edition*, vol. 52, no. 48, pp. 12723-6.

Kapoor, A. & Viraraghavan, T. 1997, 'Nitrate removal from drinking water', *Journal of environmental engineering*, vol. 123, no. 4, pp. 371-80.

Kehrer, M., Duchoslav, J., Hinterreiter, A., Cobet, M., Mehic, A., Stehrer, T. & Stifter, D. 2019, 'XPS investigation on the reactivity of surface imine groups with TFAA', *Plasma Processes and Polymers*, vol. 16, no. 4, p. 1800160.

Khaniya, A., Ezzat, S., Cumston, Q., Coffey, K.R. & Kaden, W.E. 2020, 'Ru (0001) and SiO_2/Ru (0001): XPS study', *Surface Science Spectra*, vol. 27, no. 2, p. 024009.

Kissel, E. 2014, 'The Historical Development and Significance of the Haber Bosch Process', *Better Crops With Plant Food*, vol. 98, no. 2, p. 31.

Kobayashi, H., Hayakawa, A., Somarathne, K. & Okafor, E.C. 2019, 'Science and technology of ammonia combustion', *Proceedings of the Combustion Institute*, vol. 37, no. 1, pp. 109-33.

Koh, E.-H., Lee, E. & Lee, K.-K. 2020, 'Application of geographically weighted regression models to predict spatial characteristics of nitrate contamination: Implications for an effective groundwater management strategy', *Journal of Environmental Management*, vol. 268, p. 110646.

Kominami, H., Furusho, A., Murakami, S.-y., Inoue, H., Kera, Y. & Ohtani, B. 2001, 'Effective

photocatalytic reduction of nitrate to ammonia in an aqueous suspension of metal-loaded titanium (IV) oxide particles in the presence of oxalic acid', *Catalysis letters*, vol. 76, no. 1-2, pp. 31-4.

Kong, X.Y., Lee, W.P.C., Ong, W.J., Chai, S.P. & Mohamed, A.R. 2016, 'Oxygen-Deficient BiOBr as a Highly Stable Photocatalyst for Efficient CO_2 Reduction into Renewable Carbon-Neutral Fuels', *Chemcatchem*, vol. 8, no. 19, pp. 3074-81.

Kresse, G. & Furthmüller, J. 1996a, 'Efficiency of ab-initio total energy calculations for metals and semiconductors using a plane-wave basis set', *Computational materials science*, vol. 6, no. 1, pp. 15-50.

Kresse, G. & Furthmüller, J. 1996b, 'Efficient iterative schemes for ab initio total-energy calculations using a plane-wave basis set', *Physical review B*, vol. 54, no. 16, p. 11169.

Kresse, G., Furthmüller, J. & Hafner, J. 1994, 'Theory of the crystal structures of selenium and tellurium: the effect of generalized-gradient corrections to the local-density approximation', *Physical Review B*, vol. 50, no. 18, p. 13181.

Kresse, G. & Hafner, J. 1993, 'Ab initio molecular dynamics for liquid metals', *Physical Review B*, vol. 47, no. 1, p. 558.

Kresse, G. & Joubert, D. 1999, 'From ultrasoft pseudopotentials to the projector augmented-wave method', *Physical Review B*, vol. 59, no. 3, pp. 1758-75.

Kroke, E., Schwarz, M., Horath-Bordon, E., Kroll, P., Noll, B. & Norman, A.D. 2002, 'Tri-s-triazine derivatives. Part I. From trichloro-tri-s-triazine to graphitic C_3N_4 structures', *New Journal of Chemistry*, vol. 26, no. 5, pp. 508-12.

Kumar, R., Heße, F., Rao, P., Musolff, A., Jawitz, J., Sarrazin, F., Samaniego, L., Fleckenstein, J., Rakovec, O. & Thober, S. 2020, 'Strong hydroclimatic controls on vulnerability to subsurface nitrate contamination across Europe', *Nature communications*, vol. 11, no. 1, pp. 1-10.

Lan, M., Zheng, N., Dong, X., Ren, X., Wu, J., Ma, H. & Zhang, X. 2021, 'Facile construction of hierarchical Bi@BiOBr-Bi_2MoO_6 ternary heterojunction with abundant oxygen vacancies for excellent photocatalytic nitrogen fixation', *Sustainable Energy & Fuels*.

Lashgari, M. & Zeinalkhani, P. 2017, 'Photocatalytic N_2 conversion to ammonia using efficient nanostructured solar-energy-materials in aqueous media: A novel hydrogenation strategy and basic understanding of the phenomenon', *Applied Catalysis A: General*, vol. 529, pp. 91-7.

Lassaletta, L., Billen, G., Grizzetti, B., Anglade, J. & Garnier, J. 2014, '50 year trends in nitrogen use efficiency of world cropping systems: the relationship between yield and nitrogen input to cropland', *Environmental Research Letters*, vol. 9, no. 10, p. 9.

Leigh, G. 2004a, 'Haber-Bosch and other industrial processes', *Catalysts for nitrogen fixation*, Springer, pp. 33-54.

Leigh, G.J. 2004b, 'Haber-Bosch and other industrial processes', *Catalysts for Nitrogen Fixation: Nitrogenases, Relevant Chemical Models and Commercial Processes*, pp. 33-54.

Lemaignen, L., Tong, C., Begon, V., Burch, R. & Chadwick, D. 2002, 'Catalytic denitrification of water with palladium-based catalysts supported on activated carbons', *Catalysis Today*, vol. 75, no. 1-4, pp. 43-8.

Li, H., Shang, J., Ai, Z.H. & Zhang, L.Z. 2015, 'Efficient Visible Light Nitrogen Fixation with

BiOBr Nanosheets of Oxygen Vacancies on the Exposed {001} Facets', *Journal of the American Chemical Society*, vol. 137, no. 19, pp. 6393-9.

Li, H., Shang, J., Shi, J.G., Zhao, K. & Zhang, L.Z. 2016, 'Facet-dependent solar ammonia synthesis of BiOCl nanosheets via a proton-assisted electron transfer pathway', *Nanoscale*, vol. 8, no. 4, pp. 1986-93.

Li, H.P., Liu, J.Y., Hou, W.G., Du, N., Zhang, R.J. & Tao, X.T. 2014, 'Synthesis and characterization of g-C_3N_4/Bi_2MoO_6 heterojunctions with enhanced visible light photocatalytic activity', *Applied Catalysis B-Environmental*, vol. 160, pp. 89-97.

Li, J., Li, H., Zhan, G.M. & Zhang, L.Z. 2017, 'Solar Water Splitting and Nitrogen Fixation with Layered Bismuth Oxyhalides', *Accounts of Chemical Research*, vol. 50, no. 1, pp. 112-21.

Li, L.Q., Tang, C., Xia, B.Q., Jin, H.Y., Zheng, Y. & Qiao, S.Z. 2019, 'Two-Dimensional Mosaic Bismuth Nanosheets for Highly Selective Ambient Electrocatalytic Nitrogen Reduction', *ACS Catalysis*, vol. 9, no. 4, pp. 2902-8.

Li, R.G. 2018, 'Photocatalytic nitrogen fixation: An attractive approach for artificial photocatalysis', *Chinese Journal of Catalysis*, vol. 39, no. 7, pp. 1180-8.

Li, T.T., Shan, B., Xu, W. & Meyer, T.J. 2019, 'Electrocatalytic CO_2 reduction with a ruthenium catalyst in solution and on nanocrystalline TiO_2', *ChemSusChem*, vol. 12, no. 11, pp. 2402-8.

Li, X.-H., Zhang, J., Chen, X., Fischer, A., Thomas, A., Antonietti, M. & Wang, X. 2011, 'Condensed Graphitic Carbon Nitride Nanorods by Nanoconfinement: Promotion of Crystallinity on Photocatalytic Conversion', *Chemistry of Materials*, vol. 23, no. 19, pp. 4344-8.

Li, X., Zhang, X., Everitt, H.O. & Liu, J. 2019, 'Light-induced thermal gradients in ruthenium catalysts significantly enhance ammonia production', *Nano Letters*, vol. 19, no. 3, pp. 1706-11.

Li, X.F., Li, Q.K., Cheng, J., Liu, L.L., Yan, Q., Wu, Y.C., Zhang, X.H., Wang, Z.Y., Qiu, Q. & Luo, Y. 2016, 'Conversion of Dinitrogen to Ammonia by FeN_3-Embedded Graphene', *Journal of the American Chemical Society*, vol. 138, no. 28, pp. 8706-9.

Li, X.M., Sun, X., Zhang, L., Sun, S.M. & Wang, W.Z. 2018, 'Efficient photocatalytic fixation of N_2 by KOH-treated g-C_3N_4', *Journal of Materials Chemistry A*, vol. 6, no. 7, pp. 3005-11.

Lidder, S. & Webb, A.J. 2013, 'Vascular effects of dietary nitrate (as found in green leafy vegetables and beetroot) via the nitrate-nitrite-nitric oxide pathway', *British journal of clinical pharmacology*, vol. 75, no. 3, pp. 677-96.

Liebig, J.v.J.A.P. 1834, 'About some nitrogen compounds', vol. 10, no. 10.

Lin, B., Heng, L., Fang, B., Yin, H., Ni, J., Wang, X., Lin, J. & Jiang, L. 2019, 'Ammonia synthesis activity of alumina-supported ruthenium catalyst enhanced by alumina phase transformation', *ACS Catalysis*, vol. 9, no. 3, pp. 1635-44.

Liu, A.Y. & Cohen, M.L. 1989, ' Prediction of new low compressibility solids', *Science*, vol. 245, no. 4920, pp. 841-2.

Liu, C.W., Li, Q.Y., Wu, C.Z., Zhang, J., Jin, Y.G., MacFarlane, D.R. & Sun, C.H. 2019, 'Single-Boron Catalysts for Nitrogen Reduction Reaction', *Journal of the American Chemical Society*, vol. 141, no. 7, pp. 2884-8.

Liu, C.W., Li, Q.Y., Zhang, J., Jin, Y.G., MacFarlane, D.R. & Sun, C.H. 2018, 'Theoretical Evaluation of Possible 2D Boron Monolayer in N_2 Electrochemical Conversion into Ammonia', *Journal of Physical Chemistry C*, vol. 122, no. 44, pp. 25268-73.

Liu, G., Wu, W. & Zhang, J. 2005, 'Regional differentiation of non-point source pollution of agriculture-derived nitrate nitrogen in groundwater in northern China', *Agriculture, ecosystems & environment*, vol. 107, no. 2-3, pp. 211-20.

Liu, G., You, S., Ma, M., Huang, H. & Ren, N. 2016, 'Removal of nitrate by photocatalytic denitrification using nonlinear optical material', *Environmental Science & Technology*, vol. 50, no. 20, pp. 11218-25.

Liu, J.X., Li, R., Zu, X., Zhang, X.C., Wang, Y.F., Wang, Y.W. & Fan, C.M. 2019, 'Photocatalytic conversion of nitrogen to ammonia with water on triphase interfaces of hydrophilic-hydrophobic composite $Bi_4O_5Br_2$/ZIF-8', *Chemical Engineering Journal*, vol. 371, pp. 796-803.

Liu, S.Z., Wang, S.B., Jiang, Y., Zhao, Z.Q., Jiang, G.Y. & Sun, Z.Y. 2019, 'Synthesis of Fe_2O_3 loaded porous g-C_3N_4 photocatalyst for photocatalytic reduction of dinitrogen to ammonia', *Chemical Engineering Journal*, vol. 373, pp. 572-9.

Liu, X., Liu, H., Wang, Y., Yang, W. & Yu, Y. 2020, 'Nitrogen-rich g-C_3N_4@ AgPd Mott-Schottky heterojunction boosts photocatalytic hydrogen production from water and tandem reduction of NO_3- and NO_2-', *Journal of Colloid and Interface Science*, vol. 581, pp. 619-26.

Liu, Y., Hu, Z. & Yu, J.C. 2020, 'Fe Enhanced Visible-Light-Driven Nitrogen Fixation on BiOBr Nanosheets', *Chemistry of Materials*, vol. 32, no. 4, pp. 1488-94.

Liu, Y., Jiang, Z., Zhang, X.Y. & Shen, P.K. 2018, 'Ultrathin porous Bi_5O_7X (X = Cl, Br, I) nanotubes for effective solar desalination', *Journal of Materials Chemistry A*, vol. 6, no. 41, pp. 20037-43.

Lu, H., Hao, Q., Chen, T., Zhang, L., Chen, D., Ma, C., Yao, W. & Zhu, Y. 2018, 'A high-performance Bi_2O_3/Bi_2SiO_5 p-n heterojunction photocatalyst induced by phase transition of Bi_2O_3', *Applied Catalysis B-Environmental*, vol. 237, pp. 59-67.

Lu, H.J., Wang, R.T., Zhang, L.H., Chen, D.M., Hao, Q., Ma, C. & Yao, W.Q. 2018, 'Photocatalyst Bi(OH)SO_4 center dot H_2O with High Photocatalytic Performance', *Russian Journal of Physical Chemistry A*, vol. 92, no. 10, pp. 2075-80.

Lundberg, J.O., Weitzberg, E. & Gladwin, M.T. 2008, 'The nitrate–nitrite–nitric oxide pathway in physiology and therapeutics', *Nature Reviews Drug discovery*, vol. 7, no. 2, pp. 156-67.

Lv, C., Yan, C., Chen, G., Ding, Y., Sun, J., Zhou, Y. & Yu, G. 2018a, 'An Amorphous Noble-Metal-Free Electrocatalyst that Enables Nitrogen Fixation under Ambient Conditions', *Angewandte Chemie International Edition*, vol. 57, no. 21, pp. 6073-6.

Lv, C.D., Yan, C.S., Chen, G., Ding, Y., Sun, J.X., Zhou, Y.S. & Yu, G.H. 2018b, 'An Amorphous Noble-Metal-Free Electrocatalyst that Enables Nitrogen Fixation under Ambient Conditions', *Angewandte Chemie International Edition*, vol. 57, no. 21, pp. 6073-6.

Maffei, N., Pelletier, L., Charland, J.P. & McFarlan, A. 2005, 'An intermediate temperature direct ammonia fuel cell using a proton conducting electrolyte', *Journal of Power Sources*, vol. 140, no. 2, pp. 264-7.

Meija, J., Coplen, T.B., Berglund, M., Brand, W.A., De Bievre, P., Groning, M., Holden, N.E., Irrgeher, J., Loss, R.D., Walczyk, T. & Prohaska, T. 2016, 'Atomic weights of the elements 2013 (IUPAC Technical Report)', *Pure and Applied Chemistry*, vol. 88, no. 3, pp. 265-91.

Meng, Q.Q., Lv, C.D., Sun, J.X., Hong, W.Z., Xing, W.N., Qiang, L.S., Chen, G. & Jin, X.L. 2019, 'High-efficiency Fe-Mediated Bi_2MoO_6 nitrogen-fixing photocatalyst: Reduced surface work function and ameliorated surface reaction', *Applied Catalysis B-Environmental*, vol. 256, p. 117781.

Monkhorst, H.J. & Pack, J.D. 1976, 'Special points for Brillouin-zone integrations', *Physical Review B*, vol. 13, no. 12, p. 5188.

Montoya, J.H., Tsai, C., Vojvodic, A. & Norskov, J.K. 2015, 'The Challenge of Electrochemical Ammonia Synthesis: A New Perspective on the Role of Nitrogen Scaling Relations', *Chemsuschem*, vol. 8, no. 13, pp. 2180-6.

Motevalli, A., Naghibi, S.A., Hashemi, H., Berndtsson, R., Pradhan, B. & Gholami, V. 2019, 'Inverse method using boosted regression tree and k-nearest neighbor to quantify effects of point and non-point source nitrate pollution in groundwater', *Journal of Cleaner Production*, vol. 228, pp. 1248-63.

Mou, H., Wang, J., Yu, D., Zhang, D., Chen, W., Wang, Y., Wang, D. & Mu, T. 2019, 'Fabricating Amorphous g-C_3N_4/ZrO_2 Photocatalysts by One-Step Pyrolysis for Solar-Driven Ambient Ammonia Synthesis', *Acs Applied Materials & Interfaces*, vol. 11, no. 47, pp. 44360-5.

Music, D., Konstantinidis, S. & Schneider, J. 2009, 'Equilibrium structure of delta-Bi_2O_3 from first principles', *Journal of Physics-Condensed Matter*, vol. 21, no. 17, p. 7.

Myers, M., Khir, F.L.M., Home, M.A., Mennell, C., Gillbanks, J., Tadich, A., Baker, M.V., Nener, B.D. & Parish, G. 2018, 'XPS/NEXAFS spectroscopic and conductance studies of glycine on AlGaN/GaN transistor devices', *Applied Surface Science*, vol. 435, pp. 23-30.

Ni, W., Gurzadyan, G.G., Ma, L., Hu, P., Kloc, C. & Sun, L. 2020, 'Ultrafast Tuning of Various Photochemical Pathways in Perylene–TCNQ Charge-Transfer Crystals', *The Journal of Physical Chemistry C*, vol. 124, no. 25, pp. 13894-901.

Nørskov, J.K., Rossmeisl, J., Logadottir, A., Lindqvist, L., Kitchin, J.R., Bligaard, T. & Jonsson, H. 2004, 'Origin of the overpotential for oxygen reduction at a fuel-cell cathode', *The Journal of Physical Chemistry B*, vol. 108, no. 46, pp. 17886-92.

Oakes, J.S. 2013, 'Investigation of iron reduction by green tea polyphenols for application in soil remediation'.

Oshikiri, T., Ueno, K. & Misawa, H. 2014, 'Plasmon-Induced Ammonia Synthesis through Nitrogen Photofixation with Visible Light Irradiation', *Angewandte Chemie-International Edition*, vol. 53, no. 37, pp. 9802-5.

Park, J.Y. & Yoo, Y.J. 2009, 'Biological nitrate removal in industrial wastewater treatment: which electron donor we can choose', *Applied microbiology and biotechnology*, vol. 82, no. 3, pp. 415-29.

Peña-Haro, S., Pulido-Velazquez, M. & Sahuquillo, A. 2009, 'A hydro-economic modelling framework for optimal management of groundwater nitrate pollution from agriculture', *Journal of Hydrology*, vol. 373, no. 1-2, pp. 193-203.

Peng, X.G., Manna, L., Yang, W.D., Wickham, J., Scher, E., Kadavanich, A. & Alivisatos, A.P. 2000, 'Shape control of CdSe nanocrystals', *Nature*, vol. 404, no. 6773, pp. 59-61.

Perdew, J.P., Burke, K. & Ernzerhof, M. 1996, 'Generalized gradient approximation made simple', *Physical Review Letters*, vol. 77, no. 18, pp. 3865-8.

Pintar, A., Batista, J. & Levec, J. 2001, 'Catalytic denitrification: direct and indirect removal of nitrates from potable water', *Catalysis Today*, vol. 66, no. 2-4, pp. 503-10.

Polikhronidi, N.G., Abdulagatov, I.M., Batyroua, R.G. & Stepanov, G.V. 2009, 'PVT measurements of water-ammonia refrigerant mixture in the critical and supercritical regions', *International Journal of Refrigeration-Revue Internationale Du Froid*, vol. 32, no. 8, pp. 1897-913.

Ran, J., Ma, T.Y., Gao, G., Du, X.-W. & Qiao, S.Z. 2015, 'Porous P-doped graphitic carbon nitride nanosheets for synergistically enhanced visible-light photocatalytic H_2 production', *Energy & Environmental Science*, vol. 8, no. 12, pp. 3708-17.

Rehman, J.U., Ahmad, N., Ullah, N., Alam, I. & Ullah, H. 2020, 'Health risks in different age group of nitrate in spring water used for drinking in Harnai, Balochistan, Pakistan', *Ecology of food and nutrition*, vol. 59, no. 5, pp. 462-71.

Ren, H.-T., Jia, S.-Y., Zou, J.-J., Wu, S.-H. & Han, X. 2015, 'A facile preparation of Ag_2O/P_{25} photocatalyst for selective reduction of nitrate', *Applied Catalysis B: Environmental*, vol. 176, pp. 53-61.

Rezaei, H., Jafari, A., Kamarehie, B., Fakhri, Y., Ghaderpoury, A., Karami, M.A., Ghaderpoori, M., Shams, M., Bidarpoor, F. & Salimi, M. 2019, 'Health-risk assessment related to the fluoride, nitrate, and nitrite in the drinking water in the Sanandaj, Kurdistan County, Iran', *Human and ecological risk assessment: an international journal*, vol. 25, no. 5, pp. 1242-50.

Sa, J., Agüera, C.A., Gross, S. & Anderson, J.A. 2009, 'Photocatalytic nitrate reduction over metal modified TiO_2, *Applied Catalysis B: Environmental*, vol. 85, no. 3-4, pp. 192-200.

Samatya, S., Kabay, N., Yüksel, Ü., Arda, M. & Yüksel, M. 2006, 'Removal of nitrate from aqueous solution by nitrate selective ion exchange resins', *Reactive and Functional Polymers*, vol. 66, no. 11, pp. 1206-14.

Santamaria, P. 2006, 'Nitrate in vegetables: toxicity, content, intake and EC regulation', *Journal of the Science of Food and Agriculture*, vol. 86, no. 1, pp. 10-7.

Saravanan, R., Khan, M.M., Gupta, V.K., Mosquera, E., Gracia, F., Narayanan, V. & Stephen, A. 2015, 'ZnO/Ag/CdO nanocomposite for visible light-induced photocatalytic degradation of industrial textile effluents', *Journal of Colloid and Interface Science*, vol. 452, pp. 126-33.

Scherer, H.W., Mengel, K., Dittmar, H., Drach, M., Vosskamp, R., Trenkel, M.E., Gutser, R., Steffens, G., Czikkely, V. & Niedermaier, T. 2000, 'Fertilizers', *Ullmann's Encyclopedia of Industrial Chemistry*.

Schoeman, J. & Steyn, A. 2003, 'Nitrate removal with reverse osmosis in a rural area in South Africa', *Desalination*, vol. 155, no. 1, pp. 15-26.

Sharma, R., Khanuja, M., Sharma, S.N. & Sinha, O.P. 2017, 'Reduced band gap & charge recombination rate in Se doped α-Bi_2O_3 leads to enhanced photoelectrochemical and photocatalytic performance: theoretical & experimental insight', *International Journal*

of Hydrogen Energy, vol. 42, no. 32, pp. 20638-48.

Sheng, J., He, Y., Li, J., Yuan, C., Huang, H., Wang, S., Sun, Y., Wang, Z. & Dong, F. 2020, 'Identification of Halogen-Associated Active Sites on Bismuth-Based Perovskite Quantum Dots for Efficient and Selective CO_2-to-CO Photoreduction', *ACS nano*, vol. 14, no. 10, pp. 13103-14.

Shi, R., Zhao, Y., Waterhouse, G.I., Zhang, S. & Zhang, T. 2019, 'Defect engineering in photocatalytic nitrogen fixation', *ACS Catalysis*, vol. 9, no. 11, pp. 9739-50.

Shi, Z., Zhang, Y., Shen, X., Duoerkun, G., Zhu, B., Zhang, L., Li, M. & Chen, Z. 2020, 'Fabrication of g-C_3N_4/BiOBr heterojunctions on carbon fibers as weaveable photocatalyst for degrading tetracycline hydrochloride under visible light', *Chemical Engineering Journal*, vol. 386, p. 124010.

Siddiqui, O. & Dincer, I. 2017, 'Analysis and performance assessment of a new solar-based multigeneration system integrated with ammonia fuel cell and solid oxide fuel cell-gas turbine combined cycle', *Journal of Power Sources*, vol. 370, pp. 138-54.

Sim, H.Y.F., Chen, J.R.T., Koh, C.S.L., Lee, H.K., Han, X., Phan-Quang, G.C., Pang, J.Y., Lay, C.L., Pedireddy, S. & Phang, I.Y. 2020, 'ZIF-induced d-band Modification in Bimetallic Nanocatalyst: Achieving> 44% Efficiency in Ambient Nitrogen Reduction Reaction', *Angewandte Chemie International Edition.* vol. 132, no. 39, p. 17145-51.

Soares, M. 2000, 'Biological denitrification of groundwater', *Water, Air, and Soil Pollution*, vol. 123, no. 1, pp. 183-93.

Sun, S.M., An, Q., Wang, W.Z., Zhang, L., Liu, J.J. & Goddard, W.A. 2017, 'Efficient photocatalytic reduction of dinitrogen to ammonia on bismuth monoxide quantum dots', *Journal of Materials Chemistry A*, vol. 5, no. 1, pp. 201-9.

Swann, P.F. 1975, 'The toxicology of nitrate, nitrite and n-nitroso compounds', *Journal of the Science of Food and Agriculture*, vol. 26, no. 11, pp. 1761-70.

Tang, C. & Qiao, S.Z. 2019, 'How to explore ambient electrocatalytic nitrogen reduction reliably and insightfully', *Chemical Society Reviews*, vol. 48, no. 12, pp. 3166-80.

Tennakone, K., Thaminimulla, C. & Bandara, J. 1992, 'Nitrogen photoreduction by vanadium (III)-substituted hydrous ferric oxide', *Journal of Photochemistry and Photobiology A: Chemistry*, vol. 68, no. 2, pp. 131-5.

Teter, D.M. & Hemley, R.J. 1996, 'Low-compressibility carbon nitrides', *Science*, vol. 271, no. 5245, pp. 53-5.

Tong, N., Wang, Y., Liu, Y., Li, M.B., Zhang, Z.Z., Huang, H.J., Sun, T., Yang, J.X., Li, F.Y. & Wang, X.X. 2018, 'PdSn/NiO/$NaTa_3$:La:La for photocatalytic ammonia synthesis by reduction of NO_3^- with formic acid in aqueous solution', *Journal of Catalysis*, vol. 361, pp. 303-12.

Tong, Y.Y., Guo, H.P., Liu, D.L., Yan, X., Su, P.P., Liang, J., Zhou, S., Liu, J., Lu, G.Q. & Dou, S.X. 2020, 'Vacancy Engineering of Iron-Doped $W_{18}O_{49}$ Nanoreactors for Low-Barrier Electrochemical Nitrogen Reduction', *Angewandte Chemie-International Edition*, vol. 59, no. 19, pp. 7356-61.

Tu, X., Luo, S., Chen, G. & Li, J. 2012, 'One-Pot Synthesis, Characterization, and Enhanced Photocatalytic Activity of a BiOBr–Graphene Composite', *Chemistry–A European Journal*, vol. 18, no. 45, pp. 14359-66.

Vanýsek, P. 2012, 'Electrochemical series', *Handbook of Chemistry and Physics*, vol. 93, pp.

5-80.

Velu, M., Balasubramanian, B., Velmurugan, P., Kamyab, H., Ravi, A.V., Chelliapan, S., Lee, C.T. & Palaniyappan, J. 2021, 'Fabrication of nanocomposites mediated from aluminium nanoparticles/Moringa oleifera gum activated carbon for effective photocatalytic removal of nitrate and phosphate in aqueous solution', *Journal of Cleaner Production*, vol. 281, p. 124553.

Wakida, F.T. & Lerner, D.N. 2005, 'Non-agricultural sources of groundwater nitrate: a review and case study', *Water Research*, vol. 39, no. 1, pp. 3-16.

Wang, S.Y., Hai, X., Ding, X., Chang, K., Xiang, Y.G., Meng, X.G., Yang, Z.X., Chen, H. & Ye, J.H. 2017, 'Light-Switchable Oxygen Vacancies in Ultrafine Bi_5O_7Br Nanotubes for Boosting Solar-Driven Nitrogen Fixation in Pure Water', *Advanced Materials*, vol. 29, no. 31, p. 1701774.

Wang, W., Herreros, J.M., Tsolakis, A. & York, A.P. 2013, 'Ammonia as hydrogen carrier for transportation; investigation of the ammonia exhaust gas fuel reforming', *International Journal of Hydrogen Energy*, vol. 38, no. 23, pp. 9907-17.

Wang, X., Qiu, S., Feng, J., Tong, Y., Zhou, F., Li, Q., Song, L., Chen, S., Wu, K.H. & Su, P. 2020, 'Confined Fe–Cu Clusters as Sub-Nanometer Reactors for Efficiently Regulating the Electrochemical Nitrogen Reduction Reaction', *Advanced Materials*, vol. 32, no. 40, p. 2004382.

Wang, Y., Shi, M.-M., Bao, D., Meng, F.-L., Zhang, Q., Zhou, Y.-T., Liu, K.-H., Zhang, Y., Wang, J.-Z., Chen, Z.-W., Liu, D.-P., Jiang, Z., Luo, M., Gu, L., Zhang, Q.-H., Cao, X.-Z., Yao, Y., Shao, M.-H., Zhang, Y., Zhang, X.-B., Chen, J.G., Yan, J.-M. & Jiang, Q. 2019a, 'Generating Defect-Rich Bismuth for Enhancing the Rate of Nitrogen Electroreduction to Ammonia', *Angewandte Chemie International Edition,* vol. 131, no. 28, pp. 9564-9.

Wang, Y., Tian, Y., Yan, L. & Su, Z. 2018, 'DFT study on sulfur-doped g-C3N4 nanosheets as a photocatalyst for CO_2 reduction reaction', *The Journal of Physical Chemistry C*, vol. 122, no. 14, pp. 7712-9.

Wang, Y., Zhou, W., Jia, R., Yu, Y. & Zhang, B. 2020, 'Unveiling the Activity Origin of a Copper-based Electrocatalyst for Selective Nitrate Reduction to Ammonia', *Angewandte Chemie Internationl Edition,* vol. 131, no. 13, pp. 5388-92.

Wang, Y.T., Yu, Y.F., Jia, R.R., Zhang, C. & Zhang, B. 2019, 'Electrochemical synthesis of nitric acid from air and ammonia through waste utilization', *National Science Review*, vol. 6, no. 4, pp. 730-8.

Wang, Z.L., Mao, X., Chen, P., Xiao, M., Monny, S.A., Wang, S.C., Konarova, M., Du, A.J. & Wang, L.Z. 2019, 'Understanding the Roles of Oxygen Vacancies in Hematite-Based Photoelectrochemical Processes', *Angewandte Chemie-International Edition*, vol. 58, no. 4, pp. 1030-4.

Wang, Z.L., Zhang, L., Schulli, T.U., Bai, Y., Monny, S.A., Du, A.J. & Wang, L.Z. 2019, 'Identifying Copper Vacancies and Their Role in the CuO Based Photocathode for Water Splitting', *Angewandte Chemie-International Edition*, vol. 58, no. 49, pp. 17604-9.

Wen, J.Q., Xie, J., Chen, X.B. & Li, X. 2017, 'A review on g-C_3N_4-based photocatalysts', *Applied Surface Science*, vol. 391, pp. 72-123.

Wick, K., Heumesser, C. & Schmid, E. 2012, 'Groundwater nitrate contamination: factors and indicators', *Journal of Environmental Management*, vol. 111, pp. 178-86.

Wu, Y., Yuan, B., Li, M., Zhang, W.-H., Liu, Y. & Li, C. 2015, 'Well-defined BiOCl colloidal ultrathin nanosheets: synthesis, characterization, and application in photocatalytic aerobic oxidation of secondary amines', *Chemical Science*, vol. 6, no. 3, pp. 1873-8.

Xia, J., Di, J., Li, H., Xu, H., Li, H. & Guo, S. 2016, 'Ionic liquid-induced strategy for carbon quantum dots/BiOX (X= Br, Cl) hybrid nanosheets with superior visible light-driven photocatalysis', *Applied Catalysis B: Environmental*, vol. 181, pp. 260-9.

Xue, X., Chen, R., Yan, C., Hu, Y., Zhang, W., Yang, S., Ma, L., Zhu, G. & Jin, Z. 2019, 'Efficient photocatalytic nitrogen fixation under ambient conditions enabled by the heterojunctions of n-type Bi_2MoO_6 and oxygen-vacancy-rich p-type BiOBr', *Nanoscale*, vol. 11, no. 21, pp. 10439-45.

Xue, X.L., Chen, R.P., Chen, H.W., Hu, Y., Ding, Q.Q., Liu, Z.T., Ma, L.B., Zhu, G.Y., Zhang, W.J., Yu, Q., Liu, J., Ma, J. & Jin, Z. 2018, 'Oxygen Vacancy Engineering Promoted Photocatalytic Ammonia Synthesis on Ultrathin Two-Dimensional Bismuth Oxybromide Nanosheets', *Nano Letters*, vol. 18, no. 11, pp. 7372-7.

Xue, X.L., Chen, R.P., Yan, C.Z., Zhao, P.Y., Hu, Y., Zhang, W.J., Yang, S.Y. & Jin, Z. 2019, 'Review on photocatalytic and electrocatalytic artificial nitrogen fixation for ammonia synthesis at mild conditions: Advances, challenges and perspectives', *Nano Research*, vol. 12, no. 6, pp. 1229-49.

Yan, H.J. & Yang, H.X. 2011, 'TiO_2-g-C_3N_4 composite materials for photocatalytic H-2 evolution under visible light irradiation', *Journal of Alloys and Compounds*, vol. 509, no. 4, pp. L26-L9.

Yan, X., Liu, D., Cao, H., Hou, F., Liang, J. & Dou, S.X. 2019, 'Nitrogen Reduction to Ammonia on Atomic-Scale Active Sites under Mild Conditions', *Small Methods*, vol. 3, no. 9, p. 1800501.

Yan, Y., Yang, H., Yi, Z., Wang, X., Li, R. & Xian, T. 2020, 'Evolution of Bi nanowires from BiOBr nanoplates through a $NaBH_4$ reduction method with enhanced photodegradation performance', *Environmental Engineering Science*, vol. 37, no. 1, pp. 64-77.

Yang, F.Y., Liu, K., Chien, C.L. & Searson, P.C. 1999, 'Large magnetoresistance and finite-size effects in electrodeposited single-crystal Bi thin films', *Physical Review Letters*, vol. 82, no. 16, pp. 3328-31.

Yao, J.X., Bao, D., Zhang, Q., Shi, M.M., Wang, Y., Gao, R., Yan, J.M. & Jiang, Q. 2018, 'Tailoring Oxygen Vacancies of $BiVO_4$ toward Highly Efficient Noble-Metal-Free Electrocatalyst for Artificial N_2 Fixation under Ambient Conditions', *Small Methods*, vol. 3, no.6, p. 1800333.

Yu, H., Huang, H., Xu, K., Hao, W., Guo, Y., Wang, S., Shen, X., Pan, S. & Zhang, Y. 2017, 'Liquid-Phase Exfoliation into Monolayered BiOBr Nanosheets for Photocatalytic Oxidation and Reduction', *ACS Sustainable Chemistry & Engineering*, vol. 5, no. 11, pp. 10499-508.

Yu, H., Huang, J., Jiang, L., Shi, Y., Yi, K., Zhang, W., Zhang, J., Chen, H. & Yuan, X. 2020, 'Enhanced photocatalytic tetracycline degradation using N-CQDs/OV-BiOBr composites: Unraveling the complementary effects between N-CQDs and oxygen vacancy', *Chemical Engineering Journal*, vol. 402, p. 126187.

Yue, F.-J., Waldron, S., Li, S.-L., Wang, Z.-J., Zeng, J., Xu, S., Zhang, Z.-C. & Oliver, D.M. 2019, 'Land use interacts with changes in catchment hydrology to generate chronic nitrate pollution in karst waters and strong seasonality in excess nitrate export', *Science of the Total Environment*, vol. 696, p. 134062.

Zhang, D., Wang, B., Gong, X., Yang, Z. & Liu, Y. 2019, 'Selective reduction of nitrate to nitrogen gas by novel Cu_2O-Cu^0@ Fe0 composite combined with HCOOH under UV radiation', *Chemical Engineering Journal*, vol. 359, pp. 1195-204.

Zhang, H., Liu, Z., Li, Y., Zhang, C., Wang, Y., Zhang, W., Wang, L., Niu, L., Wang, P. & Wang, C. 2020, 'Intimately coupled TiO2/g-C3N4 photocatalysts and in-situ cultivated biofilms enhanced nitrate reduction in water', *Applied Surface Science*, vol. 503, p. 144092.

Zhang, J.S., Wang, B. & Wang, X.C. 2013, 'Chemical Synthesis and Applications of Graphitic Carbon Nitride', *Acta Physico-Chimica Sinica*, vol. 29, no. 9, pp. 1865-76.

Zhang, N., Li, L.G., Shao, Q., Zhu, T., Huang, X.Q. & Xiao, X.H. 2019, 'Fe-Doped BiOCl Nanosheets with Light-Switchable Oxygen Vacancies for Photocatalytic Nitrogen Fixation', *Acs Applied Energy Materials*, vol. 2, no. 12, pp. 8394-8.

Zhang, S., Zhao, Y., Shi, R., Waterhouse, G.I. & Zhang, T. 2019, 'Photocatalytic ammonia synthesis: Recent progress and future', *EnergyChem*, vol. 1, no. 2, p. 100013.

Zhang, X., Sun, X., Guo, S.-X., Bond, A.M. & Zhang, J. 2019, 'Formation of lattice-dislocated bismuth nanowires on copper foam for enhanced electrocatalytic CO_2 reduction at low overpotential', *Energy & Environmental Science*, vol. 12, no. 4, pp. 1334-40.

Zhang, Z., Wang, J., Liu, D., Luo, W., Zhang, M., Jiang, W. & Zhu, Y. 2016, 'Highly efficient organic photocatalyst with full visible light spectrum through π–π stacking of TCNQ–PTCDI', *ACS applied materials & interfaces*, vol. 8, no. 44, pp. 30225-31.

Zhao, J., Li, N., Yu, R., Zhao, Z. & Nan, J. 2018, 'Magnetic field enhanced denitrification in nitrate and ammonia contaminated water under 3D/2D Mn_2O_3/g-C_3N_4 photocatalysis', *Chemical Engineering Journal*, vol. 349, pp. 530-8.

Zhao, W.R., Zhang, J., Zhu, X., Zhang, M., Tang, J., Tan, M. & Wang, Y. 2014, 'Enhanced nitrogen photofixation on Fe-doped TiO_2 with highly exposed (101) facets in the presence of ethanol as scavenger', *Applied Catalysis B-Environmental*, vol. 144, pp. 468-77.

Zhao, Y., Setzler, B.P., Wang, J., Nash, J., Wang, T., Xu, B. & Yan, Y. 2019, 'An efficient direct ammonia fuel cell for affordable carbon-neutral transportation', *Joule*, vol. 3, no. 10, pp. 2472-84.

Zhou, C., Shi, R., Shang, L., Wu, L.Z., Tung, C.H. & Zhang, T.R. 2018, 'Template-free large-scale synthesis of g-C_3N_4 microtubes for enhanced visible light-driven photocatalytic H_2 production', *Nano Research*, vol. 11, no. 6, pp. 3462-8.

Zhou, X., Liu, G., Yu, J. & Fan, W. 2012, 'Surface plasmon resonance-mediated photocatalysis by noble metal-based composites under visible light', *Journal of Materials Chemistry*, vol. 22, no. 40, pp. 21337-54.

Zhou, Z., Zhang, Y., Shen, Y., Liu, S. & Zhang, Y. 2018, 'Molecular engineering of polymeric carbon nitride: advancing applications from photocatalysis to biosensing and more', *Chemical Society Reviews*, vol. 47, no. 7, pp. 2298-321.